JAEA-Research
2006-034

JP0650404

JAEA-Research

Preparation and Characterization of B-C-N Hybrid Thin Films

Md.Nizam UDDIN*, Iwao SHIMOYAMA
Tetsuhiro SEKIGUCHI, Krishna G.NATH*
Yuji BABA and Masamitsu NAGANO*

Surface Chemistry Research Group
Quantum Beam Science Directorate

June 2006

Japan Atomic Energy Agency

日本原子力研究開発機構

JAEA-Research 2006-034

Preparation and Characterization of B-C-N Hybrid Thin Films

Md. Nizam UDDIN*[1], Iwao SHIMOYAMA, Tetsuhiro SEKIGUCHI, Krishna G. NATH*[2], Yuji BABA and Masamitsu NAGANO*[3]

Synchrotron Radiation Research Unit, Quantum Beam Science Directorate
Japan Atomic Energy Agency
Tokai-mura, Naka-gun, Ibaraki-ken
(Received February 23, 2006)

Two dimensional thin films composed of boron, carbon and nitrogen (B-C-N hybrid) were synthesized by ion beam deposition, and their electronic and geometrical structures were characterized by core-level spectroscopy using synchrotron radiation. B-C-N hybrid thin films were grown from ion beam plasma of borazine on highly oriented pyrolitic graphite (HOPG) at various temperatures. The films were characterized *in-situ* by X-ray photoelectron spectroscopy (XPS) and near edge X-ray absorption fine structure (NEXAFS). XPS study suggested that B, N and C atoms in the deposited films were in a wide variety of chemical bonds *e.g.*, B-C, B-N, N-C, and B-C-N. It was found that B-C-N hybrid formation was enhanced at high temperature, and that the B-C-N component was dominantly synthesized at low boron content. In the NEXAFS spectra, the resonance peaks from B 1s to unoccupied π*-like orbitals were clearly observed. The polarization dependence of the B 1s→π^* resonance peaks confirmed that the highly oriented graphite-like B-C-N hybrids surely exist at low boron content.

Keywords: Ion Beam Implantation, B-C-N Hybrid Thin Films, X-Ray Photoelectron Spectroscopy, Synchrotron Radiation, Near-Edge X-Ray Absorption Fine Structure

---

*1 Department of Chemistry, Shah Jalal University of Science and Technology, Sylhet 3114, Bangladesh
(Research Student of JAERI from April 2003 to February 2005)

*2 INRS-EMT, Univ. of Quebec 1650 Boul. Lionel Boulet, J3X 1S2 Varennes, QC, Canada
(Research Fellow of JAERI from June June 2001 to May 2004)

*3 Department of Applied Chemistry, Graduate School of Science and Engineering, Saga University

B-C-Nハイブリッド薄膜の合成と構造解析

日本原子力研究開発機構　量子ビーム応用研究部門　放射光科学研究ユニット

Md. Nizam UDDIN[1*]、下山　巖、関口　哲弘、Krishna G. NATH[*2]、

馬場　祐治、永野　正光[*3]

(2006年2月23日受理)

イオンビーム蒸着法によりホウ素、炭素、窒素からなる二次元薄膜（B-C-N ハイブリッド薄膜）を合成し、その電子構造と立体構造を放射光を用いた内殻分光法により調べた。B-C-N ハイブリッド薄膜は、種々の温度で高配向性熱分解グラファイト（HOPG）表面にボラジンガスの放電により生成したプラズマを蒸着させることにより合成した。薄膜の構造は X 線光電子分光法(XPS)および X 線吸収端微細構造法(NEXAFS)によりその場観察した。XPS 測定の結果、薄膜中のホウ素、炭素、窒素原子は B-C、B-N、B-C-N など種々の結合状態をとることがわかった。B-C-N ハイブリッドは高温で作成するほど効率よく生成し、ホウ素の濃度が低い領域では B-C-N 結合をもつ薄膜の生成が支配的になることを明らかにした。NEXAFS スペクトルには、B 1s 軌道からπ^*的性格を持つ価電子帯の非占有軌道への共鳴吸収によるピークが明瞭に観測された。このピークの偏光依存性を調べた結果、ホウ素の濃度が低い領域においてグラファイトと同様な配向性をとる二次元状の B-C-N ハイブリッド薄膜が安定に存在することを明らかにした。

原子力科学研究所（駐在）：〒319-1195 茨城県那珂郡東海村白方白根 2-4

*1 Department of Chemistry, Shah Jalal University of Science and Technology（2003年4月から2005年2月まで日本原子力研究所特別研究生）

*2 INRS-EMT, Univ. of Quebec（2001年6月から2004年5月まで日本原子力研究所リサーチフェロー）

*3 佐賀大学理工学部機能物質化学科

Contents

目次

List of Abbreviations

XPS	x-ray photoelectron spectroscopy
FWHM	full-width at half-maximum
IBI	ion beam implantation
HOPG	highly oriented pyrolitic graphite
SR	synchrotron radiation
NEXAFS	near-edge x-ray absorption fine structure
RT	room temperature
UHV	ultrahigh vacuum
QMS	quadrupole mass spectrometer
ELNES	electron energy loss near-edge structures
EELS	electron energy loss spectroscopy
XANES	x-ray absorption near-edge structure
TEY	total electron yield

本報告書に用いた略称一覧

XPS	X線光電子分光法
FWHM	半値全幅
IBI	イオン注入
HOPG	高配向性熱分解グラファイト
SR	放射光
NEXAFS	X線近吸収端微細構造
RT	室温
UHV	超高真空
QMS	四重極質量分析計
ELNES	エネルギー損失吸収微細構造
EELS	電子エネルギー損失分光法
XANES	X線吸収端微細構造
TEY	全電子収量

List of Table and Figures

List of Table

List of Figures

1. Introduction

1.1 General consideration

The phase diagram of the ternary B-C-N system is shown in Figure 1. The vertices and sides contain interesting phases including diamond, graphite, fullerene, carbon nanotubes, boron carbide, boron nitride, and hypothetical carbon nitride [1,2,3].

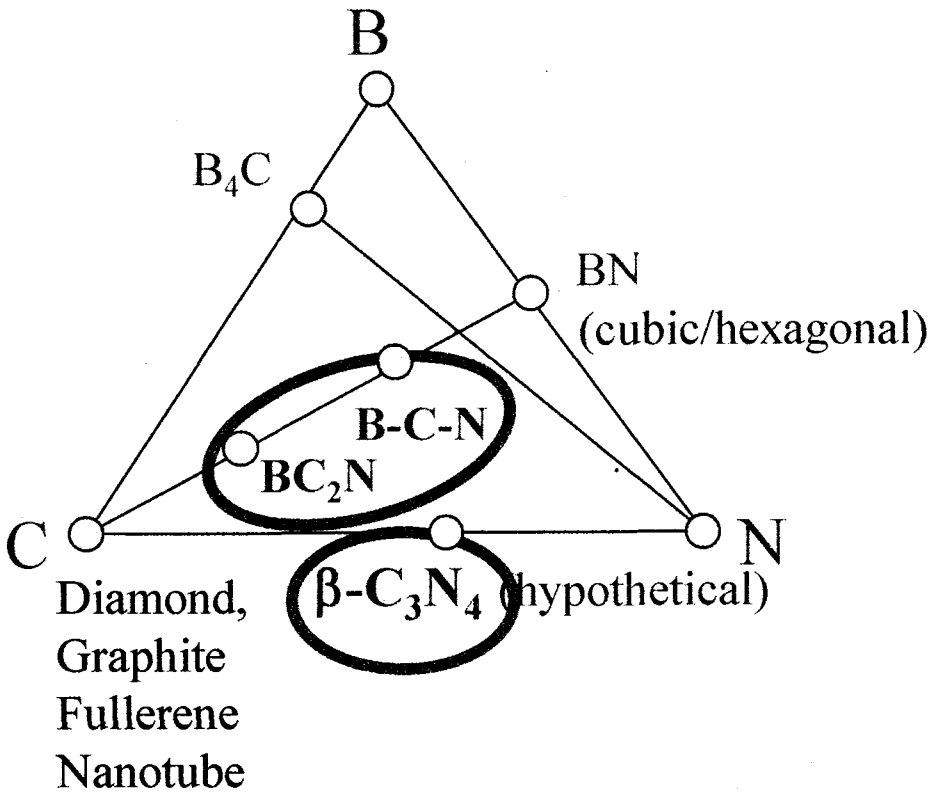

Fig. 1. Phase diagram of ternary B-C-N system.

On the search for new hard materials which might even be harder than diamond, the hardest known substance, much effort has been made on promising materials such as boron nitride [4-7] and diamond like carbon (DLC) [8-15].

Among the materials in vertices and sides of the ternary B-C-N system in Fig. 1, hexagonal boron nitride (*h*-BN) and graphite (shown in Fig. 2) have almost the same crystal structures. These two materials, however, have quite different electrical property; *h*-BN is an insulator while graphite is a semi-metal.

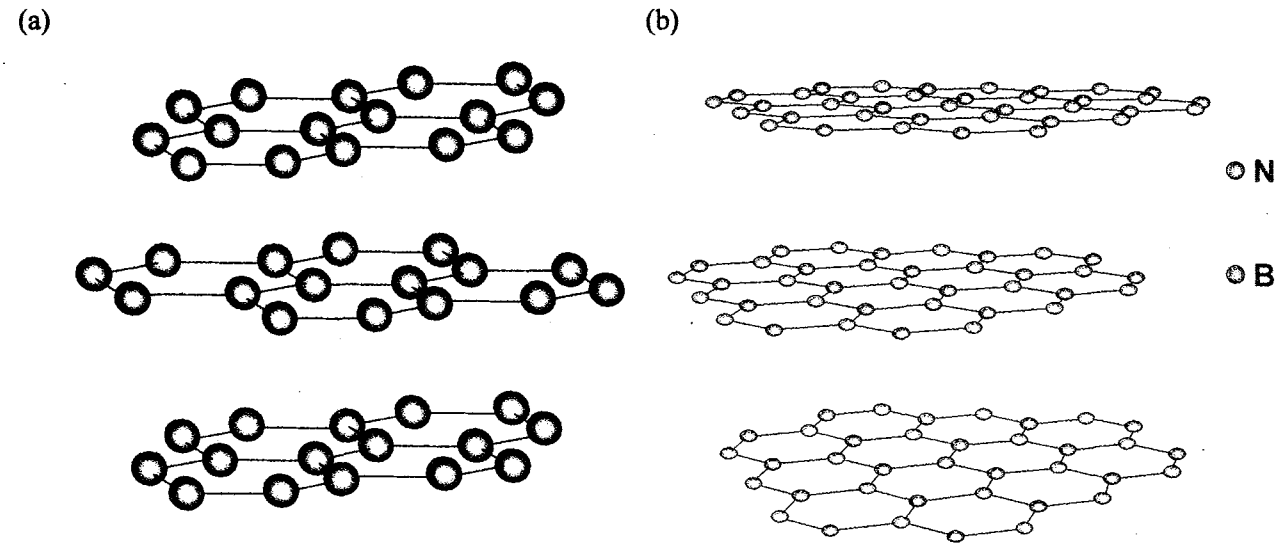

Fig. 2. Structures of (a) graphite and (b) hexagonal boron nitride.

The synthesis of the hybrid compounds of these two materials has been motivated from the differences in conducting properties, in spite of the similarities in their phase diagrams and atomic sizes. If a stable B-C-N hybrid with graphite-like structure is synthesized, it may have semiconducting property with versatile band-gap [1]. Thus this material is interesting for applications to electronic and luminescent devices [1].

However, the single phase of B-C-N hybrid has not been prepared successfully. Recently, the synthesis and characterization of B-C-N hybrid have attracted many research interests due to its interesting properties [1]. In this study, the preparation and characterization of B-C-N hybrids have been performed.

1.2 B-C-N hybrid thin films

Three possible atomic arrangements of graphite-like BC_2N have been proposed [16] using a first-principles pseudopotential approach. These are shown in Fig. 3. According to the calculation, the possible model (Model I) would be a metal and two others (Models II and III) would be semiconductors. This implies that the electrical properties should depend on the particular atomic arrangement in B-C-N hybrid. In addition to BC_2N, other compositions such as BC_3N [17], BC_6N [18], and BC_3 [19], with graphite-like structure have also been proposed. Some other compositions of B-C-N

hybrids with graphite-like structures have also been proposed [16,17]. The synthesis of single phase B-C-N hybrid has become a challenge because of its compositional varieties.

(I)

(II)

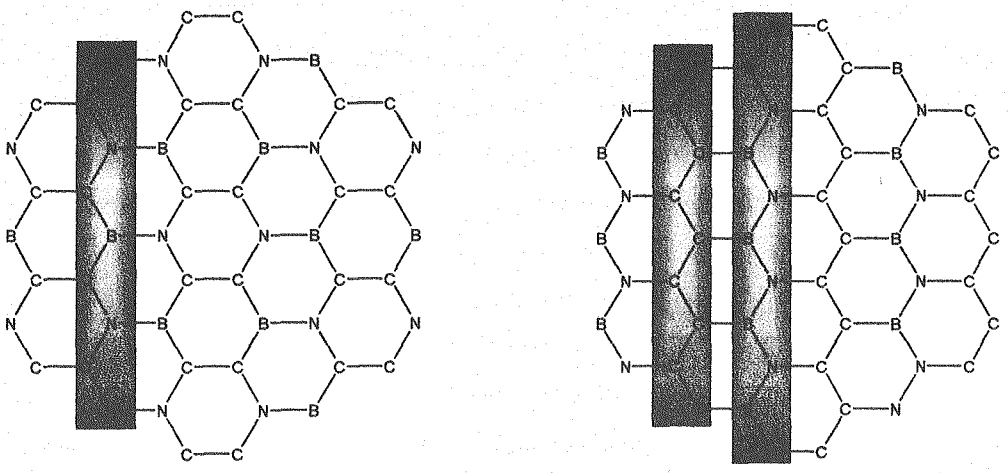

(III)

Fig. 3. Proposed structural models for BC_2N [16]. Model I is for metal and Models II and III are for semiconductor.

The structures of B-C-N hybrids have been explored by employing the core-level spectroscopy. It is reported that the electron-energy-loss near-edge structures (ELNES) for BC_2N show consistently graphite-like appearance at the K edges (B, C, and N K-edge features) on the basis of the theoretical calculations (multiple scattering approach) [20]. Experimentally, there have been a few works which show the formation of graphite-like B-C-N hybrids [19,21]. In these works, however, the samples were characterized by electron microscope combined with electron energy loss spectroscopy (EELS) [21]. These analyses do not exclude the possibility that the films may have nanocrystalline or amorphous structures instead of single crystalline phase. It was difficult to distinguish B-C-N hybrid from BN

component in the EELS feature [21] because of the poor resolution of that spectrum. No unambiguous experimental evidence for the existence of the graphite-like configuration of B-C-N hybrids has been shown yet. Therefore, the preparation of B-C-N hybrids with highly oriented graphite-like structure and its characterization have been attempted in this work.

X-ray photoelectron spectroscopy (XPS) is one of the powerful tools for the investigation of the electronic structures of solid surface. This method has been widely used for the characterization of B–C–N hybrids. Most of the XP spectra of the B–C–N hybrids show relatively high content of BN component in the products. In addition, the broad features of these spectra suggest that different configurations of B–C–N hybrids are included in the products instead of the single phase. It has become a challenge how to increase the relative portion of B–C–N hybrid component in the films.

Near-edge x-ray absorption fine structure (NEXAFS) using synchrotron radiation is another powerful method to study the geometrical and electronic structures of solid surfaces. NEXAFS is suited for the structural analysis of B-C-N hybrids for the following reasons. Firstly, a sharp π^* resonance would be observed below an ionization threshold of K-edge if the sample has a π bond, because NEXAFS probes unoccupied electronic states. Secondly, NEXAFS spectra show variations in the π^* and σ^* peak intensities depending on the x-ray incidence angles and the orientation of the system if we use linearly polarized synchrotron radiation [22]. NEXAFS has successfully been applied to the electronic structure analysis of *h*-BN [23] and nitrogen-substituted graphite [24]. Therefore, this spectroscopy has a great advantage in providing information on the orientation of graphite-like B-C-N hybrids.

In the present work, B-C-N hybrid thin films were prepared by ion beam deposition on highly oriented pyrolitic graphite (HOPG) at various temperatures, and the films were characterized by XPS and NEXAFS spectroscopy. The electronic and geometrical structures of synthesized B-C-N hybrids will be discussed on the basis of the XPS core-level shifts and the polarization dependencies of the NEXAFS spectra.

2. Experimental

2.1 Preparation method, precursor and target

It is very important to select the appropriate precursors and method both in the formation of the planned network and in the avoidance of un-wanted side reactions and contaminations. There were some reports which showed the synthesis of B-C-N hybrids [25-36]. Considerable efforts in the synthesis of B-C-N hybrids have been made by a large variety of deposition methods such as ion beam assisted deposition [28,29,37], laser ablation [38], chemical vapor deposition [29,37,38], pulsed laser

deposition [2], radio frequency reactive sputtering [38], reactive DC magnetron sputtering [39], microwave plasma with radio frequency (RF) bias enhancement (MW-PECVD), and direct current glow discharge plasma system (GD-PECVD) [40]. However, the quality of the samples has not been drastically improved in these methods. To our knowledge, there have been no report which shows the synthesis of single-phase B-C-N hybrid. Then, the synthesis method of B-C-N hybrids is still under development.

As precursors of B-C-N hybrid synthesis, many kinds of molecules and gas mixtures have been attempted such as $BCl_3 + CCl_4 + N_2 + H_2$ [31], $C_2H_2 + NH_3$ [32], $BCl_3 + CH_3CN$ [33,34], $NH(CH_3)_2{:}BH_3 + NH_3 + C_2H_4$ [35], $B + N_2$ [36], $N_2 + CH_4 + Ar$ [28,29], and borazine + NH_3 [30]. As substrates of B-C-N hybrid films, some kinds of solids have been used such as *h*-BN [25-27], B_4C [28-29], graphite [25-29,36], p-type Si(100) [28,29], and nanocrystalline diamond [30].

In the present work, we applied ion beam implantation method, because we can precisely control the composition of the films by changing the fluence of the ion beam. As a precursor, we chose borazine because this molecule has benzene-like structure (Fig.5) and it is molecular analogue of h-BN. The fragment ions which were produced by the discharge of borazine were implanted in HOPG at various temperatures.

2.1.1 Ion Beam implantation (IBI)

Ion beam implantation (IBI) method has been widely used in the synthesis of thin films [41-45]. It is one of the promising methods to synthesize B-C-N hybrid thin films. The schematics of the borazine implantation on HOPG and the mechanism of film growth are shown in Fig. 4.

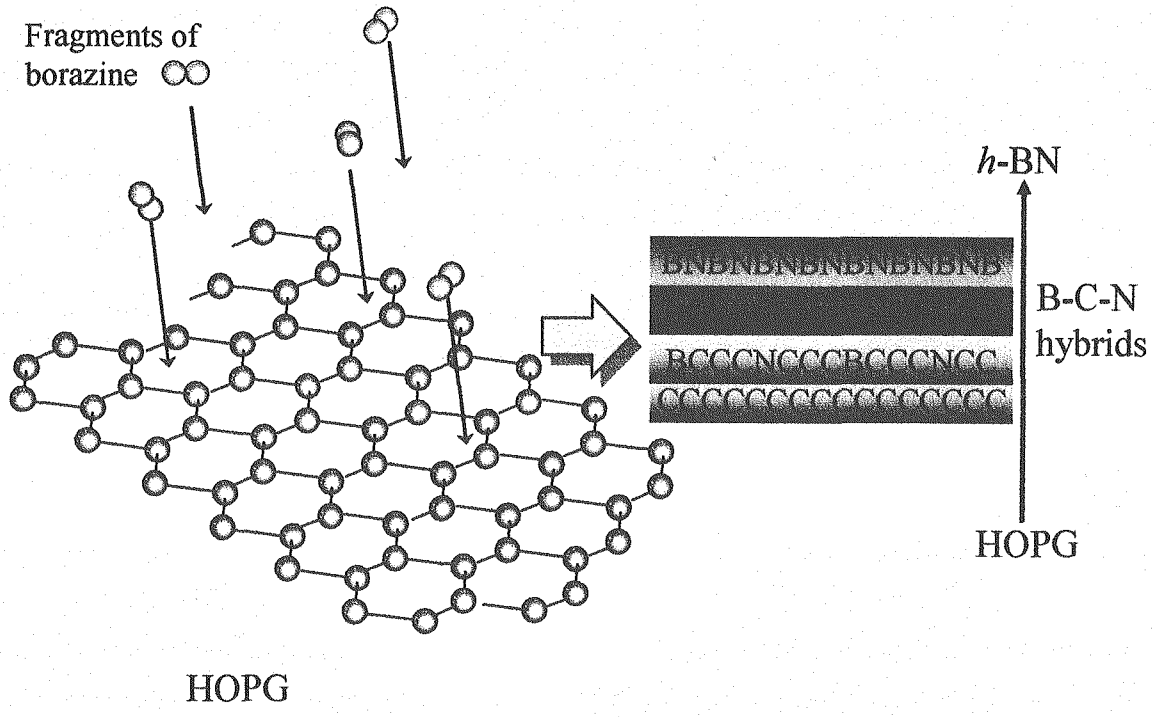

Fig. 4. Borazine ion beam implantation on graphite and the mechanism of film growth.

IBI has many merits in the film synthesis such as (i) removal of contamination (e.g. oxygen), (ii) non-equilibrium process → formation of novel materials, (iii) thin film formation using low-energy ion, and (iv) easiness to control composition by ion fluence.

2.1.2 Target and precursor

HOPG (Union Carbide) of 12 mm × 12 mm in size was used as a target. The structure of HOPG is shown in Fig. 2. It was cleaved *ex-situ* by using carbon tape and installed into ultrahigh vacuum (UHV) chamber.

Borazine as the precursor was available from Katchen Ltd., Czech Republic. The structure of borazine is shown in Fig. 5.

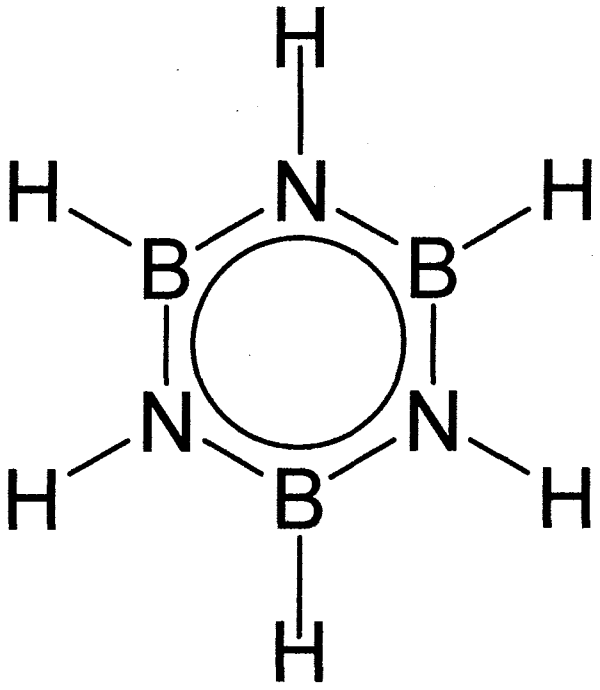

Fig. 5. The structure of borazine ($B_3N_3H_6$); MW: 80.51, chemical purity: min. 98 %, melting point: -56 °C, boiling point: 55 °C, density: 0.86 g / ml at 25 °C, vapor pressure: 210 Torr at 20 °C, and flash point: 1.7 °C.

Borazine is flammable liquid which may be decomposed by water, alcohol, acid, light, and heat. Details of its stability are described as follows:

1. Thermal stability: Extensive decomposition can occur when stored at ambient temperature for period longer than one month. Decomposition appears to be autocatalytic. Negligible decomposition when stored at below 0 °C.
2. Stability to air: Stable in dry air but reacts with trace amount of atmospheric moisture. Slow reaction with liquid water to form H_2, NH_3 and boric acid.
3. Stability to light: Slow polymerization may occur by light. Hydrogen is formed as a by-product.

Carbon dioxide or dry chemicals can be used as fire extinguisher. It may cause burns to skin, eyes and respiratory system. Borazine was stored below 0 °C to avoid degradation. Borazine was first purified by vacuum sublimation at liquid nitrogen temperature and then implanted on HOPG. Mass spectroscopic observation of the fragment ion species of borazine plasma and its purity will be discussed in section 3.2.

2.2 Experimental setup and characterization of thin films

2.2.1 Experimental setup

All the experiments were performed at the Photon Factory (PF) of High Energy Accelerator Research Organization (KEK), Tsukuba, Japan. Two setups were used in the experiments for two different synchrotron beam lines. The reaction chambers for sample transfer and epitaxial growth of thin films were developed during this work.

In Case I of this study, experimental setup, located in the beamline BL-27A, was employed. The schematics of the experimental setup is shown in Fig. 6. The UHV chamber was equipped with electron energy analyzer, sample preparation and transfer chamber, ion gun, YAG laser, quadrupole mass spectrometer (QMS) (ULVAC MSQ-1000), and MgK_α and AlK_α x-ray sources. The base pressure of the UHV chamber was ~10^{-8} Pa. The reaction chamber was connected to the SR with x-ray ranges from 1.8 to 5 keV.

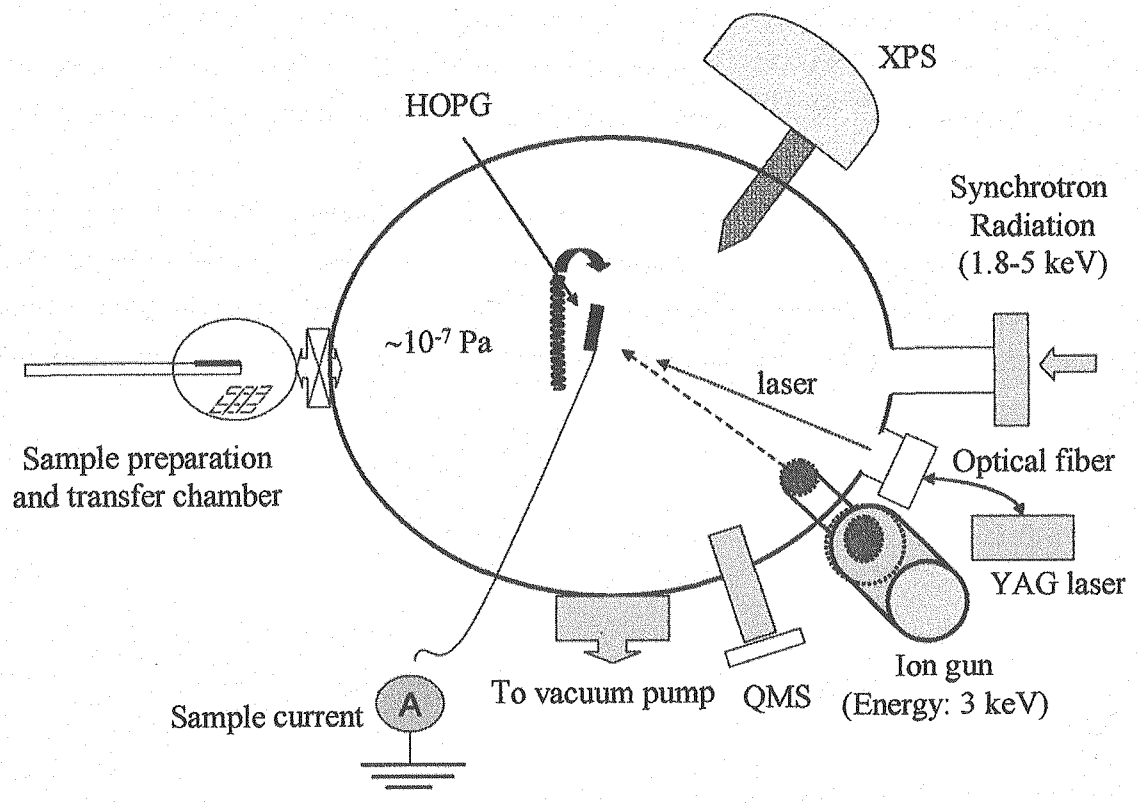

Fig. 6. Schematic illustration of the experimental setup located in beamline (BL) 27A, KEK-PF. The UHV chamber is equipped with electron energy analyzer, sample preparation and transfer chamber, ion gun, YAG laser, QMS, MgK_α and AlK_α x-ray sources, and SR with x-ray ranges from 1.8 to 5 keV.

Fragment ions of borazine plasma were obtained by cold-cathode penning-ionization gauge (PIG) ion source and then implanted on the target with accelerating voltage of 3.0 kV. Borazine ion implantation was performed with the typical pressure of ~10^{-4} Pa at RT, 600 °C, and 850 °C. The target was heated by using YAG laser. Ion implantation was carried out at normal incidence while laser irradiation was performed simultaneously from the front side of the target. The surface temperature was monitored by optical pyrometer. Surface composition of the implanted films and chemical condition of the local structures were studied by XPS. XPS was carried out *in-situ* in the same UHV chamber with ion implantation. A hemispherical-type electron energy analyzer (VSW, CLASS100) was used. Mg$K\alpha$ x-ray source was also used for XPS measurements. Binding energies

(E_b^F) relative to the Fermi level were calibrated by Au($4f_{7/2}$) photoelectron peak (E_b^F = 84.0 eV). Composition ratio of the films was determined from the XP peak intensity ratio. XP spectra of a pyrolitic BN (*p*-BN, Advanced Ceramics International Co.) and a HOPG were also measured as references.

In Case II of this study, experimental setup, used in BL11A, was employed. It is shown in Fig. 7. The UHV chamber of that experimental setup was equipped with electron energy analyzer, sample preparation and transfer chamber, ion gun, electron bombardment heating system, and QMS (Stanford Research System RGA200). This reaction chamber was connected to the SR with x-ray ranges from 70-1900 eV.

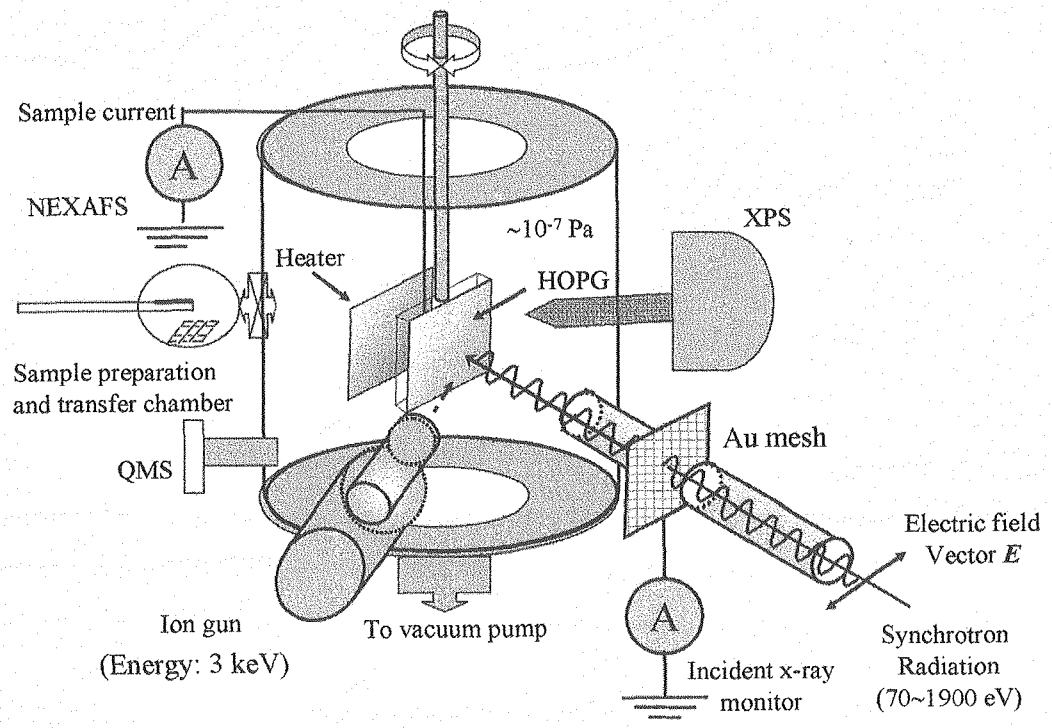

Fig. 7. Schematic illustration of the experimental setup used in beamline (BL) 11A, KEK-PF. The UHV chamber is equipped with electron energy analyzer, sample preparation and transfer chamber, ion gun, electron bombardment heater, QMS, and SR with x-ray ranges from 70-1900 eV.

The photograph of the experimental system is also shown in Fig. 8.

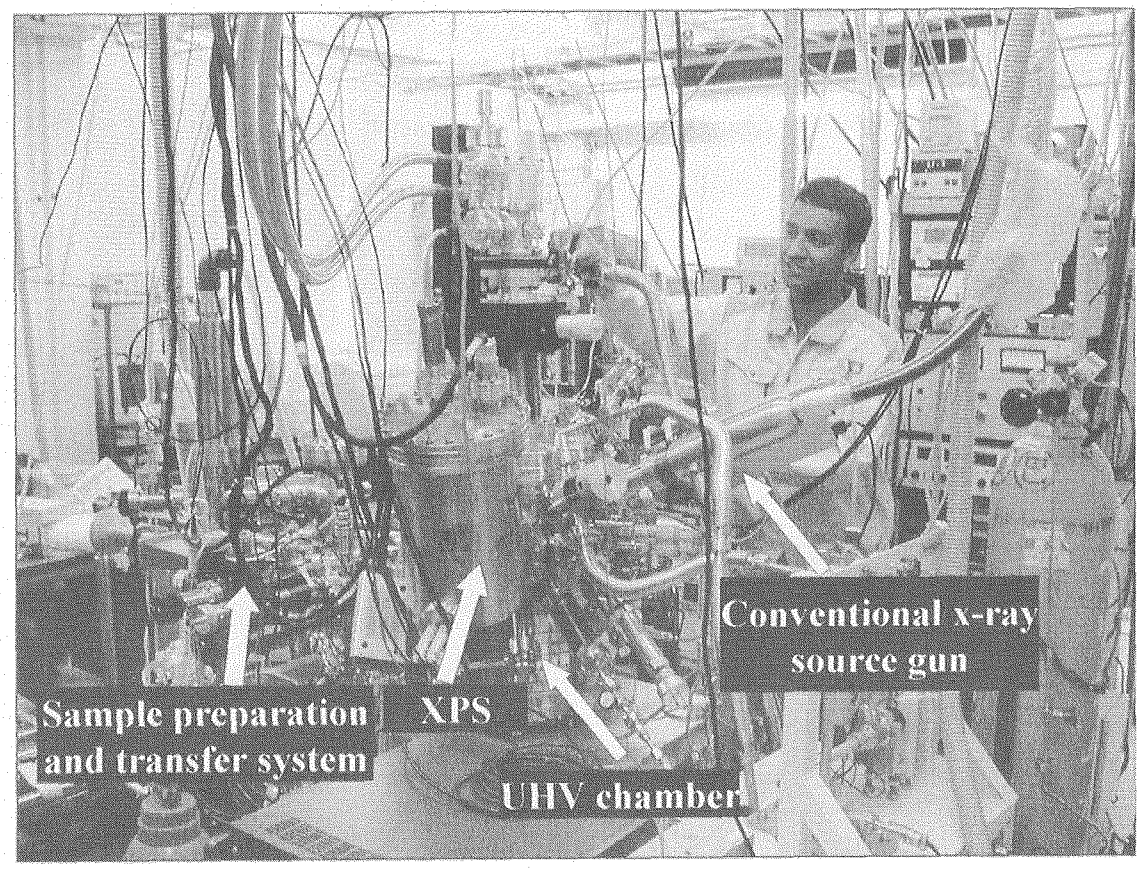

Fig. 8. The photograph of the experimental system.

Borazine ion implantation was performed with the typical pressure of ~10^{-4} Pa at RT and 800 °C. The target was heated by electron bombardment. Ion implantation was carried out at normal incidence while heating was performed simultaneously from the backside of target (HOPG). The surface temperature was also monitored by optical pyrometer. The films were characterized *in-situ* by polarization-dependent NEXAFS in order to study the geometrical and electronic structures of the B-C-N hybrid thin films. Surface composition of the implanted films and chemical condition of the local structures were studied by XPS. XPS measurements were carried out *in-situ* in the same UHV chamber by a sector-type analyzer (VG, CLAM2). Soft x-rays emitted from the beamline were used for XPS measurement. The photon energy was in the range of 500-700 eV.

2.2.2 XPS analysis

XPS is one of the element specific analysis techniques. When x-ray is absorbed, core electron is ionized. Therefore, electronic structure of core level relative to Fermi level (FL) is clarified as shown

in Fig. 9. The chemical environment of the system can be inferred from the chemical shift of core level. This is an indirect method to study the chemical condition.

For a conductive sample in electrical contact with the spectrometer, conservation of energy leads to the Eq. 1;

$$h\nu = E_K + \phi + E_B^F \quad \cdots\cdots\cdots\cdots\cdots\cdots\cdots\cdots (1)$$

where, $h\nu$ is the energy of the exciting x-ray photon, E_K is the kinetic energy of the emitted electrons, ϕ is the work function of the spectrometer, and E_B^F is the electron binding energy (BE) relative to the Fermi level (FL) of the sample. Mg$K\alpha$ ($h\nu$ = 1253.6 eV) was used as the exciting x-ray source. Work function was fixed value for the spectrometer. BE was calculated automatically from measured E_K, based on Eq. 1. The BE was applied to study the chemical bond.

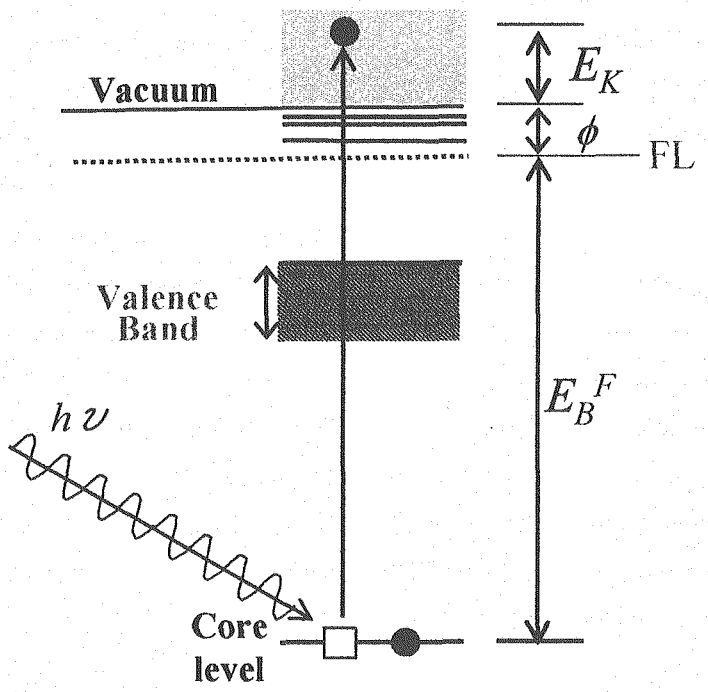

Fig. 9. Schematic of the processes involved in XPS. The $h\nu$, E_K, E_B^F, and ϕ are the energy of the exciting x-ray photon, kinetic energy, electron binding energy relative to the Fermi level (FL) of sample, and work function of the spectrometer, respectively.

2.2.3 Near edge x-ray absorption fine structure analysis

2.2.3.1 Introduction

The theoretical background of the NEXAFS technique is briefly discussed in this section. NEXAFS is also sometimes referred to as x-ray absorption near edge structure (XANES). It typically represents

the energy region from the absorption edge to about 50 eV above the edge [22]. X-ray absorption spectra (XAS) are generally characterized by many fine spectral features near the absorption edge. NEXAFS spectra provide important information about the electronic and structural properties of molecules on surfaces.

NEXAFS is ideally suited for studying adsorbed molecules for several reasons: (1) X-ray absorption occurs because of the excitation of core electrons. It makes this technique element specific. (2) NEXAFS features are very sensitive to the local electronic structures of adsorbates. It in turn provides information on the degree of interaction between the surface and adsorbates. (3) NEXAFS excitations are governed by the dipole selection rule. We can know the orbital components of valence unoccupied states. (4) In NEXAFS excitation, transition probability depends on the direction of electric field vector of the incident x-rays. It allows the determination of molecular orientation by varying the incidence angles of the polarized synchrotron beam. (5) Because of the brightness of the synchrotron source, NEXAFS measurements can be readily carried out for adsorbates even at sub-monolayer coverages.

2.2.3.2 Synchrotron radiation

Synchrotron radiation (SR) is required for NEXAFS measurement. SR is a highly intense, stable, collimated, continuous, polarized, and pulsed electromagnetic radiation. SR is generated when charged particles (electron or positrons) moving at relativistic speeds, is deflected by a magnetic field with a large radius of curvature. The deflection can be achieved either by bending magnets (circular motion) or by periodic magnetic structures (sinusoidal motion) [46-49]. In general, SR covers a wide range of electromagnetic spectrum from infrared region through visible, ultraviolet, soft x-ray to hard x-ray region. These characteristics are essential for achieving reliable and high quality NEXAFS measurements.

2.2.3.3 Basic principles of NEXAFS

Because NEXAFS measurements involve the excitation of electrons from a core level to partially filled and empty levels, the peak positions and spectral lineshape in a NEXAFS spectrum are directly related to the nature of unoccupied electronic levels. The mechanism of NEXAFS is explained schematically in Fig. 10. An example of typical NEXAFS spectrum for B-C-N thin films is also shown in Fig. 10.

When monochromatic x-ray emitted by SR is irradiated to a system, core electron is ionized. If the energy of x-ray is tuned at the core-to-valence resonance energy of the target element, the core electrons are excited to unoccupied levels of the system. In the case of molecules having double or

triple bonds, the lowest unoccupied molecular orbital is typically an unoccupied π^* orbital, which is followed by a set of Rydberg states (not shown in Fig. 10) just below the vacuum level, and then by an unoccupied σ^* molecular orbital at energies above the vacuum level. Assuming that transitions of the core level (1s electrons) to all empty orbitals are allowed, the corresponding NEXAFS spectrum is illustrated in the Fig. 10 (b), where the absorption intensity of x-ray photons is plotted as a function of photon energy. The NEXAFS spectrum for molecules having double or triple bonds is characterized by a π^* resonance at energies below the ionization potentials (IP), which reflects the energy difference between core level and the vacuum level. In addition, a σ^* resonance is observed as a relative broad feature at energies above IP.

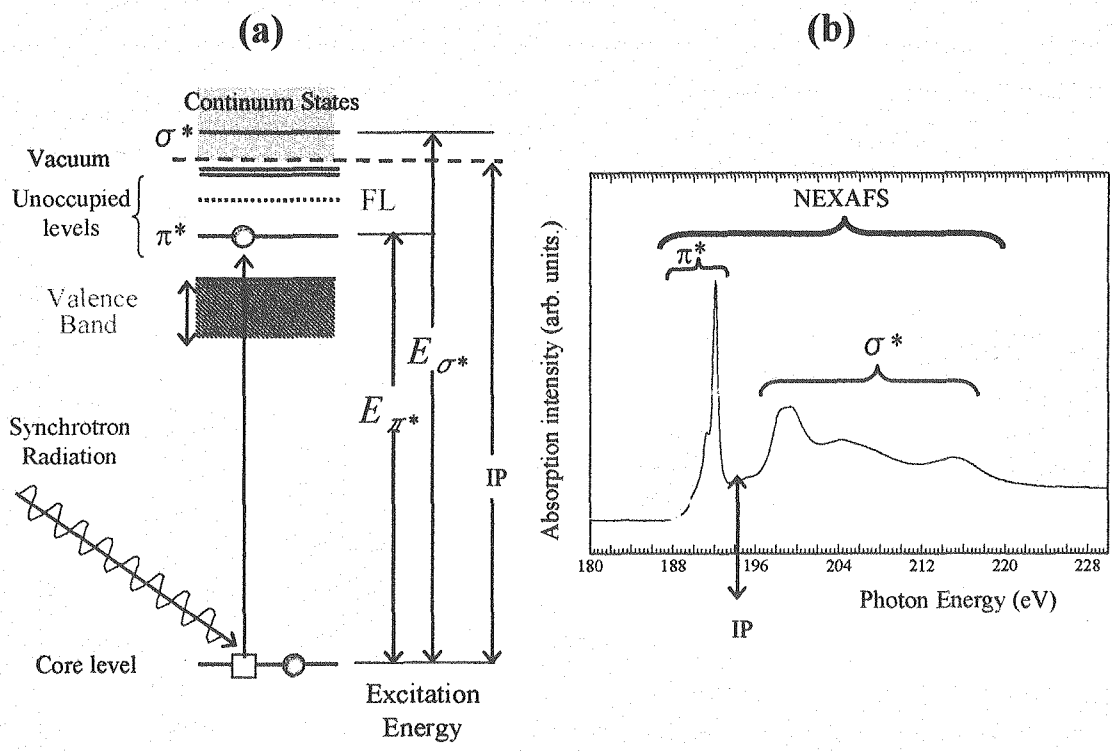

Fig. 10. (a) Schematic of the processes involved in NEXAFS for unsaturated compounds with double or triple bonds. IP is ionization potential and E_{π^*} and E_{σ^*} are the excitation energies of the electrons from core level to unoccupied levels, π^* and σ^*, respectively and (b) a typical NEXAFS spectrum which shows two features, π^* and σ^*.

NEXAFS measurements provide direct information about the nature of the empty molecular orbitals by probing the excitation of core electrons to unoccupied levels. Because of the number of

empty molecular orbitals and their energy positions are characteristic for different chemical species, NEXAFS spectra can be used as "fingerprints" for identifying molecular species. Furthermore, because NEXAFS measurements involve dipole transitions between well-defined initial and final states, the application of the dipole selection rule often provides information about the local symmetry of the molecules [22].

NEXAFS is an element specific analysis technique and gives information regarding configuration of local structure and orbital orientation of the system. These are discussed below.

2.2.3.3.1 Element specific analysis

A schematic illustration of inner shell excitation spectrum is shown in Fig. 11. Due to the core level difference, absorption edges of different elements are separated each other. This allows extracting an electronic structure around a specific element. Therefore, this is useful to characterize a complex system which includes plural elements.

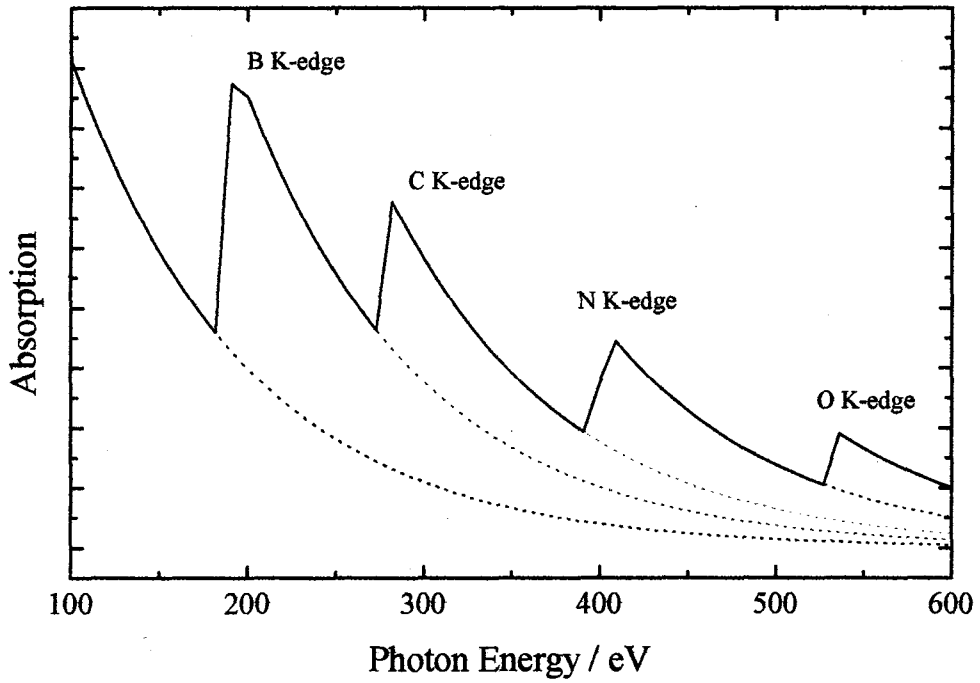

Fig. 11. Schematic illustration of inner shell excitation spectrum. Absorption edges of B, C, N, and O are separated each other due to the core level difference.

The excitation energies of the absorption edges in the NEXAFS K-edge region are typically within a few eV of the binding energies for the corresponding 1s electrons, and are approximately at 193 eV for B, 285 eV for C, 400 eV for N, and 530 eV for O. These excitation energies are in the range of the so-called soft x-ray regime, which generally represents photon energies below 1000 eV.

2.2.3.3.2 Configuration of local structure

NEXAFS reflects the bonding configuration of local structure. Two kinds of bonding configurations are shown in Fig. 12.

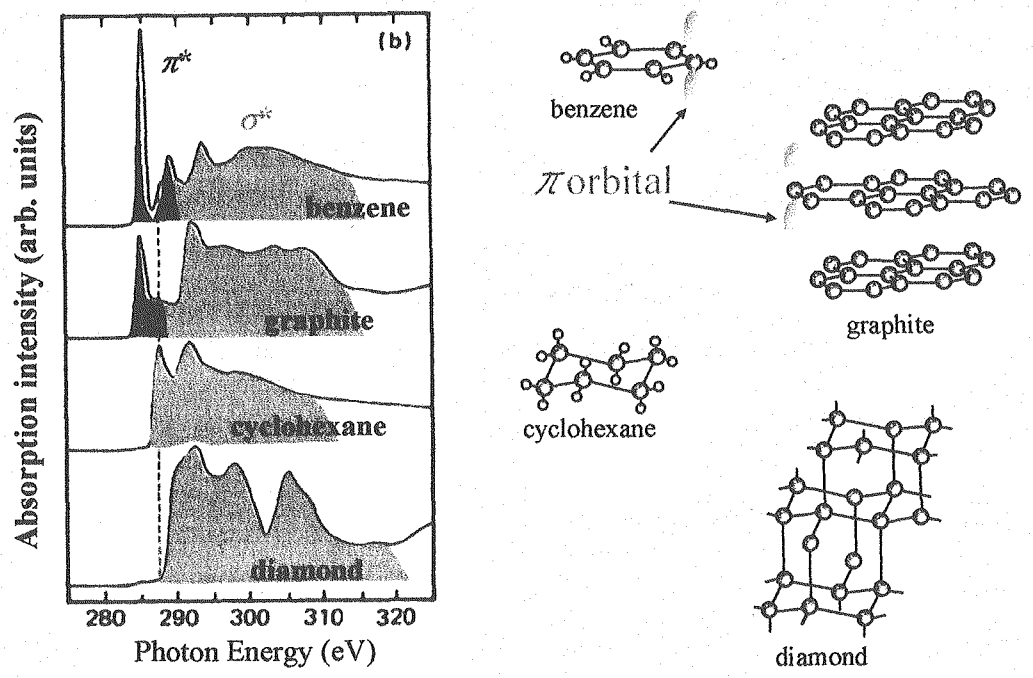

Fig. 12 Bonding configuration of local structure by NEXAFS. The sp^2 and sp^3 bonding configurations are elucidated in this figure.

Benzene and graphite have sp^2 configuration whereas cyclohexane and diamond have sp^3 configuration. The NEXAFS spectra of benzene and graphite show discrete π^* resonances in the low energy region. On the other hand, the spectra of cyclohexane and diamond show no π^* resonance. So, the bonding configuration of the systems can be distinguished by the feature of NEXAFS.

2.2.3.3.3 Orbital orientation

Another characteristic of NEXAFS is to study orientation of the system. Orbital orientation can be clarified from the polarization dependence measurement of NEXAFS spectrum. The details of polarization dependence of NEXAFS spectrum will be discussed in section 2.2.3.4.4.

2.2.3.4 NEXAFS experiment

Some of the most fundamental aspects in the NEXAFS measurements are briefly discussed in this section. These include the excitation process in x-ray absorption, the experimental means of detecting the x-ray absorption event, the dependence on the polarization of the incident photon beam, and the commonly used methods for the normalization of NEXAFS spectrum. A much more detailed discussion on these subjects is provided by Stöhr [22].

2.2.3.4.1 X-ray absorption cross section

The probability of exciting an electron, from an initial state ϕ_i to a final state ϕ_f, by x-ray photons is typically described in terms of the x-ray absorption cross section, σ_x. It is defined as the number of electrons excited per unit time divided by the number of incident photons per unit time per unit area [22]. It has the dimension of (length)^2 and is typically given in the unit of cm^2. Basically, σ_x can be described as: [22,50,51]

$$\sigma_{\mathrm{x}} = \frac{4\pi^2 h^2}{m^2}\frac{e^2}{hc}\frac{1}{h\omega}\zeta(E)\left|\langle\phi_{\mathrm{f}}\left|\mathbf{e}\cdot\mathbf{p}\right|\phi_{\mathrm{i}}\rangle\right|^2\delta(h\omega + E_{\mathrm{i}} - E_{\mathrm{f}}), \qquad \cdots\cdots \qquad (2)$$

Where, h, ω, e and m are the Planck's constant, frequency of the incident photon, the charge and mass of electrons, respectively. $\zeta(E)$ is the energy density of the final state, $|\langle\phi_f|\mathbf{e}\cdot\mathbf{p}|\phi_i\rangle|$ is the dipole matrix, and $\delta(h\omega+E_i-E_f)$ is the delta function for the conservation of energy. The terms $\mathbf{e}$, $\mathbf{p}$, E_i, and E_f are the unit vector in the direction of the incident x-ray photons, the linear momentum operator of electrons, and initial and final kinetic energy of photoelectron, respectively. The theoretical treatment of Eq. (2) has been discussed in details in several reviews [22,51]. The importance of several terms in Eq. (2), only qualitatively, is given below:

(1) The presence of the dipole matrix term, $|\langle\phi_f|\mathbf{e}\cdot\mathbf{p}|\phi_i\rangle|$, reveals the importance of an effective interaction between the sum of $\mathbf{e}$ and the sum of $\mathbf{p}$. The dipole matrix term is the theoretical

basis for the polarization dependence NEXAFS measurements that are often used for the determination of molecular orientation of adsorbates on surfaces [22,52-54]. In addition, the nature of the dipole transition also implies that the NEXAFS excitation should obey the dipole selection rule, which states that the change in angular momentum quantum number should be $\Delta l = \pm 1$ between the initial and final states. Therefore, for K-edge transitions (from an initial s state) the final states should have contributions from p orbitals. Similarly, for L-edge transitions (from an initial p state) the final states can be either s or d orbitals.

(2) The x-ray absorption cross section is proportional to the energy density of the final state $\zeta(E)$, which qualitatively explains the direct correlations between a NEXAFS spectrum and the nature of the unoccupied states.

(3) In principle, the delta function in Eq. (2) is only valid for a final state with infinite lifetime. For a more quantitative analysis, it should be replaced by a Lorentzian to account for finite lifetime of the final states [51]. This is an important point since the life time of a bound resonance state is often several orders of magnitude longer than a continuum resonance state [22].

(4) The intensity for a resonance transition is often expressed by a dimensionless term, optical oscillator strength, f, which is related to the x-ray absorption cross section in Eq. 2 by [22,55]:

$$\sigma_x(E) = \frac{2\pi^2 e^2 h}{mc}\frac{df}{dE} \qquad \cdots\cdots (3)$$

In other words, the resonance intensity (oscillator strength) in NEXAFS is the energy integral of the x-ray absorption cross section. Therefore, Eqs. 2 and 3 are used as the theoretical basis of the absorption intensity in NEXAFS and the molecular orientation of B-C-N hybrids.

2.2.3.4.2 Experimental detection of x-ray absorption

Schematic illustration of creation and annihilation of a core hole as a result of x-ray absorption is shown in Fig. 13. A and B represent two core levels of a sample. The energy zero is chosen at the Fermi level E_F [22].

The absorption of an x-ray photon, with a resonance energy, gives rise to an electronic excitation from the core level to an unoccupied level. The $h\nu$ is the energy of the exciting x-ray photon. A core hole is created as a result of the resonance excitation. NEXAFS measurements are carried out by following the de-excitation process, which generates either an Auger electron or a fluorescence photon. Experimentally, NEXAFS spectra can be recorded by measuring either the electron yield or

fluorescence yield as a function of incident photon energy. In addition to Auger electrons, the absorption of x-rays also produces photoelectrons. The photoelectrons can originate from both core and valence states of all elements that are present in the chemical system, as long as the incident photon energy is above the binding energies of these states with respect to the vacuum level.

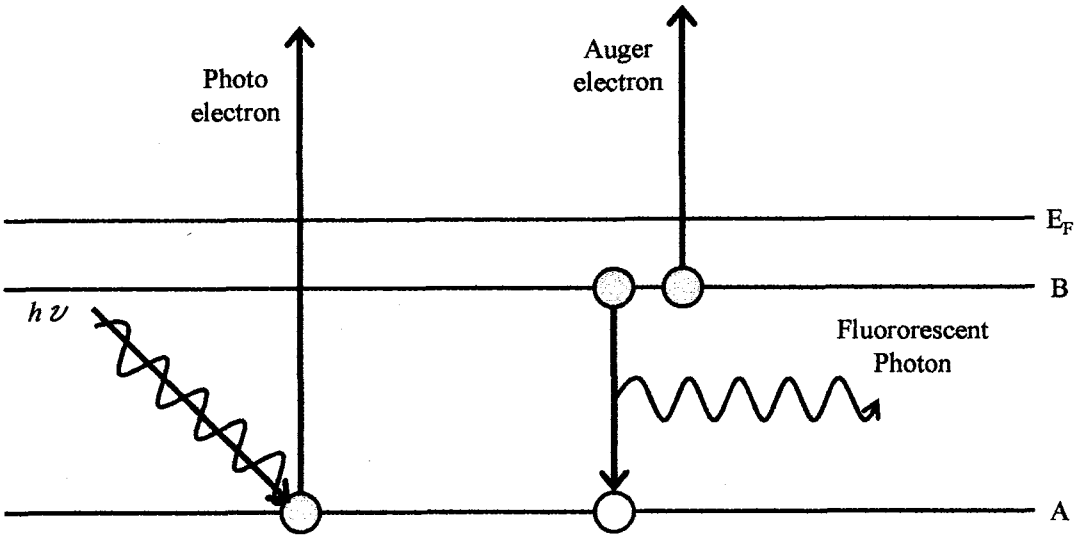

Fig. 13. Schematic illustration of creation and annihilation of a core hole as a result of x-ray absorption.

Based on the kinetic energies, electron yield measurements in NEXAFS can be carried out in three ways; Auger electron yield (AEY), partial electron yield (PEY) and total electron yield (TEY). The advantages, disadvantages and the experimental setup of the three methods have been discussed in detail by Stöhr [22]. One of the main differences among the three methods is the relative sensitivity to surface and bulk compositions. The surface sensitivity of each electron yield method is determined by the mean free path of electrons, which is governed by the kinetic energy, as shown in the so-called universal curve in Fig. 14 [56-58].

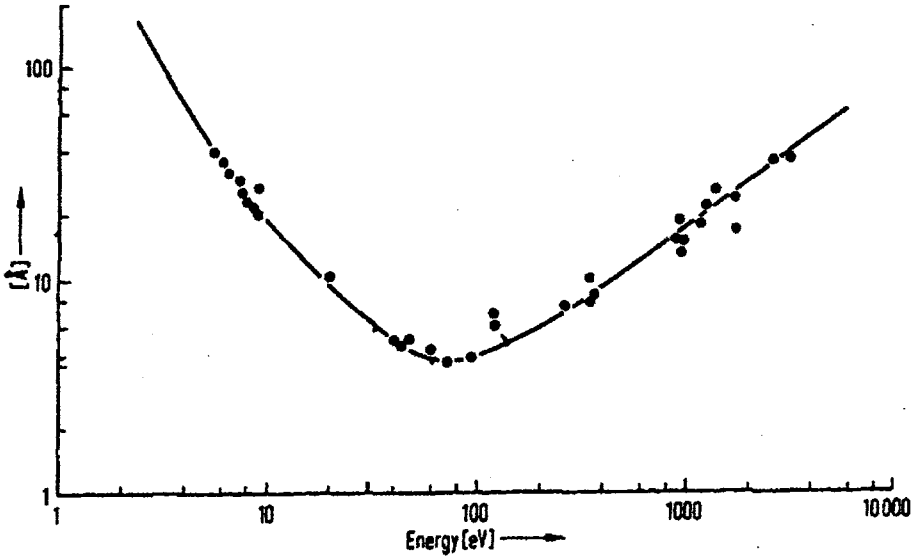

Fig. 14. Universal curve of electron mean free path as a function of kinetic energy. (From Ertl and Kiippers [56]; copyright Verlag Chemie.).

TEY measurement was employed in NEXAFS measurement which required UHV conditions. The TEY method measures the yield of all of the electrons emitted from sample surface triggered by photoelectrons and Auger electrons. The electron yield signals in TEY are dominated by the low energy electrons with kinetic energies below 20 eV [22]. Due to the large mean free paths of these low energy electrons, which are typically in the range of 50-100 Å as shown in Fig. 14, the TEY method is much more sensitive to the bulk compositions than to the top-most surface layers. Experimentally, the TEY setup is the easiest among the three; the electron detection can be achieved simply by collecting the signal with an electron channeltron multiplier [59].

2.2.3.4.3 Energy calibration, background correction and normalization of NEXAFS spectra

The NEXAFS spectrum of pyrolytic BN was measured as a standard spectrum of bulk *h*-BN. Photon energy of NEXAFS spectrum was calibrated by π^* peak of bulk *h*-BN, which was measured 192.1 eV for B K-edge and 401.3 eV for N K-edge [23]. All the NEXAFS spectra of the B-C-N hybrid

films were obtained by subtracting the background spectra (TEY spectra of HOPG) from those for the respective incidence angles.

The intensity of SR decays as a function of time, typically due to the decrease in the electron beam current in the storage ring. In addition, several other factors can also introduce changes in the radiation intensity as a function of photon energy [22], such as the energy-dependent reflectivity changes of the x-ray optics. Because the intensity of a raw NEXAFS spectrum depends directly on that of the synchrotron source, the time- and energy-dependent variation in the intensity of SR needs to be removed from NEXAFS data. This is commonly achieved by placing a fine gold grid directly in the optical path. The simultaneous measurement of photoelectron current from the reference gold grid provides the time- and energy-dependent variation in the radiation source. Typically, the normalization of NEXAFS data is achieved by dividing the raw NEXAFS spectrum by the concurrently measured reference grid signal. Furthermore, in NEXAFS investigations of adsorbed molecules at monolayer or submonolayer coverages, it is common to divide the normalized spectrum of the adsorbed layer by that of the clean surface. The division removes spectral contributions either from the substrate itself or from the interaction of x-ray source with impurities on the reference gold grid.

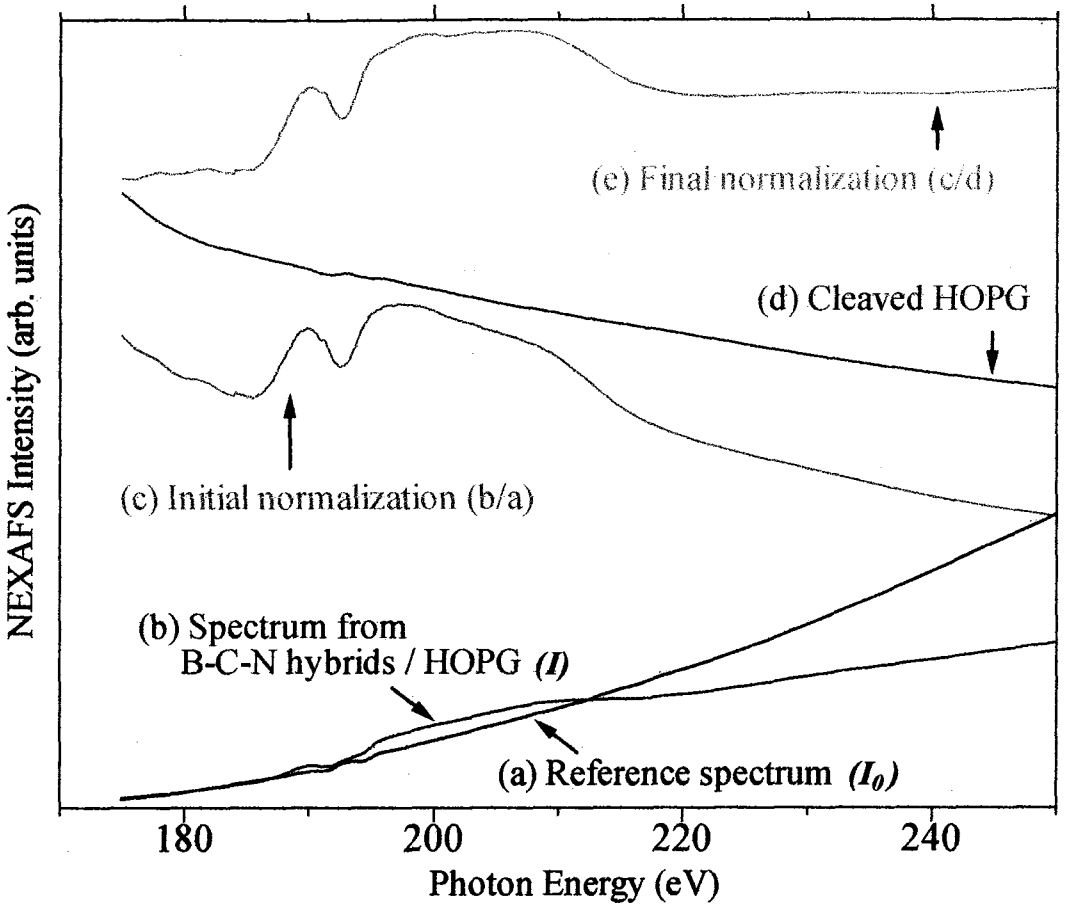

Fig. 15. Typical normalization procedure of a NEXAFS spectrum of B-C-N hybrids on HOPG at 800 °C. Spectra (a) and (b) are the time- and energy-dependent intensities measured from a reference gold grid and B-C-N hybrids/HOPG, respectively. Initial normalization of the spectrum (c) is obtained after dividing spectrum (b) by the reference spectrum I_0 (a). Final normalization of the spectrum (e) is obtained after dividing spectrum (c) by that of clean HOPG surface (spectrum (d)).

An example of normalizing the B K-edge NEXAFS data for B-C-N hybrids on HOPG is shown in Fig. 15. Spectra (a) and (b) are the raw NEXAFS data recorded concurrently for a reference gold grid and a B-C-N hybrids/HOPG, respectively. Intensity variations in both spectra resulting from the time- and energy-dependent behavior of the incident photon beam are removed after dividing spectrum (b) by spectrum (a). In addition, the remaining features from the HOPG in the initial normalized spectrum (c) can be removed after further dividing spectrum (c) by the clean HOPG spectrum (d).

2.2.3.4.4 Polarization dependence measurement

As discussed in section 2.2.3.4.1, the presence of the $|\langle\phi_f|\mathbf{e}\cdot\mathbf{p}|\phi_i\rangle|$ dipole matrix term in Eq. 2 implies that the x-ray absorption cross section, and therefore the resonance intensity (see Eq. 3), should depend on the polarization of the incident photons. More specifically, the feature of the NEXAFS clearly depends on the incident angle (θ) of x-ray. The incidence angle θ is defined as the angle between the electric field $\boldsymbol{E}$ of x-ray and the surface normal $\boldsymbol{n}$ of the sample which is shown in Fig. 16.

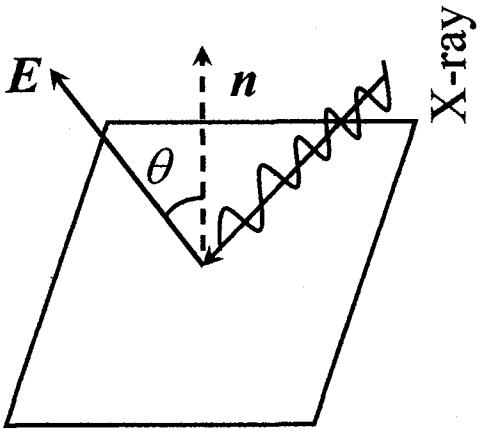

Fig. 16. The definition of the incidence angle θ, where E is the electric field of the x-ray and n is the surface normal.

The polarization dependence of the NEXAFS is described briefly in the following; [22]

$$I_{if} \propto |\boldsymbol{E}\cdot\boldsymbol{O}|^2 \propto \cos^2\delta \qquad \ldots\ldots\ldots\ldots\ldots\ldots(4)$$

where I_{if}, $\boldsymbol{O}$, *and* δ are the transition (or peak) intensity of NEXAFS (from initial to final states), vector of the final state orbital and angle between $\boldsymbol{E}$ and $\boldsymbol{O}$, respectively. C(1s) NEXAFS spectra of graphite at various incident angles (θ) of x-ray and the mechanism of polarization dependence of NEXAFS spectrum are shown in Fig. 17.

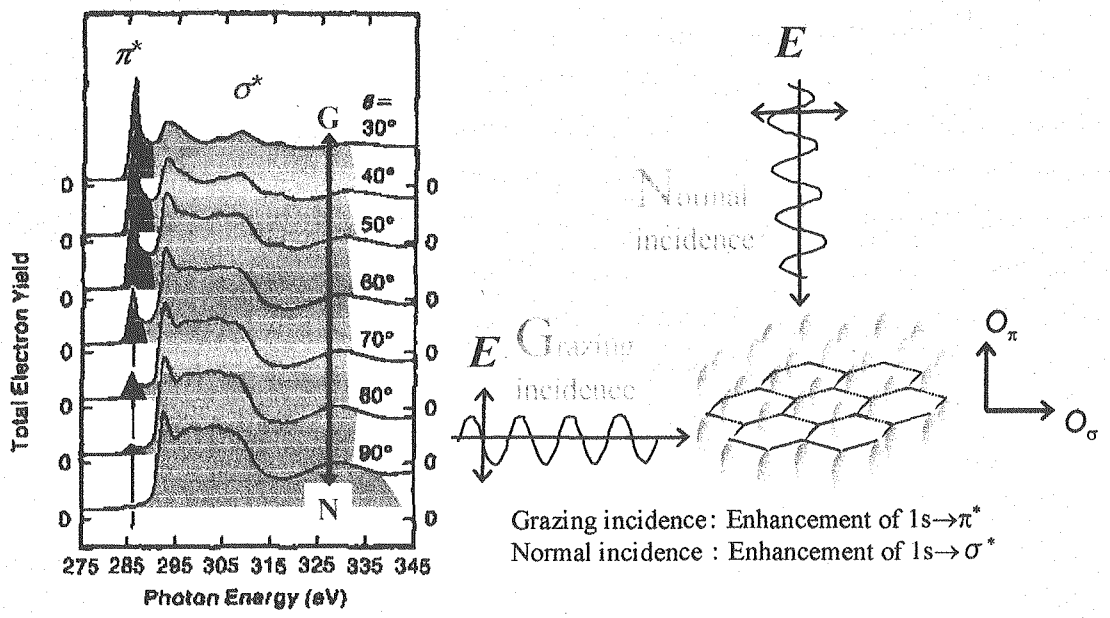

Fig. 17. C K-edge NEXAFS spectra of single-crystal graphite at various incident angles (θ) of x-ray and schematic illustration of the polarization dependence of NEXAFS spectrum where *E* and *O* are electric field vector and vector of the final state orbital, respectively.

When x-ray is incident on graphite with grazing angle, π^* peaks are enhanced while σ^* peaks are enhanced as the incident angle becomes large. This behavior is called polarization dependence. Since π^* orbital is just perpendicular to the surface of HOPG, *E* and π^* orbital have large projection at the grazing incidence. Consequently, the transition to π^* level is enhanced. On the contrary, *E* and σ^* orbital have large projection at the normal incidence, and then σ^* peaks are enhanced. Therefore, orientation of the system is clarified by measuring the polarization dependence of NEXAFS.

3. Results and Discussions

3.1 General Consideration

In the Case I of this study, B-C-N hybrid thin films were grown from ion beam plasma of borazine on graphite substrate at RT, 600 °C, and 850 °C. Laser beam was used for sample heating during the

implantation. Surface composition and chemical condition of local structures of the synthesized films were studied *in-situ* by XPS where MgK_α was used as x-ray source.

In the Case II of this study, B-C-N hybrid thin films were grown from ion beam plasma of borazine on graphite substrate at RT and 800 °C. Electron bombardment heating was used for sample heating during the implantation. Surface composition and chemical condition of local structures of the synthesized films were studied *in-situ* by XPS where SR x-ray was used as beam source. In order to clarify the existence of the graphite-like B-C-N hybrids, the thin films were characterized *in-situ* by NEXAFS. Polarization dependent NEXAFS was used to study the geometrical and electronic structures of the B-C-N hybrid thin films.

3.2 Residual gases of vacuum chamber and purity of borazine

The residual gases in the reaction chamber before borazine introduction were checked by QMS in order to confirm the cleanness of the reaction chamber. The purity of the borazine was also checked by QMS. The QMS spectrum of the residual gases in the reaction chamber before borazine introduction is shown in Fig. 18(a). The fragment ion species of borazine plasma are shown in Fig. 18 (b).

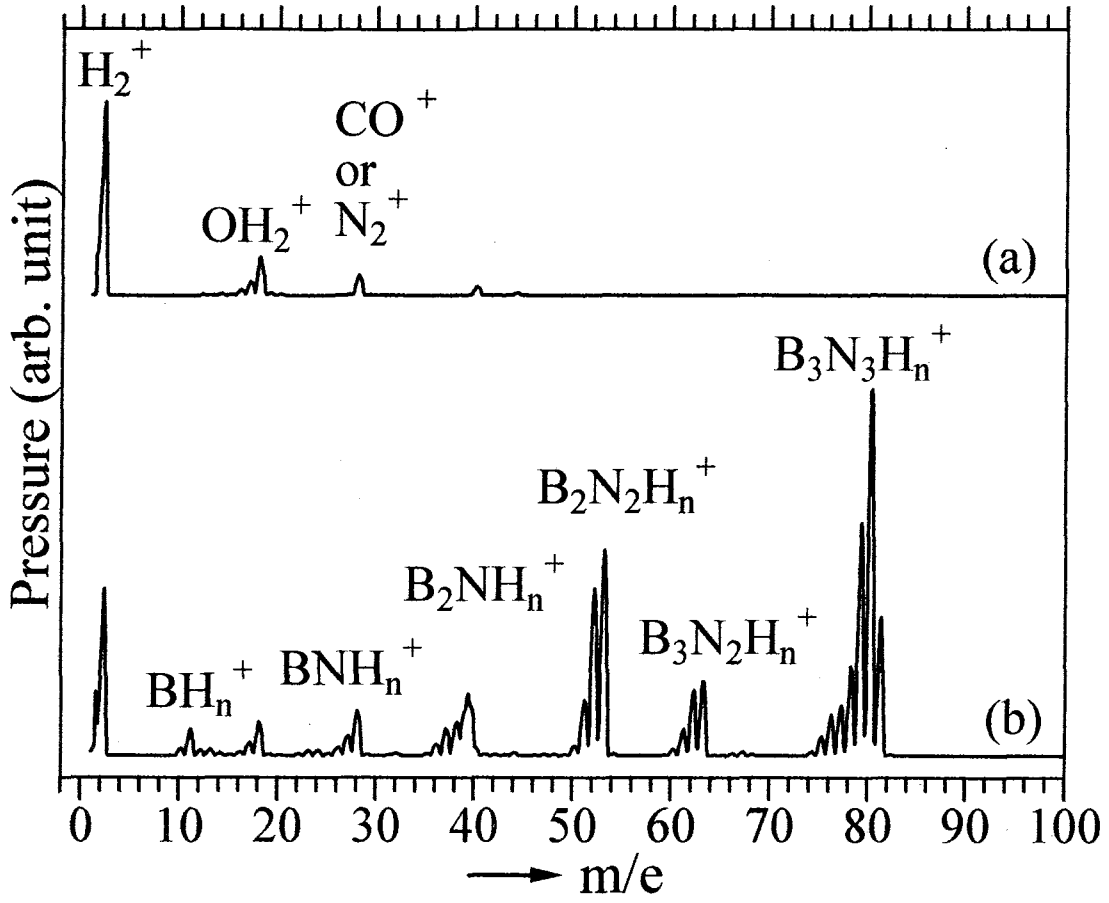

Fig. 18. Mass spectra (a) before and (b) after borazine gas introduction to the reaction chamber.

The peaks, in Fig. 18 (a), ascribed to the fragments related to water (m/e=16-18) and nitrogen or CO (m/e=28) were formed. They were so weak in comparison to the borazine related peaks (Fig. 18 (b)) that the reaction chamber was clean enough for decomposition of borazine. Spectrum of borazine matches to those reported for the cracking pattern of borazine [60]. As shown in Figs. 18(a) and 18(b), the intensities of water related fragments (*m/e* =16-18) remain constant after borazine introduction. This indicates that borazine is free from water and pure enough.

3.3 B-C-N hybrids prepared in BL27A UHV chamber

3.3.1 Work function of the spectrometer of BL27A system

Work function (ϕ) of the spectrometer should be calibrated in order to calculate the binding energy. Au($4f_{7/2}$) peak of which bonding energy is 84.0 eV was used for that calibration. Fig. 19 shows the XP

spectrum of Au using Mg Kα X-ray source ($h\nu$= 1253.6 eV). It shows the peak at 1165.6 eV, which is ascribed to Au($4f_{7/2}$).

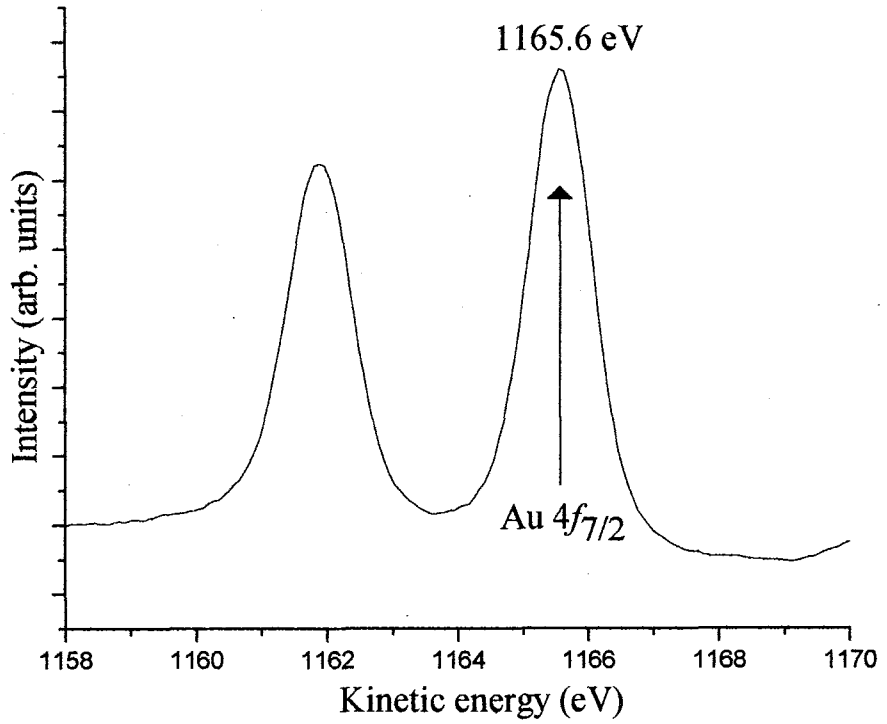

Fig. 19. XP spectrum of Au using Mg Kα x-ray source ($h\nu$= 1253.6 eV).

The following simple equation is used to calibrate the energy;

$h\nu$(Source energy) = E_K (Kinetic Energy) + ϕ (Work function) + E_B (Binding energy)

$$\phi = h\nu - E_k - E_b \quad \text{.....(5)}$$

Work function is calculated to be 4.0 eV. This value is used for the calculation of binding energy in XP spectra.

3.3.2 Composition and thickness

The composition ratio and the thickness of the deposited films are estimated from the wide scan XP spectra. Different composition ratios are estimated by the following simple equations;

$$\frac{[B]}{[N]} = \frac{\sigma_{N1s}(h\nu)}{\sigma_{B1s}(h\nu)} \times \frac{I_{B1s}}{I_{N1s}} \quad \cdots\cdots (6)$$

$$\frac{[B]}{[C]} = \frac{\sigma_{C1s}(h\nu)}{\sigma_{B1s}(h\nu)} \times \frac{I_{B1s}}{I_{C1s}} \quad \cdots\cdots (7)$$

$$\frac{[N]}{[C]} = \frac{\sigma_{C1s}(h\nu)}{\sigma_{N1s}(h\nu)} \times \frac{I_{N1s}}{I_{C1s}} \quad \cdots\cdots (8)$$

where $\sigma_{BIs}(h\nu)$, $\sigma_{NIs}(h\nu)$ and $\sigma_{CIs}(h\nu)$ are the photoionization cross sections of B(1s), N(1s) and C(1s) core levels and I_{BIs}, I_{NIs} and I_{CIs} are the intensities of photoelectron peaks, respectively. The cross sections at different x-ray sources are obtained from a reference [61].

The thickness t of the film is estimated by the following equation [62];

$$\frac{I_{N1s}}{I_{C1s}} = \frac{\sigma_{N1s}(h\nu)}{\sigma_{C1s}(h\nu)} \times \frac{\lambda_{N1s}(E_K)}{\lambda_{C1s}(E_K)} \times \frac{n_N}{n_C} \times \frac{1-\exp(-t/\lambda_{N1s}(E_K)\cos\theta)}{\exp(-t/\lambda_{C1s}(E_K)\cos\theta)} \quad \cdots\cdots (9)$$

where $\lambda(E_K)$ is ineleastic mean free path (IMFP) of photoelectron with kinetic energy E_K in the BN film, n is atomic density, and θ is an emission angle of photoelectron to the surface normal. The θ was 0° in this measurement. IMFP was estimated using the TTP-2M equation [63].

The wide scan X-ray photoelectron (XP) spectra of the films deposited at RT, 600 °C, and 850 °C are shown in Figs. 20-22, respectively.

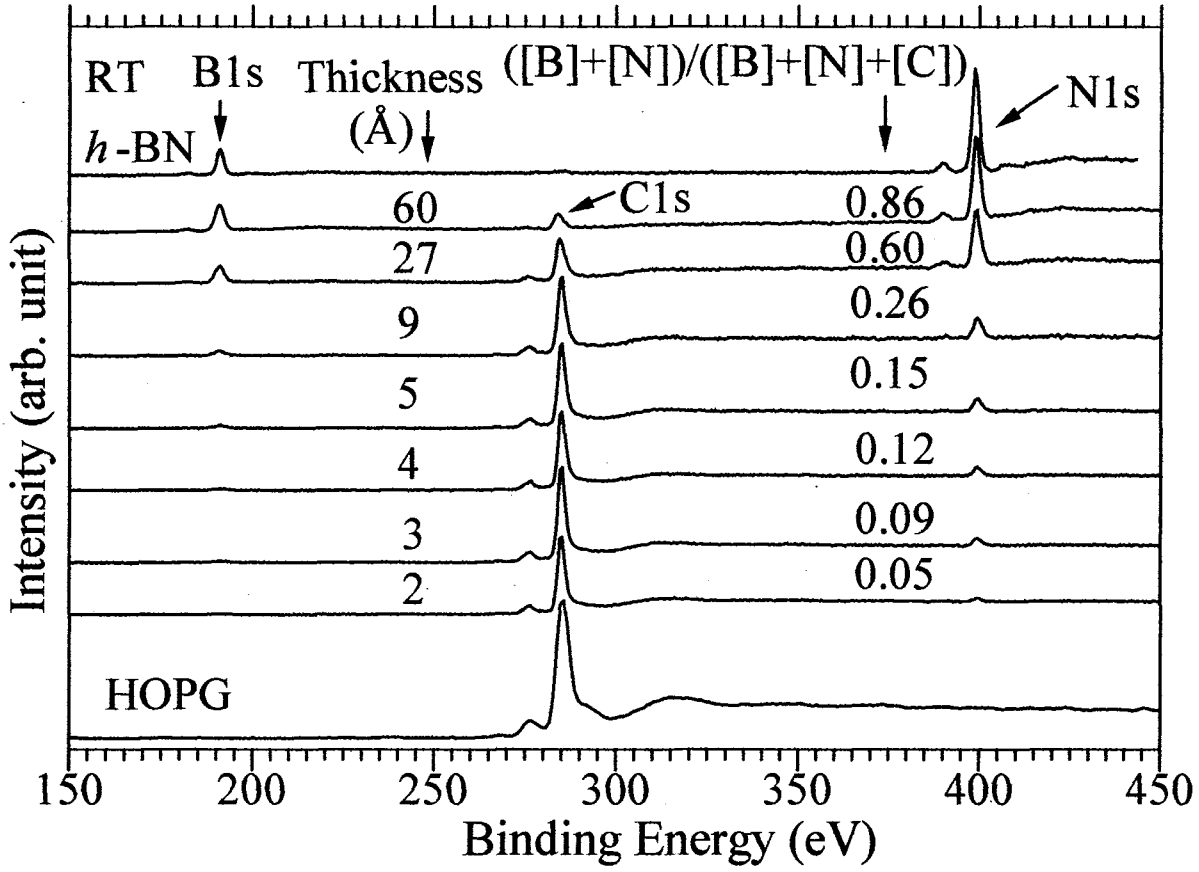

Fig. 20. XP wide scan spectra of B-C-N hybrid thin films at RT. Thickness and ([B]+[N]) / ([B]+[C]+[N]) ratio are shown at the left and right sides of each spectrum, respectively. Top and bottom curves show XP wide scan spectra of *h*-BN and HOPG, respectively.

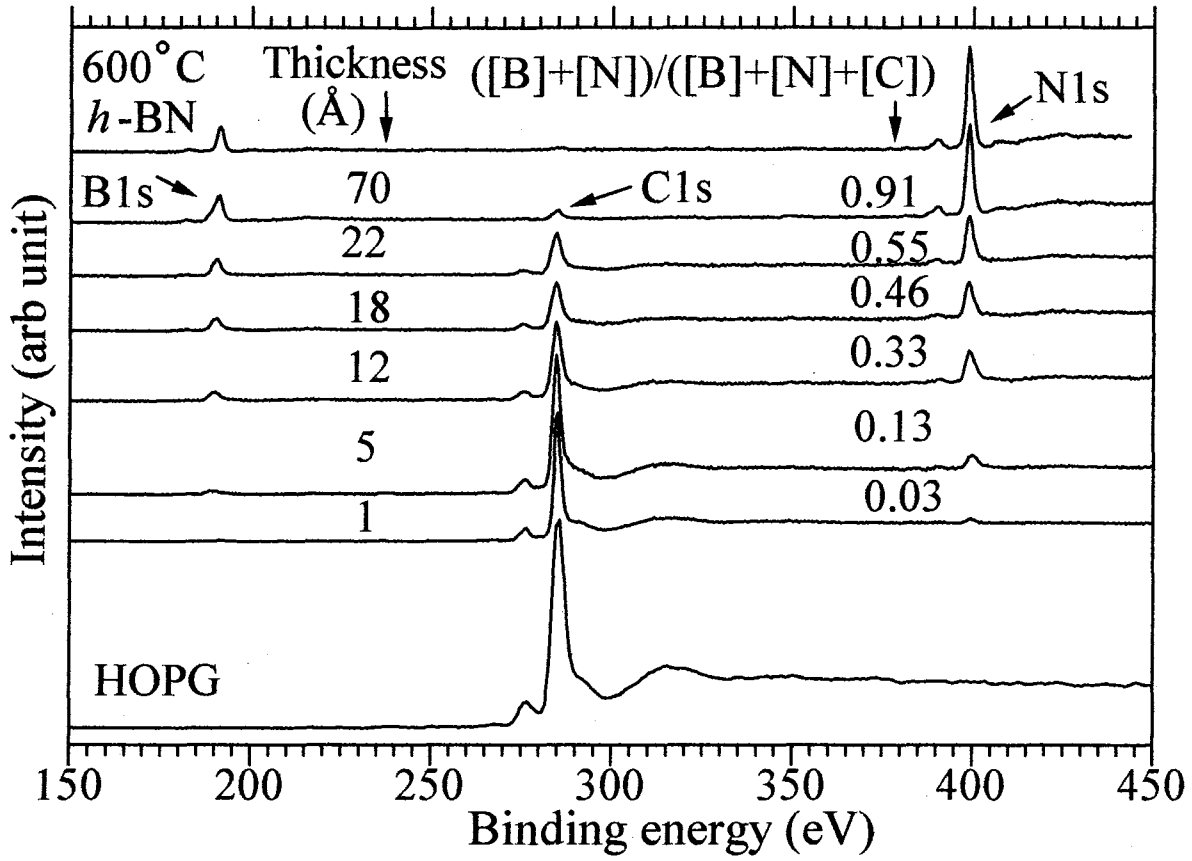

Fig. 21. XP wide scan spectra of B-C-N hybrid thin films at 600 °C. Thickness and ([B]+[N]) / ([B]+[C]+[N]) ratio are shown at the left and right sides of each spectrum, respectively. Top and bottom curves show XP wide scan spectra of *h*-BN and HOPG, respectively.

These spectra indicate that the films are composed of B, C, and N. Peak corresponds to oxygen at ~530 eV was not observed in the XP spectra, confirming no contamination with oxygen. Top and bottom curves in each figure show the results of *h*-BN and HOPG, respectively. Corresponding thickness and ([B]+[N]) / ([B]+[C]+[N]) ratio are shown on the left and right side in each curve, respectively.

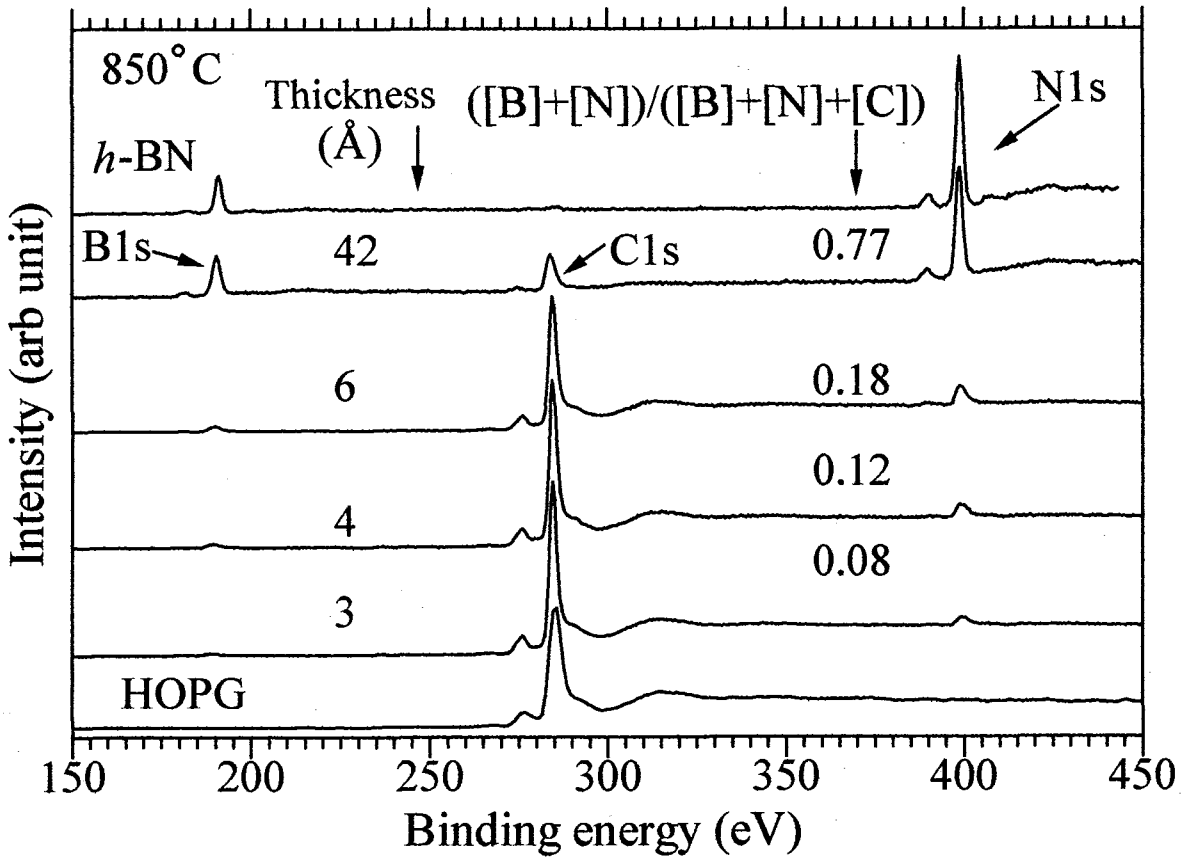

Fig. 22. XP wide scan spectra of B-C-N hybrid thin films at 850 °C. Thickness and ([B]+[N]) / ([B]+[C]+[N]) ratio are shown at the left and right sides of each spectrum, respectively. Top and bottom curves show XP wide scan spectra of *h*-BN and HOPG, respectively.

The intensity of the C(1s) peak decreases while B(1s) and N(1s) peaks grow with the increase in the thickness. The [B] / [N] ratio of the films synthesized at the highest fluence is close to that of bulk *h*-BN. This indicates that the nearly stoichiometric BN layer was finally formed as borazine plasma was deposited on HOPG surface.

3.3.3 Local structures of B-C-N hybrids

3.3.3.1 Local structures of B site

Figs. 23-25 show the B(1s) XP spectra at RT, 600 °C, and 850 °C, respectively. Each spectrum is deconvoluted into different peaks. Details of the peak assignments are explained below.

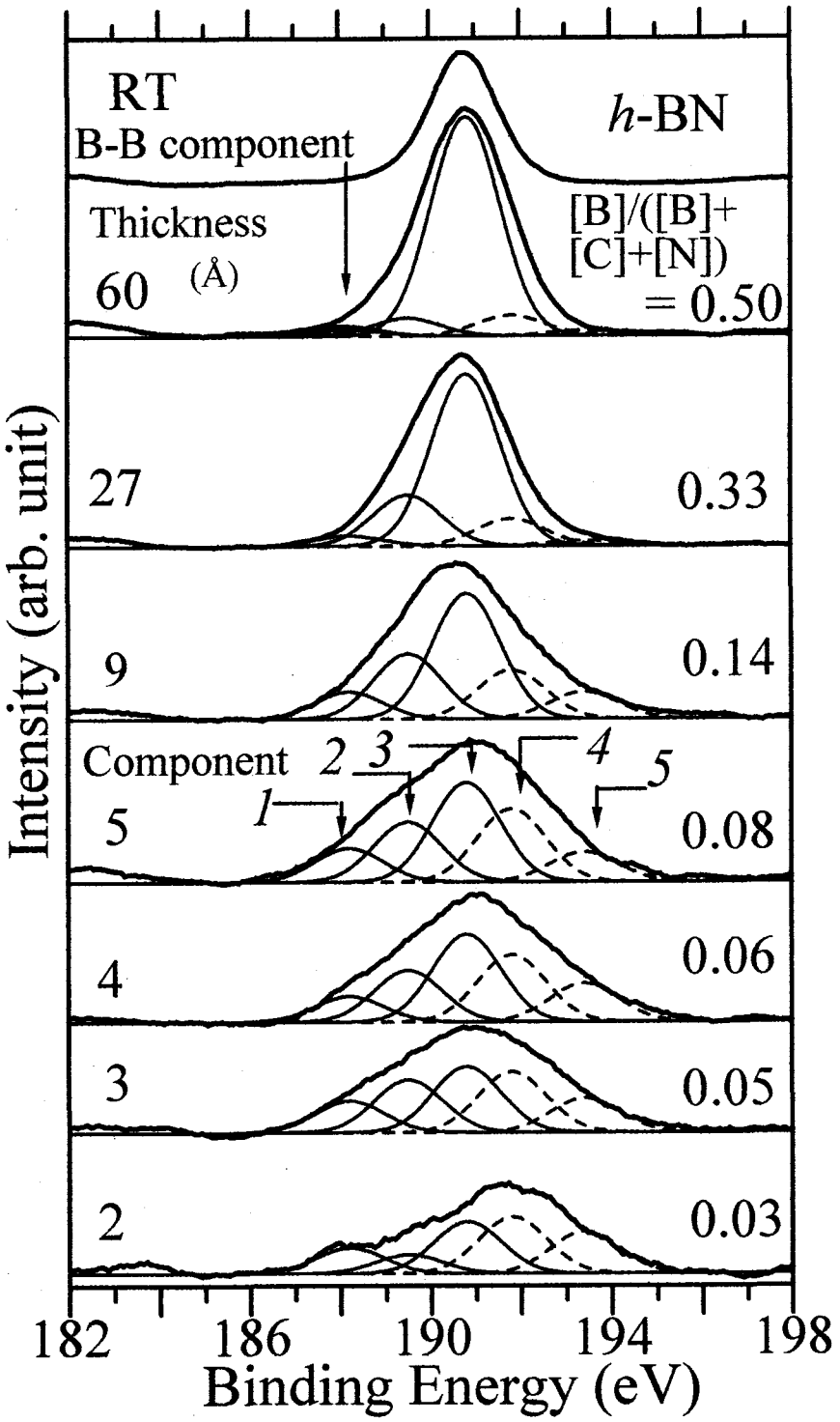

Fig. 23. Deconvoluted B(1s) XP spectra for B-C-N hybrid thin films. Curves in figure correspond to the results at RT. Thickness and [B] / ([B]+[C]+[N]) ratio are shown at the left and right sides of each spectrum, respectively. Top curve shows the spectrum for bulk *h*-BN.

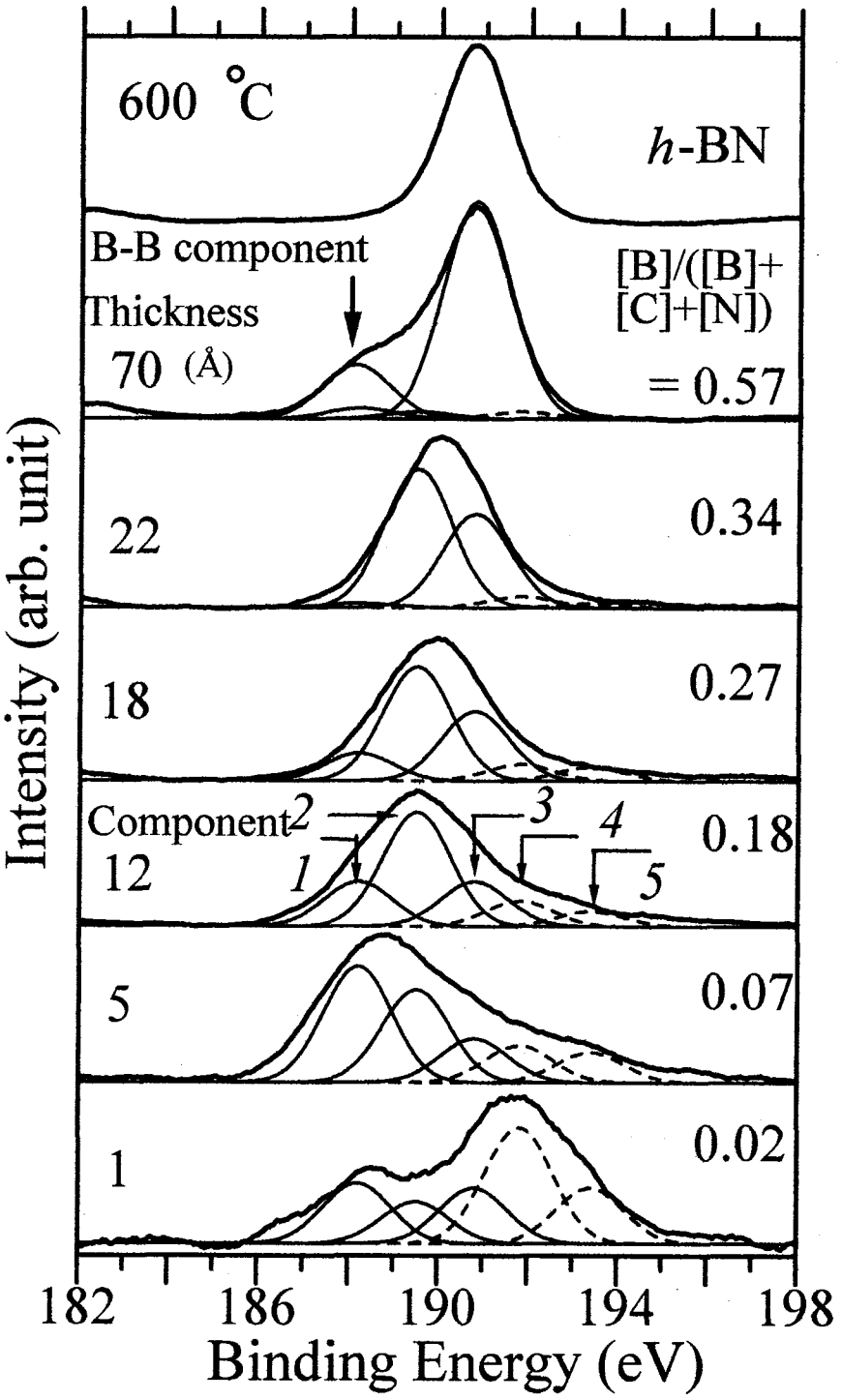

Fig. 24. Deconvoluted B(1s) XP spectra for B-C-N hybrid thin films. Curves in figure correspond to the results at 600 °C. Thickness and [B] / ([B]+[C]+[N]) ratio are shown at the left and right sides of each spectrum, respectively. Top curve shows the spectrum for bulk *h*-BN.

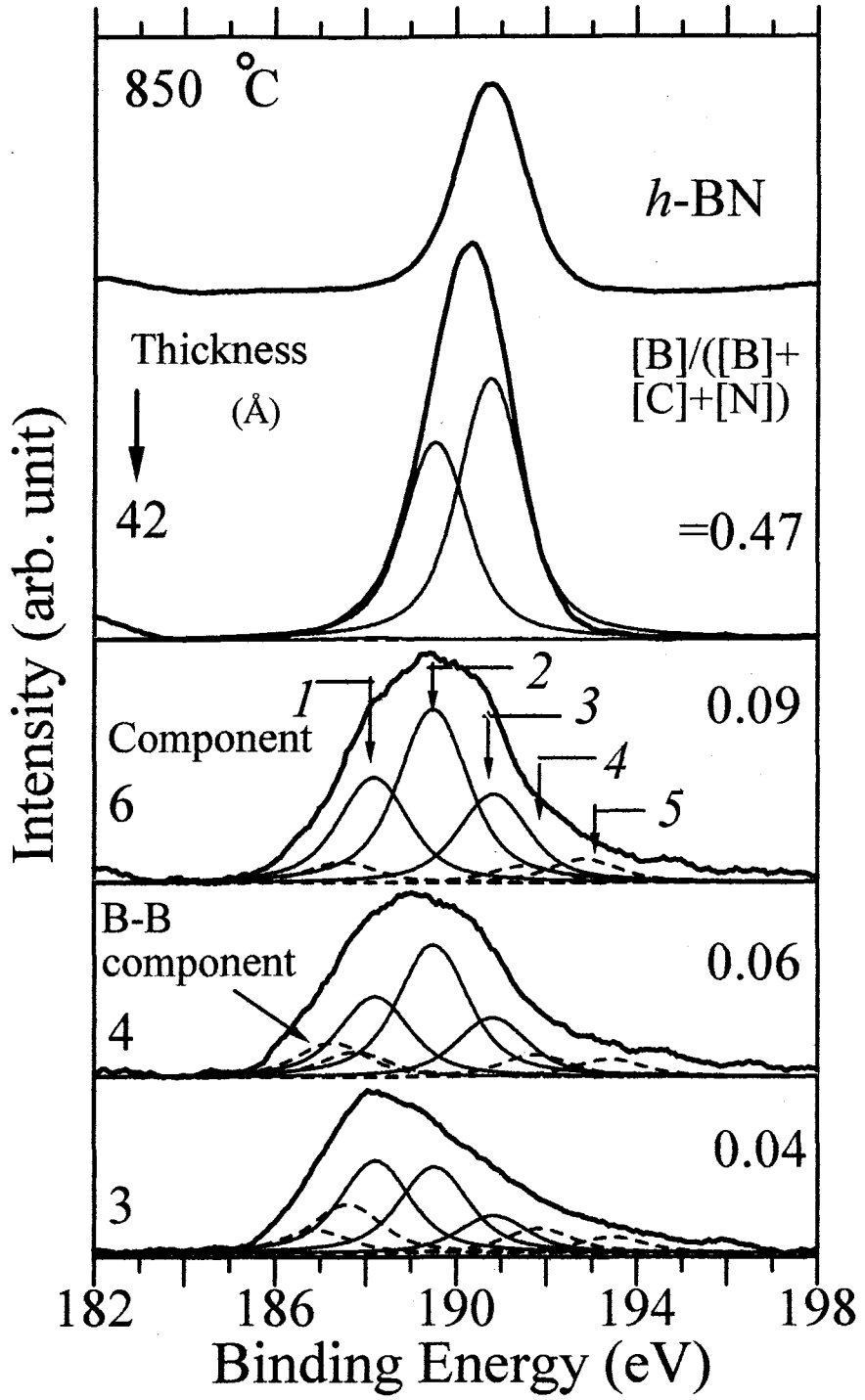

Fig. 25. Deconvoluted B(1s) XP spectra for B-C-N hybrid thin films. Curves in figure correspond to the results at 850 °C. Thickness and [B] / ([B]+[C]+[N]) ratio are shown at the left and right sides of each spectrum, respectively. Top curve shows the spectrum for bulk *h*-BN.

(i) Formation of h-BN

The [B] / ([B]+[C]+[N]) ratio and the corresponding thickness are shown on the right and left sides of each spectrum, respectively. The top curve of each figure shows the B(1s) spectrum of *h*-BN as a reference. Due to the space charge effect, the binding energy of B(1s) peak of bulk *h*-BN shifted to higher value. However, it has been already confirmed that stoichiometric BN film is predominantly formed when large amount of borazine plasma is deposited on HOPG previously [64]. Therefore, the B(1s) peak energy of bulk *h*-BN is calibrated to coincide with the peak energy of the sample which has the largest [B] / ([B]+[C]+[N]) ratio, supposing that BN film was finally formed on HOPG.

(ii) Various local structures of B

The full widths at half maximum (FWHM) of B(1s) peaks for the deposited films are larger than that of *h*-BN, which suggests that B atoms have various chemical conditions. Therefore, the peaks were deconvoluted. The measured B(1s) peak of *h*-BN, shown as the top curve of Figs. 23, 24, and 25, has the FWHM of ~1.8 eV. Using this FWHM, the number of Voigt functions for the peak deconvolution analysis were changed. Since five Voigt functions were needed at least to reproduce all the B(1s) XPS spectra, it is supposed that five components exist in the spectra. The Voigt functions are denoted by corresponding peak (component) numbers in the figure with arrows.

As candidates of the components, some possible atomic coordinations of B and N sites are summarized in Table 1, together with the corresponding binding energies and references [25,26,64-77].

Table 1

Possible atomic coordinations of B and N sites and corresponding binding energies reported and observed.

Atomic coordination of B and N	BB_3	BC_3	BCN_2	BC_2N	BN_3	NB_3	NB_2C	NBC_2	NC_3
Reported binding energy (eV)	187.3[74] 188.1[75] 187.9[65] 188[64]	~188[53] 188.4[65] 188.2[67]	188[22,23,71] 189.5[67]		191[69] 190.5[68] 189.8[71] 190.4[64] 190.2[65,76] 190.8[67]	398.3[69] 398[22,71] ~398[64] 398.7[66]	398.7[70] 399.3[22,23,71] 399.31[77]		~401[71] 400.3[2,70] 400[69]
Component		1	2		3				
Observed binding energy (eV)	188.1 187-187.8	188.2	189.5		190.8	~398.5	399.5		400.3

Among the components, the component 3 forms the dominant peak for thick films in Figs. 23 and 24. This peak is assigned to BN film deposited on HOPG. The reported values of B(1s) E_b^F of bulk *h*-BN slightly distribute in the range of 189.8-191 eV [64,65,68,71,73]. The peak energy (190.8 eV) of the component 3 is located in this range. This supports the above interpretation. This component is assigned to BN_3 coordination based on the atomic coordination of *h*-BN. Since the peak energy (188.2 eV) of the component 1 is close to the B(1s) E_b^F (188 eV and 188.4 eV) of BC_3 [64,65], this component is assigned to the BC_3 coordination. The chemical shift between the components 1 and 3 is about 2.6 eV, which is close to that of reported value for BN_3 and BC_3 coordinations [25].

(iii) B-C-N hybrid structure

In the strict sense, the chemical shift of XPS is governed by some factors, *i.e.*, interaction between core and valence electrons, Madelung potential, and relaxation energy accompanied by photoelectron emission [78]. However, the order of B(1s) E_b^F for BN_3 and BC_3 coordinations is approximately explained by the electronegativity differences between C and N. Since C atom has smaller electronegativity than N atom, the B atom with BN_3 coordination is more positively charged than that with BC_3 coordination. Consequently, the B(1s) E_b^F for BN_3 is higher than that for BC_3.

Based on this idea, it is considered that the B(1s) E_b^F for possible B-C-N hybrid coordination, *e.g.*, BCN_2 and BC_2N coordinations, should be located between those of BN_3 and BC_3. Therefore, the component 2 (E_b^F = 189.5 eV) would be assigned to B-C-N hybrid. The reported B(1s) E_b^F value of the B-C-N hybrid ranges from 188 eV to 191 eV [25,26,67,71]. This distribution may originate from the variations of the coordination in the B-C-N hybrid.

The B-C-N hybrid component (component 2) is always observed for the spectra in Figs. 23-25. However, the relative intensity of the component 2 to the other components considerably depends on the fluence and temperature. For the sample prepared at RT (Fig. 23), the B-C-N hybrid component is always smaller than the BN_3 component (component 3) and disappears with high fluence (thickness). This means that BN is preferentially formed at RT though B-C-N hybrid is synthesized at the interface between HOPG substrate and BN overlayer. On the other hand, the B-C-N hybrid component becomes dominant at the [B] / ([B]+[C]+[N]) ratio ranging from 0.18 to 0.34 for the sample prepared at 600 °C (Fig. 24). This enhancement of B-C-N hybrid formation is also observed at the [B] / ([B]+[C]+[N]) ratio ranging from 0.04 to 0.09 for the sample prepared at 850 °C (Fig. 25). These results clearly show that B-C-N hybrid is preferentially formed above 600 °C. Furthermore, the relative peak intensity of the B-C-N hybrid component in Fig. 25 shows higher value than that in Fig. 24 at very low fluence region. This implies that 850 °C could be more preferable to synthesize B-C-N hybrid than 600 °C.

(iv) BC_3 structures

The intensity of the BC_3 component (component 1) is also enhanced at high temperature and low [B] / ([B]+[C]+[N]) region. Graphite-like BC_3 among the family of B-C-N ternary materials has been proposed by Kouvetakis *et al.* [79]. According to a theoretical approach [80], BC_3 would have semiconducting or metallic property depending on the monolayer or bulk structure. Since the electronic conductivity of bulk BC_3 is expected to be larger than that of graphite, this material is interesting as a two-dimensional metallic material [79]. Thus, the fact that BC_3 component was preferentially formed by high temperature ion implantation is very interesting as well as preferential B-C-N hybrid formation.

(v) B-B structures

An additional component appears at ~188.1 eV for the thickest sample in Fig. 24. This is not assigned to BC_3 component because HOPG was covered by thick BN layer. This component may originate from B-B bonds with variety of coordinations, *e.g.*, BB_2N and BBN_2 [64,65,78,81]. On the other hand, this component is negligible in Figs. 23 and 25. This component grows when thick BN film is deposited on HOPG. The thickness of the BN film with B-B component is 70 Å (Fig. 24), and those

prepared without B-B component are 60 and 42 Å (Figs. 23 and 25), respectively. Same component has been observed for the sample with thickness of 84 Å [64]. Therefore, it is thought that some threshold thickness for the formation of the B-B bonds may exist between 60 and 70 Å.

Other components appear around 187-187.8 eV for the low [B] / ([B]+[C]+[N]) samples prepared at 850 °C in Fig. 25. These components do not appear for the samples prepared at RT and 600 °C. Since the peak energies of the components are close to the B(1s) E_b^F value of the B-B components, these components might be assigned to B-B bonds. The reason why B-B components appear even for thin film may be the increase of diffusion coefficient. It is generally accepted that the diffusion coefficient increases at high temperature. Therefore, implanted boron can migrate long distance in HOPG to form B-B component in graphite at quite high temperature. However, due to the featureless structure of B(1s) XP spectra, it is difficult to further discuss such ambiguous components.

(vi) Other structures

Furthermore, the assignment of two other components centered at 191.8 eV (component 4) and 193.4 eV (component 5) is also unknown. Although the B(1s) E_b^F for B-O bond should have higher binding energy [82] than that of BN_3, the high binding energy peaks (components 4 and 5) can not be assigned to B-O bond because I have not found any oxygen peak in XP wide scan spectra. These peaks may originate from different B-C-N clusters [1] or nanotubes like BC_2N or BC_3 nanotubes [82]. Further investigations are needed to assign these peaks properly.

(vii) Temperature and fluence effects

In order to evaluate the temperature and fluence effects clearly, the deconvoluted peak intensities of Figs. 23-25 versus [B]/([B]+[C]+[N]) ratios are plotted in Fig. 26 for RT, Fig. 27 for 600 °C and Fig. 28 for 850 °C.

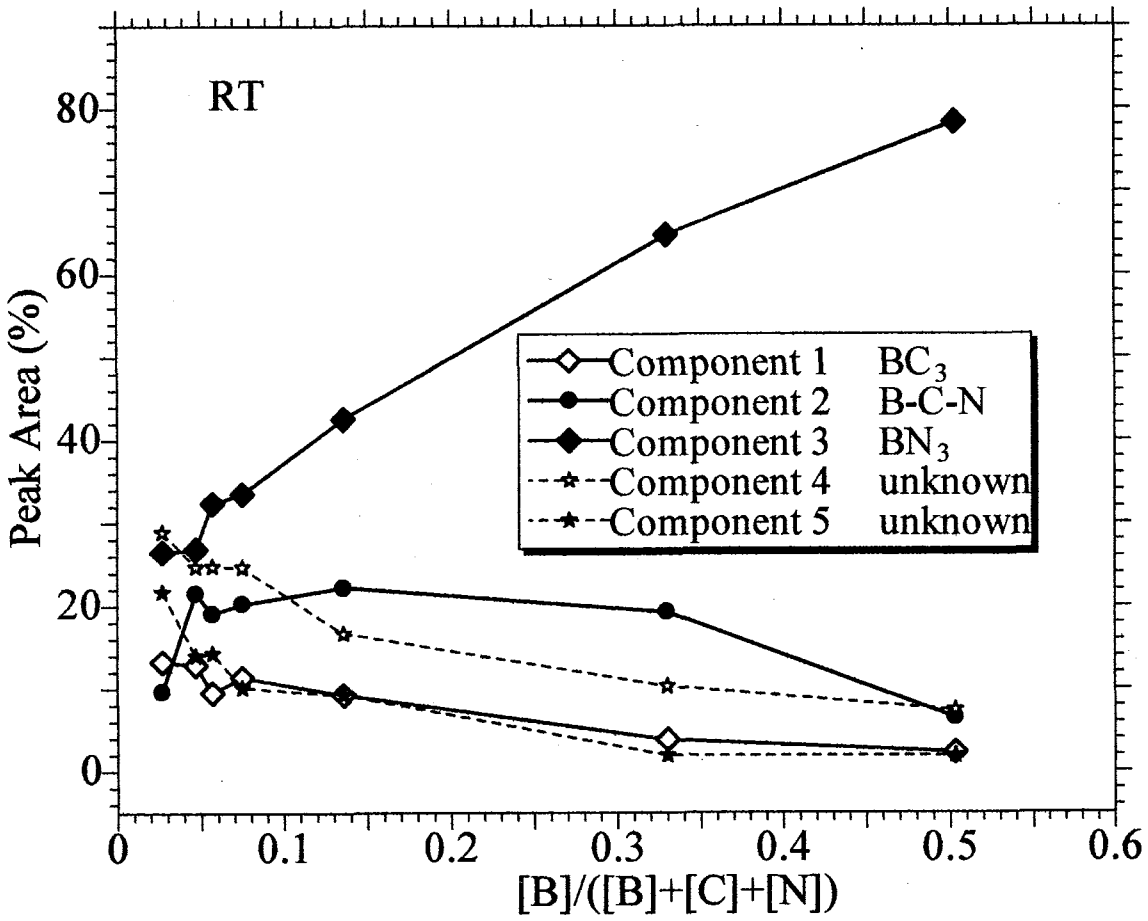

Fig. 26. The intensities of the deconvoluted five components in Fig. 23 as a function of the surface [B]/([B]+[C]+[N]) ratio. Figure corresponds to the results at room temperature. Corresponding peak (component) assignments are shown in boxes.

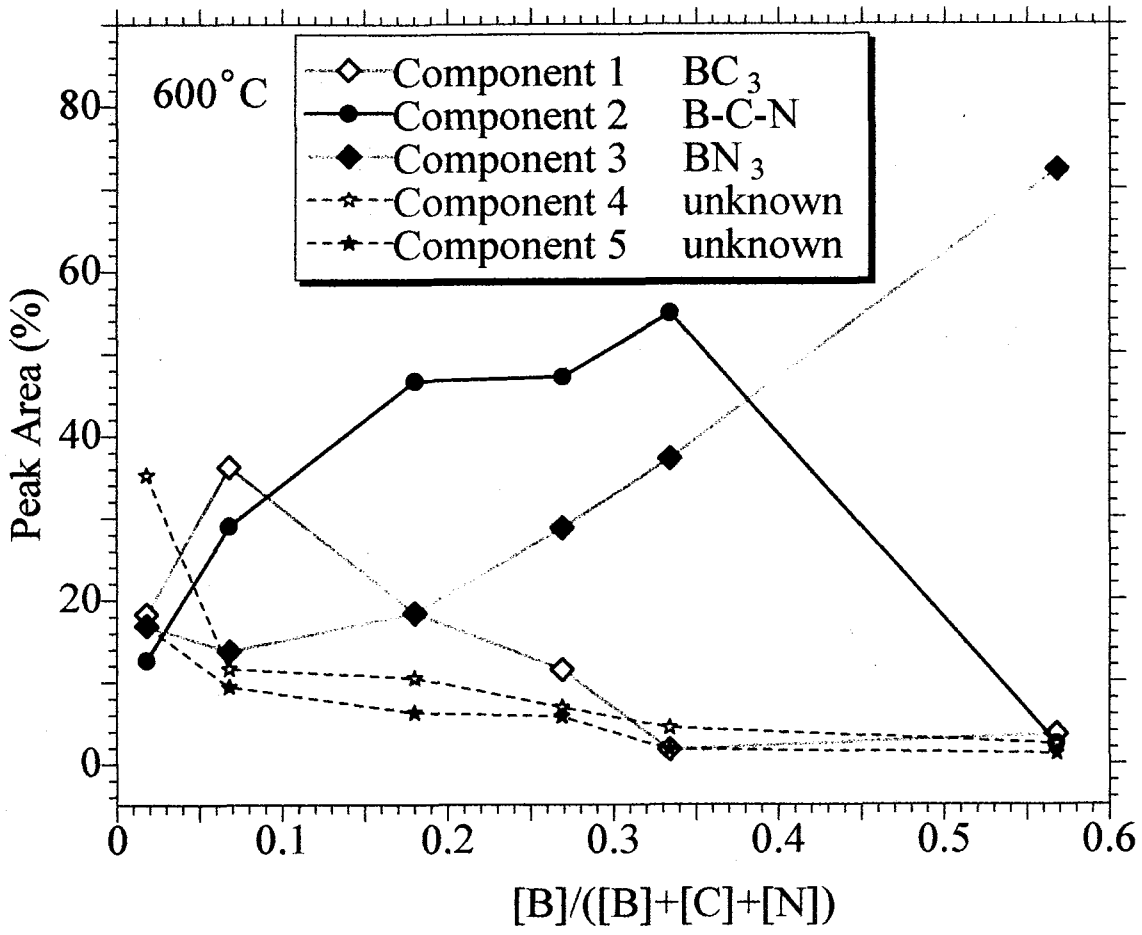

Fig. 27. The intensities of the deconvoluted five components in Fig. 24 as a function of the surface [B]/([B]+[C]+[N]) ratio. Figure corresponds to the results at 600 °C. Corresponding peak (component) assignments are shown in boxes.

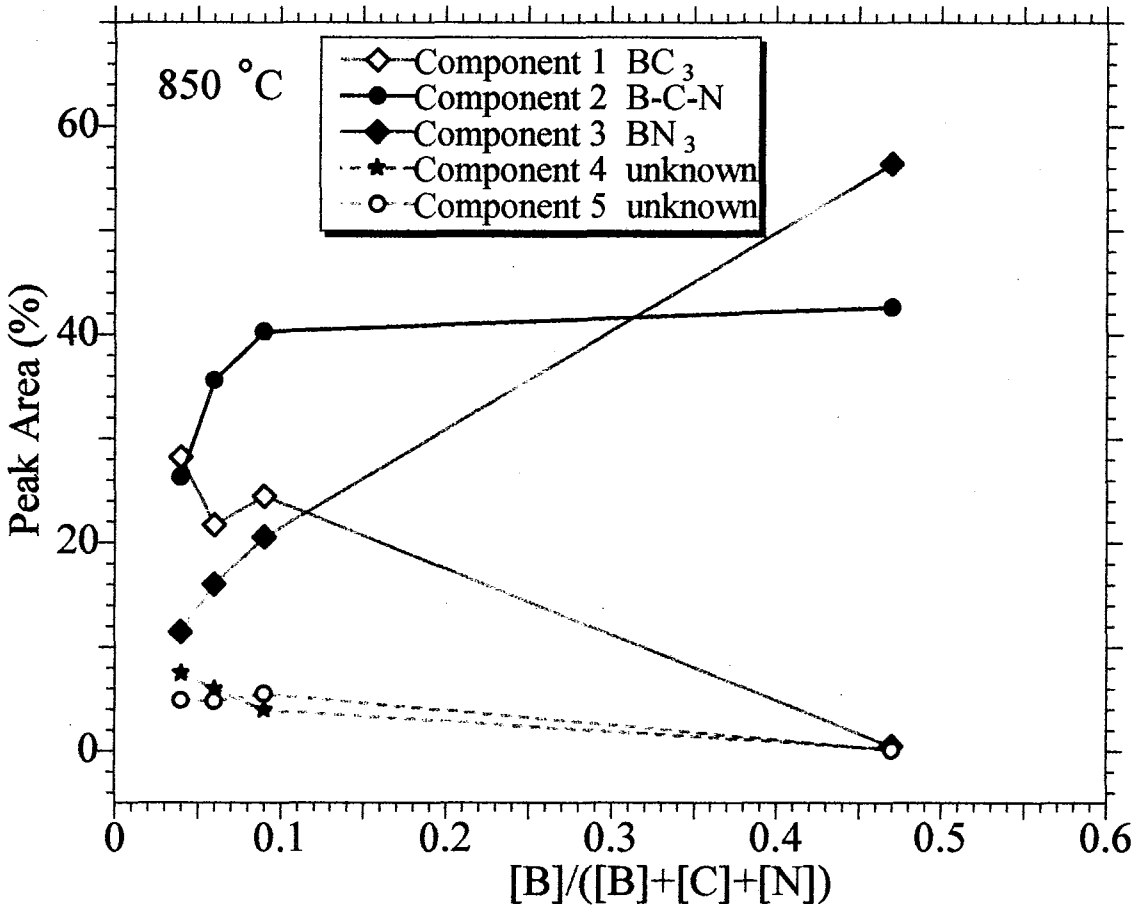

Fig. 28. The intensities of the deconvoluted five components in Fig. 25 as a function of the surface [B]/([B]+[C]+[N]) ratio. Figure corresponds to the results at 850°C. Corresponding peak (component) assignments are shown in boxes.

It is seen that the B-C-N hybrid component (component 2) increases from the [B]/([B]+[C]+[N]) ratio of 0.02 to 0.34 at 600 °C (Fig. 27), whereas the B-C-N hybrid remains almost constant from 0.04 to 0.33 at RT. Fig. 27 shows that the B-C-N hybrid dominates over the others at 600 °C in the [B]/([B]+[C]+[N]) ratio ranges from 0.1 to 0.35. On the other hand, Fig. 28 shows that B-C-N hybrid is very high, compared to others and those of 600 °C at low fluence. On the basis of the results, it is elucidated that the borazine plasma implantation on graphite at high temperature and low fluence is effective method to synthesize thin films of B-C-N hybrid. The results open up a possibility that the composition of B-C-N hybrid films can be controlled by changing the temperature and fluence during the ion implantation.

The intensity of the BC_3 component is enhanced at high temperature in low [B]/([B]+[C]+[N]) ratio region of about 0.02 to 0.3, shown in Figs. 26-28. The high content of BC_3 component over BN_3 component at low fluence means that the C atoms from graphite substrate are bonded to B atoms at the interface between graphite and BN film, and the formation of these chemical bonds are enhanced at high temperature.

BN_3 component dominates over all components in all [B]/([B]+[C]+[N]) ratios at RT. The content of this component decreased in low [B]/([B]+[C]+[N]) ratio at high temperature. This implies that BN_3 component is preferentially formed by RT ion implantation and in high [B]/([B]+[C]+[N]) ratio at high temperature.

3.3.3.2 Local structures of N site

The N(1s) XP spectra at RT, 600 °C, and 850 °C are shown in Figs. 29-31, respectively.

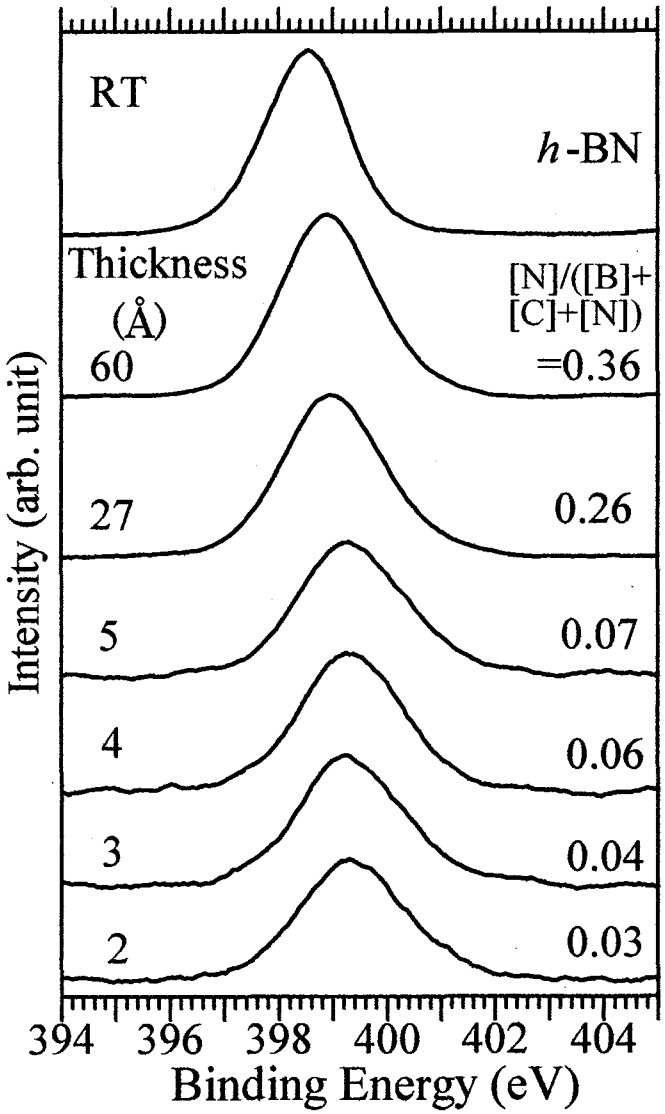

Fig. 29. N(1s) XP spectra of B-C-N hybrid thin films. Curves in figure correspond to the results at RT. Thickness and [N] / ([B]+[C]+[N]) ratio are shown at the left and right sides of each spectrum, respectively. Top curve shows the spectrum for bulk *h*-BN.

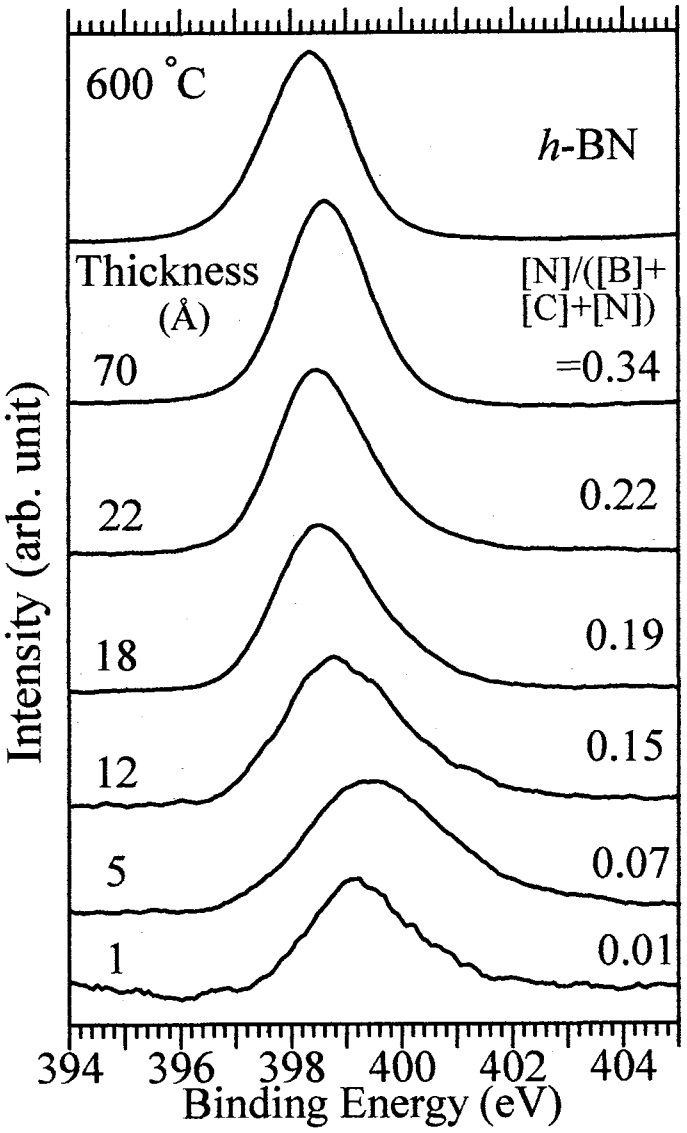

Fig. 30. N(1s) XP spectra of B-C-N hybrid thin films. Curves in figure correspond to the results at 600 °C. Thickness and [N] / ([B]+[C]+[N]) ratio are shown at the left and right sides of each spectrum, respectively. Top curve shows the spectrum for bulk *h*-BN.

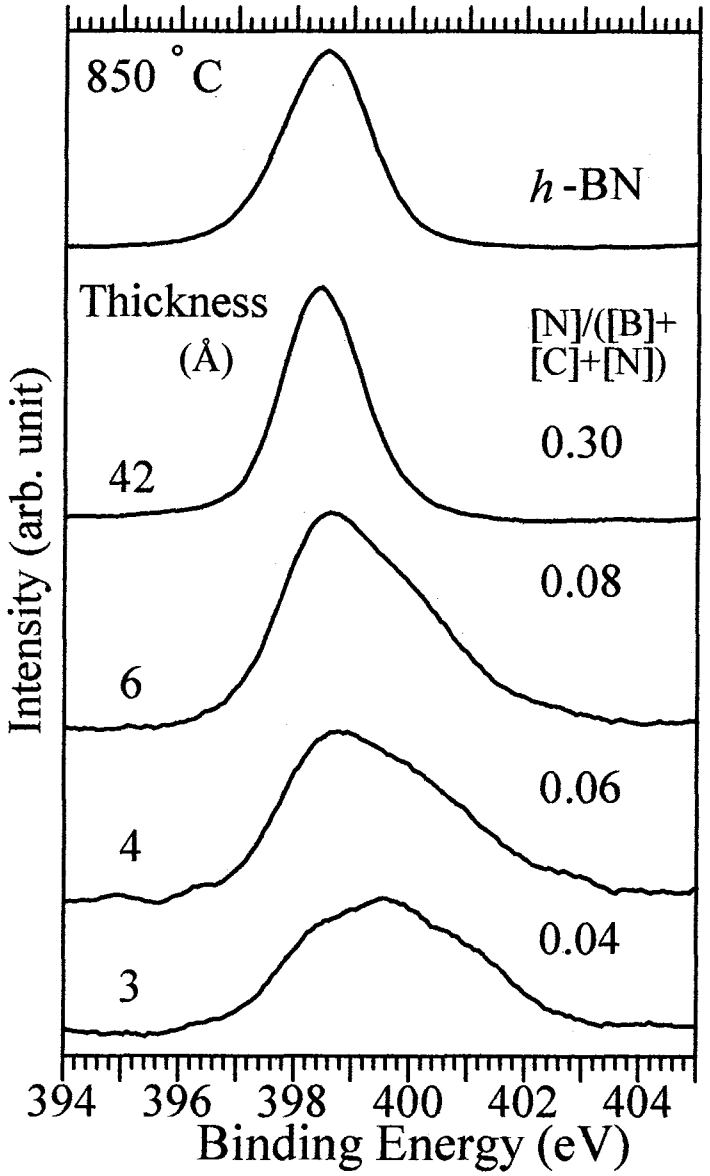

Fig. 31. N(1s) XP spectra of B-C-N hybrid thin films. Curves in figure correspond to the results at 850 °C. Thickness and [N] / ([B]+[C]+[N]) ratio are shown at the left and right sides of each spectrum, respectively. Top curve shows the spectrum for bulk *h*-BN.

Each spectrum shows the result for the film which has different composition. The [N] / ([B]+[C]+[N]) ratio and the corresponding thickness are shown on the right and left sides of each spectrum, respectively. The top curve of each figure shows the N(1s) spectrum of *h*-BN. The range of N(1s) E_b^F for N atoms bonded to B and C is relatively small [20,81] and then information of the bonding states from N(1s) spectra is more ambiguous than the case of B(1s) spectra. Therefore, the peak deconvolution for N(1s) spectra are not performed.

The peak widths at low [N] / ([B]+[C]+[N]) ratios are clearly broader than that for *h*-BN. This result indicates that the N(1s) peaks consist of various kinds of components. As shown in Table 1, it has been reported that the N(1s) E_b^F of NB_3 component distributes in the range of 398.0-398.7 eV [25,64,66,69,71,76]. The N(1s) E_b^F of NC_3 component has been reported to be around 400-401 eV [2,68,69,73]. Thus, it is considered that the N(1s) E_b^F of B-C-N hybrid should be located between those binding energies. Since the peak energy of the N(1s) spectra shifts from around 399-400 eV to lower energy side and approaches to bulk *h*-BN peak, it is deduced that B-C-N hybrid is formed at low fluence for all the temperatures. This confirms the formation of B-C-N hybrid at N site. The reported E_b^F of B-C-N hybrid is located in the range of 398.7-399.3 eV [25,26,71,72] which also supports the above interpretation.

As shown in the Figs. 29-31, clear fluence (thickness) effect was observed on the synthesis of B-C-N hybrid. B-C-N hybrid was formed preferentially as the fluence was small. Namely, B-C-N hybrid was formed at the interface between HOPG target and BN overlayer. However, the temperature effect was not so clear as the case of B(1s) spectra. RT spectra (Fig. 29) show B-C-N hybrid deposition even at the low fluence. It apparently looks controversial to the interpretation of B(1s) spectra. In order to explain this ambiguity, we propose two explanations. One is a structural model, shown in Fig. 32, is proposed.

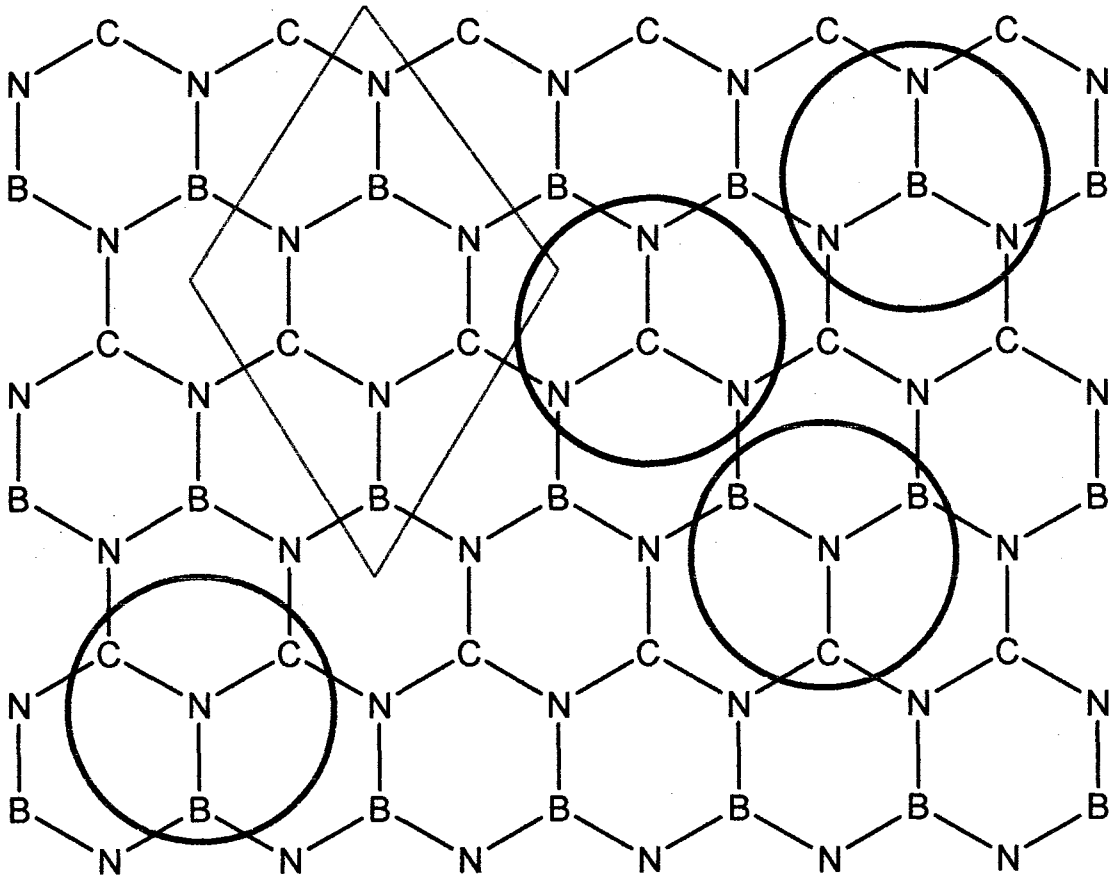

Fig. 32. Structural model for B-C-N hybrids formed at RT.

The rhombus indicates the unit cell of B-C-N hybrids. B and C have the coordinations; BN_3 and CN_3, respectively, whereas N has two types of coordinations; BNC_2 and B_2NC. This suggests that BN_3 component is high at RT as shown in B(1s) XP spectra (Fig. 23). However, B-C-N hybrid component with the coordinations of BNC_2 and B_2NC also exists in N(1s) spectra as shown in Fig. 29 for RT. The apparent inconsistency between B(1s) and N(1s) spectra can be caused by this unique structure because this implies that the B-C-N hybrid at N site is different from that at B site. The problem of this idea is discrepancy on the composition of the films. For all samples, the boron contents are close or larger than corresponding nitrogen contents. However, this model has BCN_2 stoichiometry and nitrogen content should be larger than boron content when this structure is predominantly formed. Another explanation is an idea that various kinds of structures were simultaneously formed in the films. In this model, the local structure formed at N sites can be different from that at B sites and N(1s) XPS spectra show characteristic behavior which is different from the B(1s) XPS spectra depending on the stability of each structure. In fact, N(1s) spectra become broader especially at low

fluence as the temperature increases. This indicates that various kinds of B-C-N hybrids were preferentially formed at N sites in high temperature at low fluence.

3.3.3.3 Local structures of C site

The C(1s) XP spectra at RT, 600 °C, and 850 °C are shown in Figs. 33-35, respectively. Each spectrum shows the result for the film which has different composition. The [C]/([B]+[C]+[N]) ratio and the corresponding thickness are shown on the right and left sides of each spectrum, respectively. The bottom curve of each figure shows the C(1s) spectrum of HOPG.

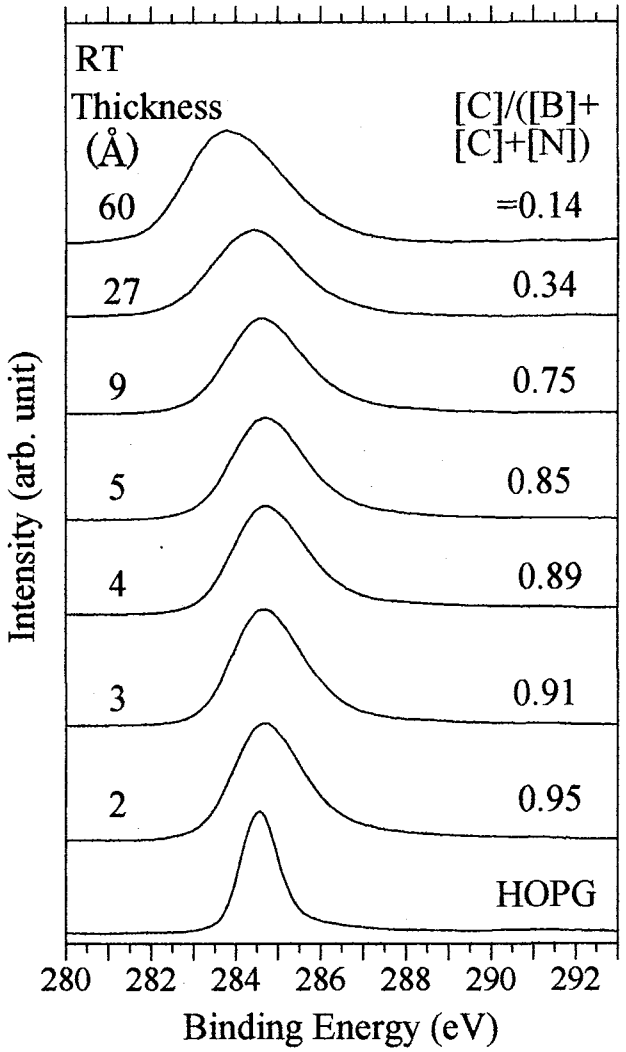

Fig. 33. C(1s) XP spectra of B-C-N hybrid thin films. Curves in figure correspond to the results at RT. Thickness and [C]/([B]+[C]+[N]) ratio are shown at the left and right sides of each spectrum, respectively. Bottom curve shows the spectrum for HOPG.

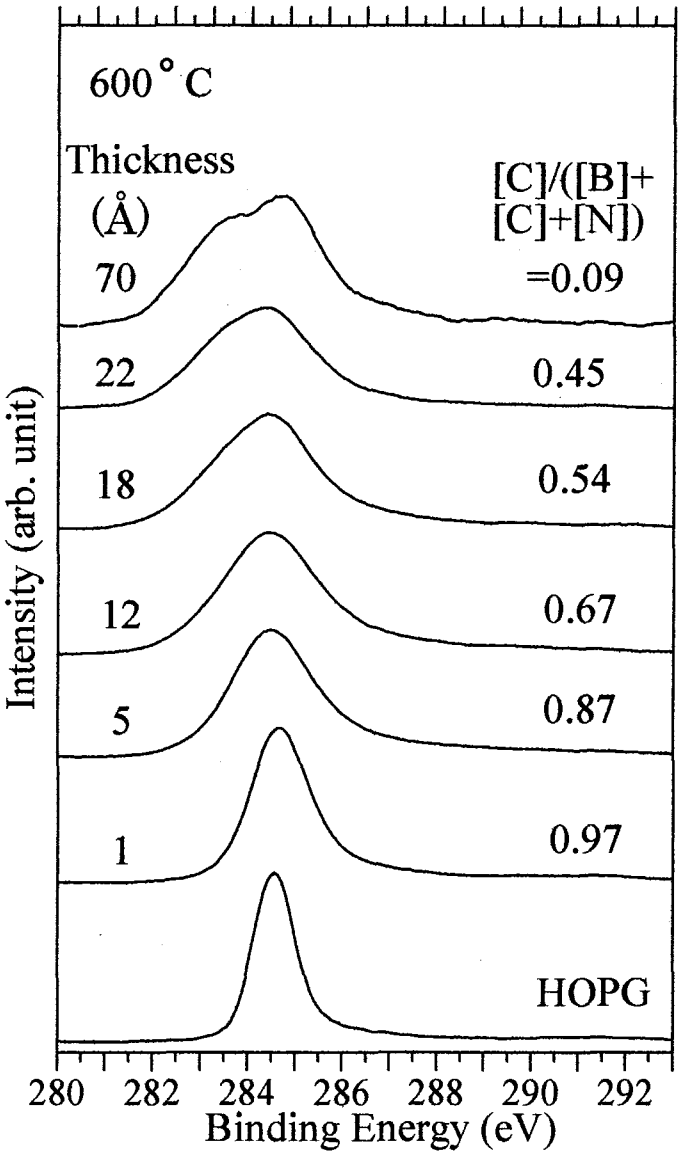

Fig. 34. C(1s) XP spectra of B-C-N hybrid thin films. Curves in figure correspond to the results at 600 °C. Thickness and [C]/([B]+[C]+[N]) ratio are shown at the left and right sides of each spectrum, respectively. Bottom curve shows the spectrum for HOPG.

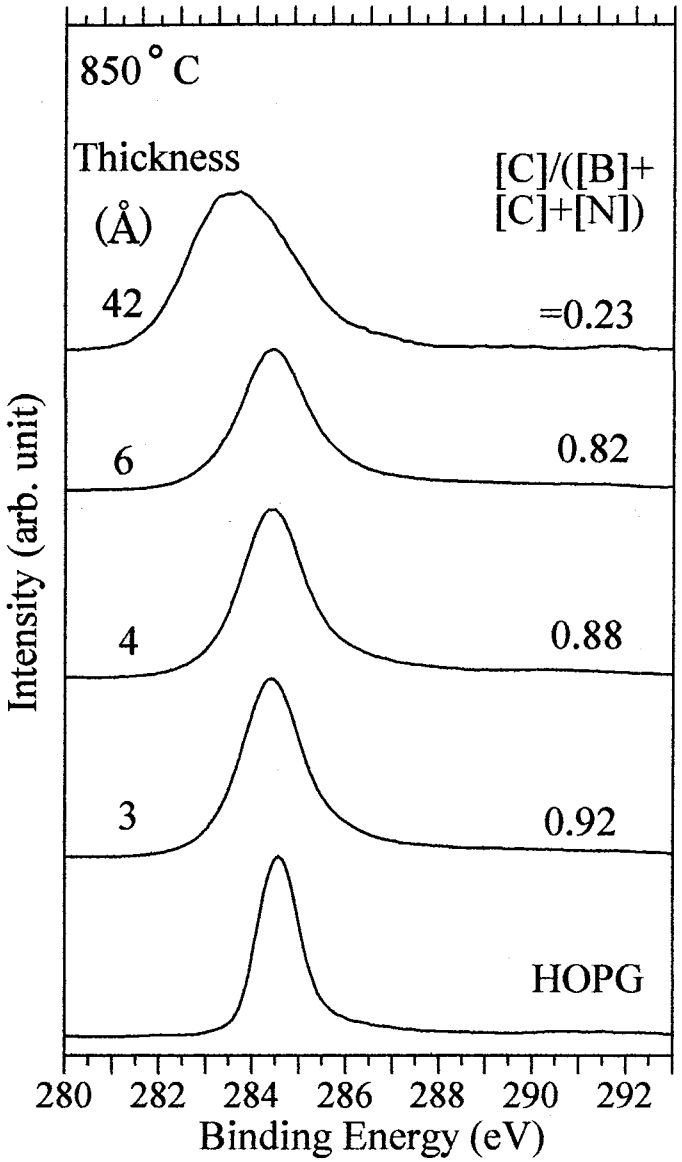

Fig. 35. C(1s) XP spectra of B-C-N hybrid thin films. Curves in figure correspond to the results at 850 °C. Thickness and [C]/([B]+[C]+[N]) ratio are shown at the left and right sides of each spectrum, respectively. Bottom curve shows the spectrum for HOPG.

The spectrum of C(1s) has peak energy of 284.6 eV for HOPG as shown in Figs. 33-35. This is assigned to C-C bond. The broadening of the spectrum with the film thickness is observed. This indicates the formation of other chemical bonds. The formation of C-B and C-N bonds may be shown as the broadened components. The C(1s) peak also shows large shift to lower binding energy side with increase of film thickness. This means that this shift is not caused by space charge effect. Shimoyama et al. [ref] proposed that this shift is caused by band bending effect because hetero junction would be

formed between B-C-N layer and BN overlayer. Due to this shift, the interpretation of C(1s) peak is difficult and peak deconvolution for C(1s) spectra are not performed.

An Mg Kα x-ray source (hν=1253.6 eV) was used for XPS measurement. The energy is fairy high compared with vacuum ultraviolet (VUV) light from synchrotron radiation described in the next section. So the kinetic energies of photoelectrons excited by Mg Kα x-ray is higher than those excited by VUV. Therefore the present XPS using Mg Kα x-ray is more bulk sensitive than that using VUV (see Fig.14). Therefore, most of the C(1s) signals came from HOPG for low film thickness. The C(1s) signals from interfacial B-C-N layer gradually increase as the BN over layer grows on HOPG target. That is why the large peak broadening is observed at high thickness. Furthermore, the large peak broadening is prominent at high temperature. Comparing the peak width of the films which has similar thickness, Fig. 34 shows larger peak width than that in Fig. 33. This implies that different types of bonds (e.g. B-C and C-N) are preferentially formed at high temperatures. This result supports the earlier interpretation of B(1s) and N(1s) spectra. However, the temperature effect is not so clear as the case of B(1s) spectra. In order to get clear information from C(1s) spectra some different calculations, like molecular orbital calculation, are needed.

3.3.4 Conclusions

Borazine ion plasma was implanted on HOPG at RT, 600 °C, and 850 °C in order to synthesize B-C-N hybrid thin films. XPS study suggested that B, N and C atoms in the deposited films are in a wide variety of atomic coordinations. The deconvolution of B(1s) spectra suggested the formation of BC_3, B-C-N hybrid, and BN_3. B-C-N hybrid component became dominant at low fluence at 600 °C and 850 °C although it was less than BN_3 component at RT. It is concluded that formation of B-C-N hybrid component is enhanced at high temperature borazine ion implantation on graphite. The results imply that it is possible to control the composition of B-C-N hybrid by changing the fluence of the ion plasma and the temperature of graphite during ion implantation. The N(1s) and C(1s) spectra showed clear fluence dependence on the synthesis of B-C-N hybrid. However, these spectra did not show clear temperature effect on synthesis of B-C-N hybrid. This implies that the B-C-N hybrid structure at B site is different from that at N site.

3.4 B-C-N hybrids prepared in BL11A UHV chamber

3.4.1 Work function of the spectrometer of BL11A system

Au($4f_{7/2}$) peak of which binding energy is 84.0 eV was used for the measurement on the work function of the spectrometer. Fig. 36 shows the XP spectrum of Au, using x-ray source of 401.55 eV from SR.

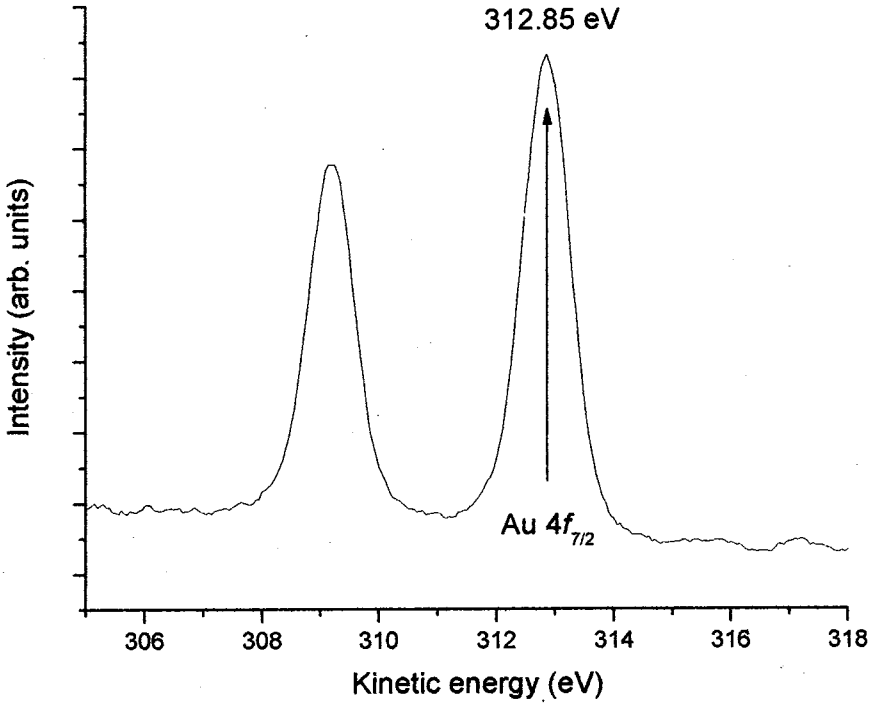

Fig. 36. XP spectrum of Au using x-ray source from SR ($h\nu$= 401.55 eV).

It shows the peak at 312.85 eV which correspond to Au($4f_{7/2}$). Work function of the spectrometer is calculated to be 4.7 eV. This value is used for the calculation of binding energy in XP spectra.

3.4.2 Composition, thickness, and local structures of B-C-N hybrids

In this case, SR x-ray source in the range of 300-700 eV was used for XPS measurements. The wide scan XP spectra of the films deposited at RT and 800 °C are shown in Fig. 37 (a) and Fig. 37 (b), respectively.

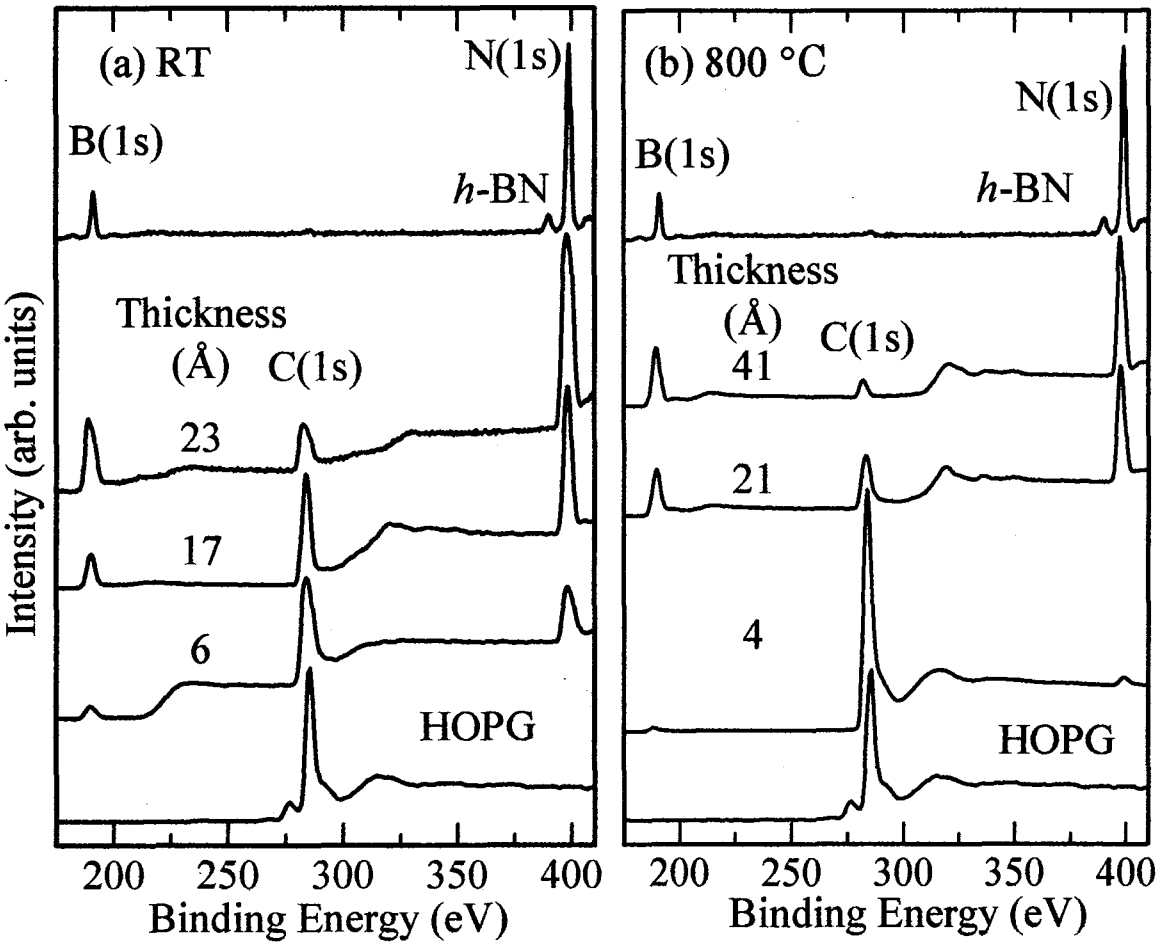

Fig. 37. XP wide scan spectra of B-C-N hybrid thin films at (a) RT and (b) 800 °C. Thickness is shown for each spectrum. Top and bottom curves show XP wide scan spectra of *h*-BN and HOPG, respectively.

These spectra indicate that the films are composed of B, C and N. No oxygen contamination was confirmed. XP spectra of *h*-BN and HOPG are also shown for comparison. The film thickness that obtained from the peak intensity, photo-ionization cross section and inelastic mean free path of photoelectron [83] is also shown in these figures. The intensity of the C(1s) peak decreases while B(1s) and N(1s) peaks grow with the increase in the film thickness. The [B] / [N] ratio of the films synthesized at the highest fluence is close to that of bulk *h*-BN. This indicates that the nearly stoichiometric BN layer was finally formed as borazine ion plasma was implanted on HOPG surface.

The B(1s) XP spectra of the films deposited at 800 °C with different thicknesses are shown in Fig. 38. The B(1s) spectrum of *h*-BN is also shown as a reference.

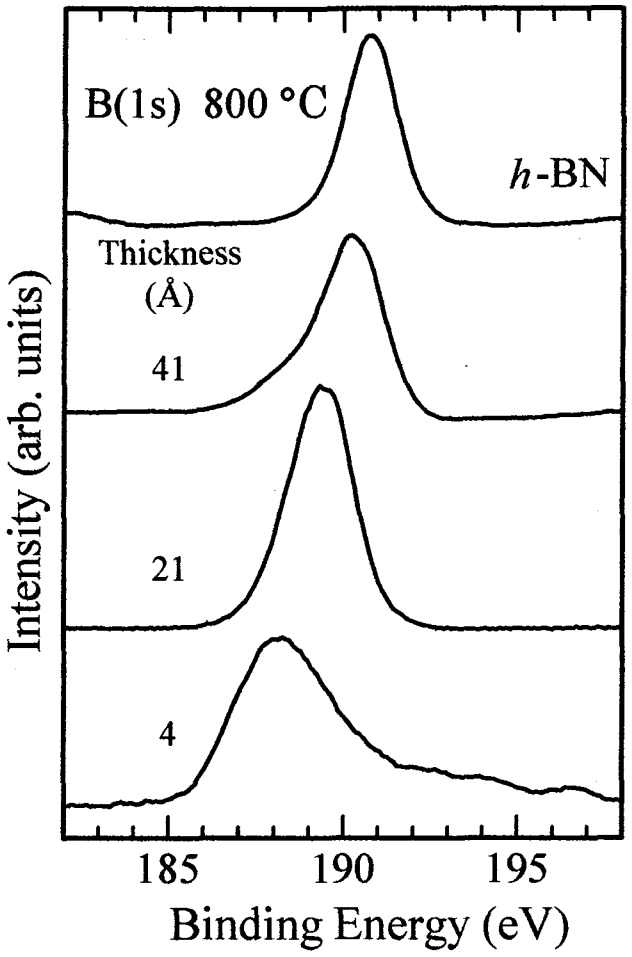

Fig. 38. B(1s) XP spectra for B-C-N hybrid thin films at 800 °C. Thickness is shown for each spectrum. Top curve shows the spectrum for bulk *h*-BN.

The full widths at half maximum (FWHM) of B(1s) peaks for the deposited films are larger than that of *h*-BN. It suggests that B atoms have various chemical environments. The B(1s) peaks with the binding energies of 188.2, 189.5, and 190.8 eV are previously assigned to BC_3, B-C-N hybrid, and BN_3 components, respectively [84]. Considering these assignments, Fig. 38 shows that BC_3, B-C-N hybrid, and BN_3 components have been formed in the films. It also shows that the contribution of BC_3 and B-C-N hybrid components is high at low fluence of borazine while that of BN_3 component is high at high fluence of borazine.

3.4.3 Geometrical and electronic structures of B-C-N hybrids

3.4.3.1 Orientation of B-C-N hybrids prepared at RT

B K-edge NEXAFS spectra for B-C-N hybrid films synthesized at RT are shown in Figs. 39-41 for the film thicknesses of 0.6 nm, 1.7 nm, and 2.3 nm, respectively. For comparison, NEXAFS spectrum for bulk *h*-BN is shown in the top of each figure.

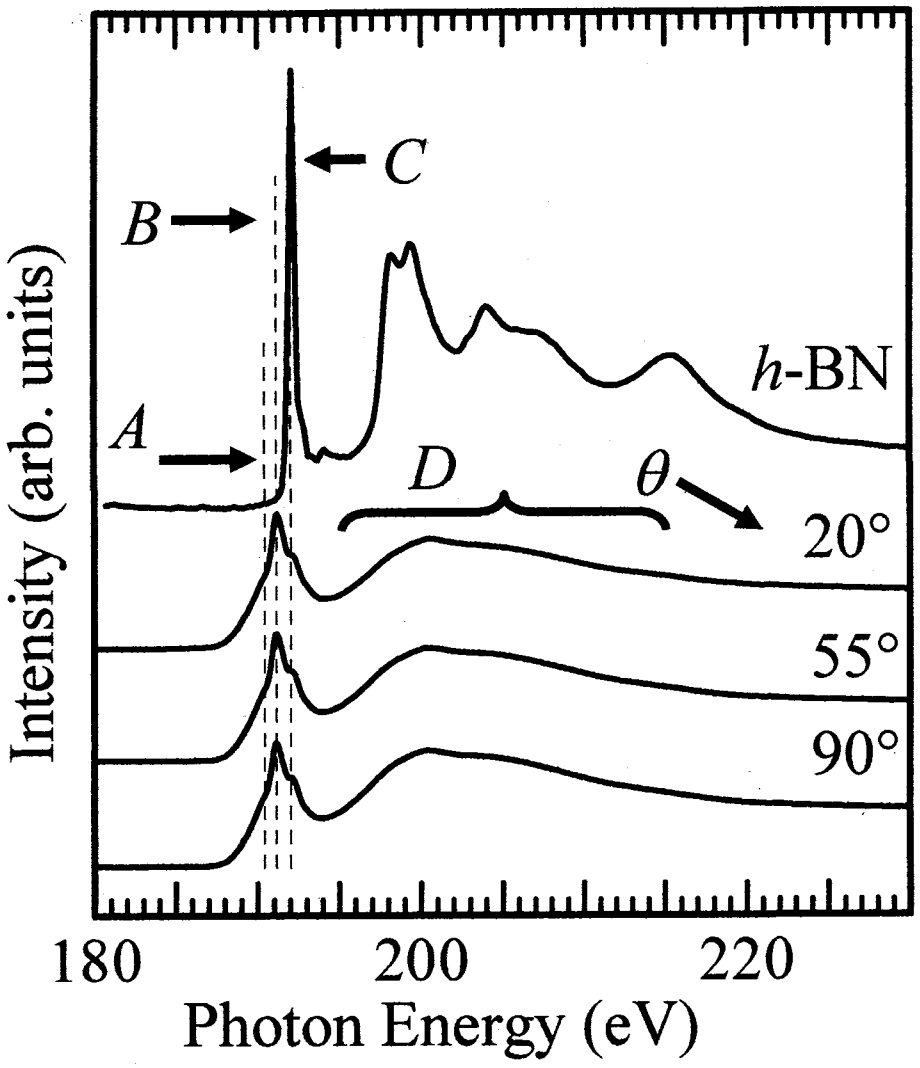

Fig. 39. B K-edge NEXAFS spectra for various incidence angles (θ) of x-ray of B-C-N hybrid films with the thickness of 0.6 nm synthesized at RT. NEXAFS spectrum for bulk *h*-BN is shown in the top of the figure.

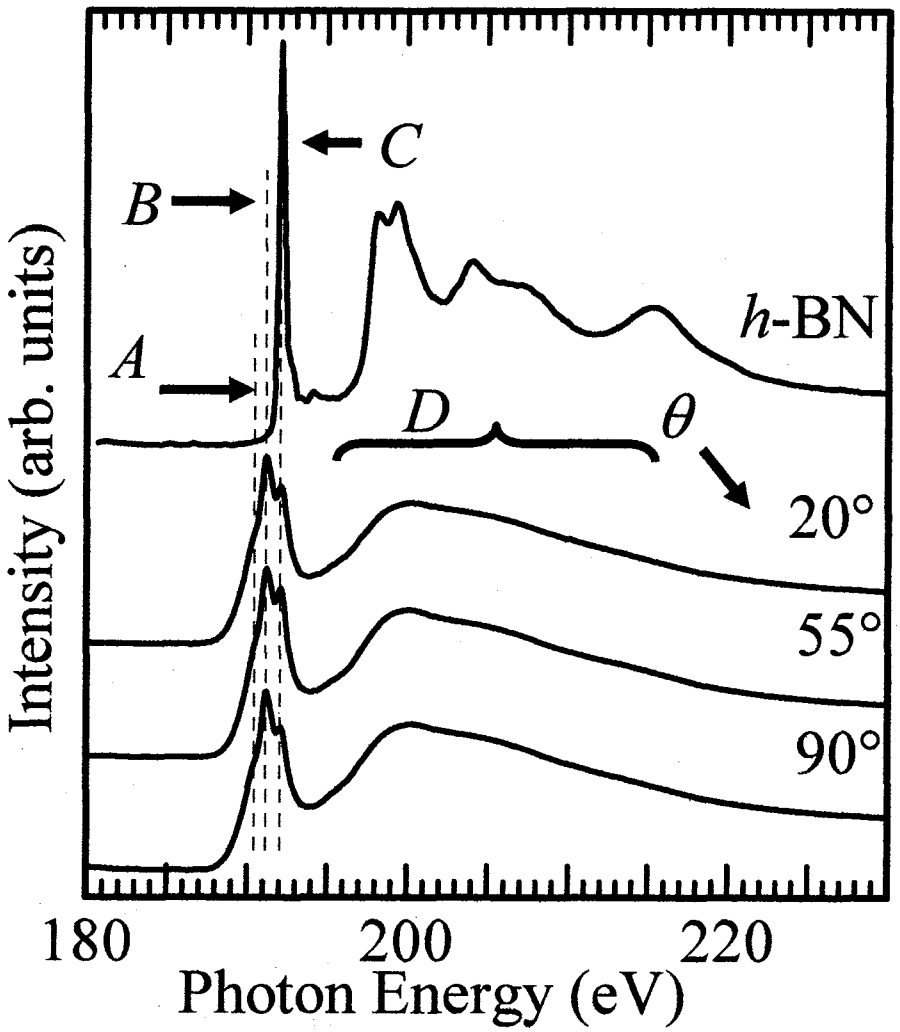

Fig. 40. B K-edge NEXAFS spectra for various incidence angles (θ) of x-ray of B-C-N hybrid films with the thickness of 1.7 nm synthesized at RT. NEXAFS spectrum for bulk *h*-BN is shown in the top of the figure.

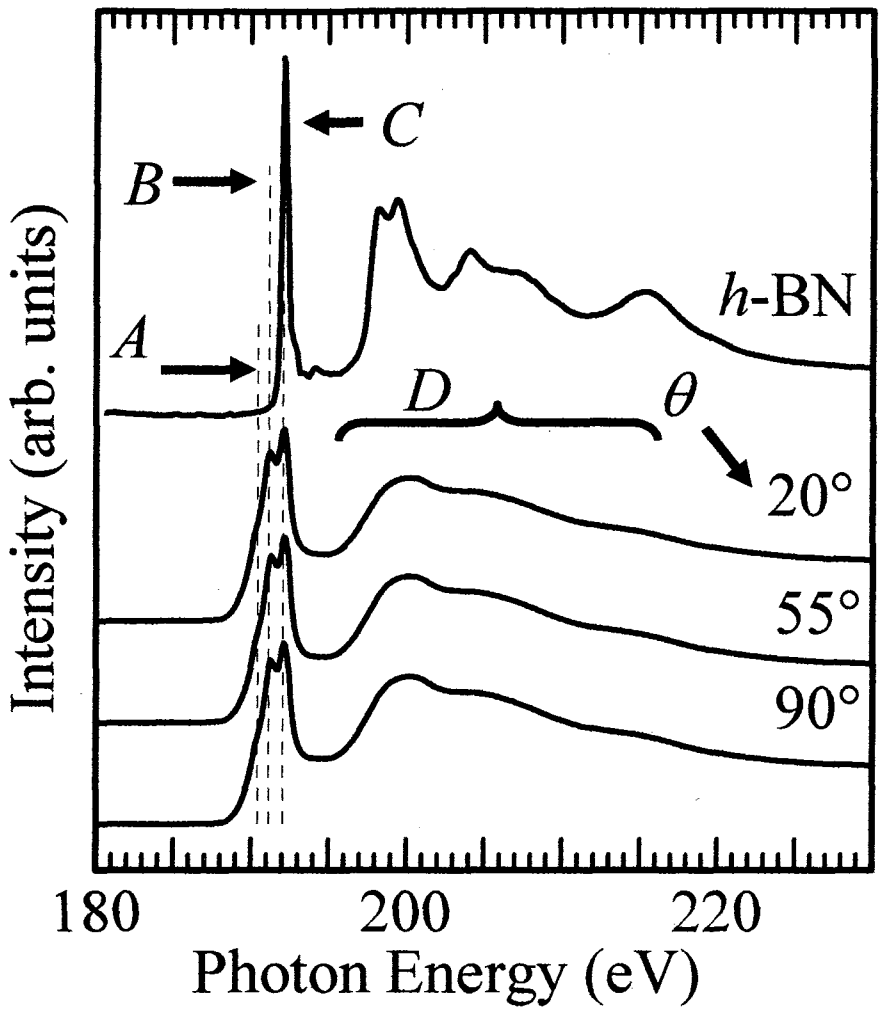

Fig. 41. B K-edge NEXAFS spectra for various incidence angles (θ) of x-ray of B-C-N hybrid films with the thickness of 2.3 nm synthesized at RT. NEXAFS spectrum for bulk *h*-BN is shown in the top of the figure.

These spectra show two clear peaks at the energy of 191.2 eV (*B*) and 192.1 eV (*C*). A small shoulder at the energy of ~190.3 eV (*A*) is also observed in these spectra. Figs. 39-41 show a broad feature (marked *D*) centered at the energy of 200.1 eV with long tail in the high energy region. For all films, the polarization dependence in peaks *A-D* is scarcely observed, suggesting that the B-C-N films synthesized at RT have random orientation.

3.4.3.2 Orientation of B-C-N hybrids prepared at 800 °C

B K-edge NEXAFS spectra for B-C-N hybrid films synthesized at 800 °C are shown in Figs. 42-44 for the film thicknesses of 0.4 nm, 2.1 nm, and 4.1 nm, respectively. For comparison, NEXAFS spectrum for bulk *h*-BN is shown in the top of each figure.

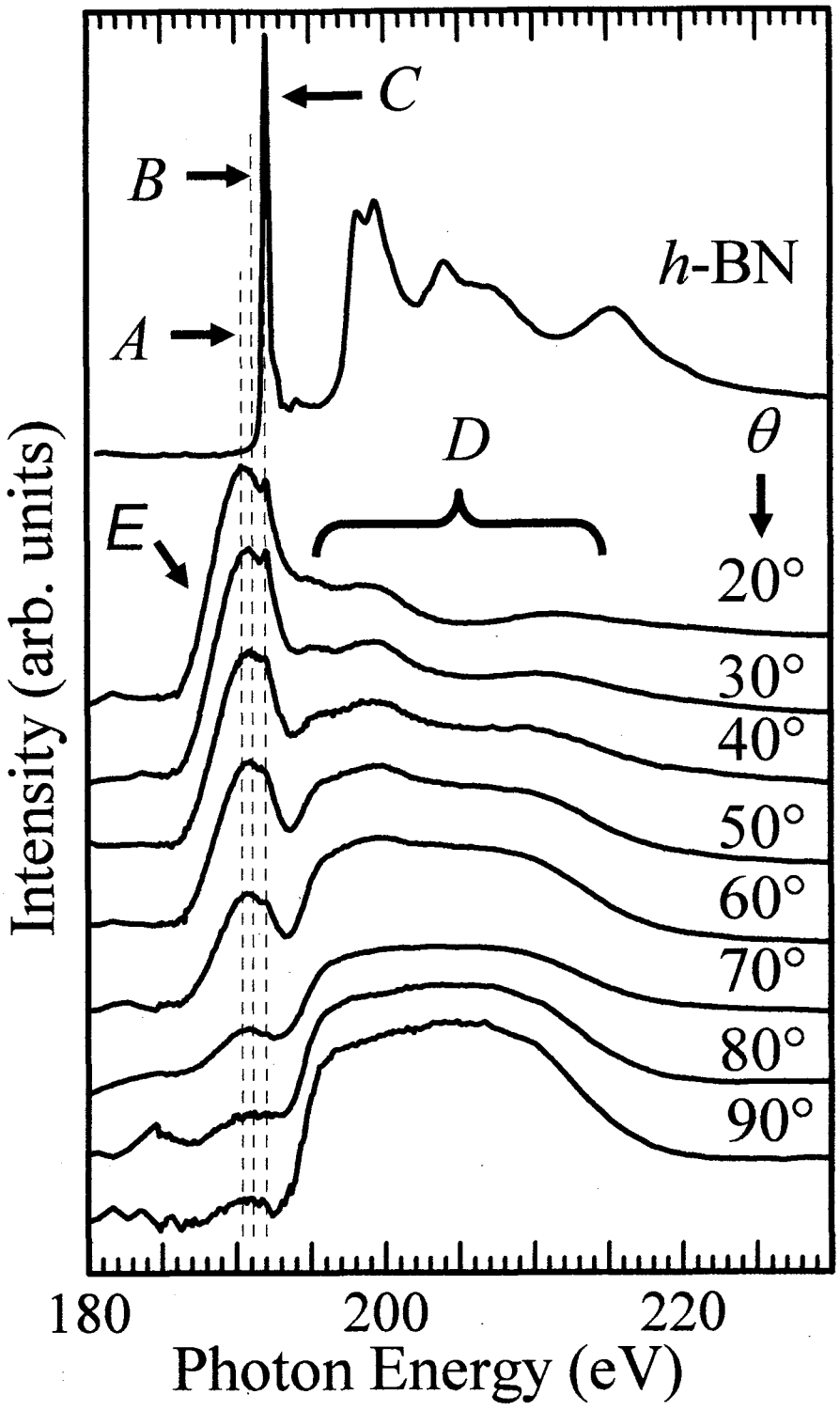

Fig. 42. B K-edge NEXAFS spectra for various incidence angles (θ) of x-ray of B-C-N hybrid films with the thickness of 0.4 nm synthesized at 800 °C. NEXAFS spectrum for bulk *h*-BN is shown in the top of the figure.

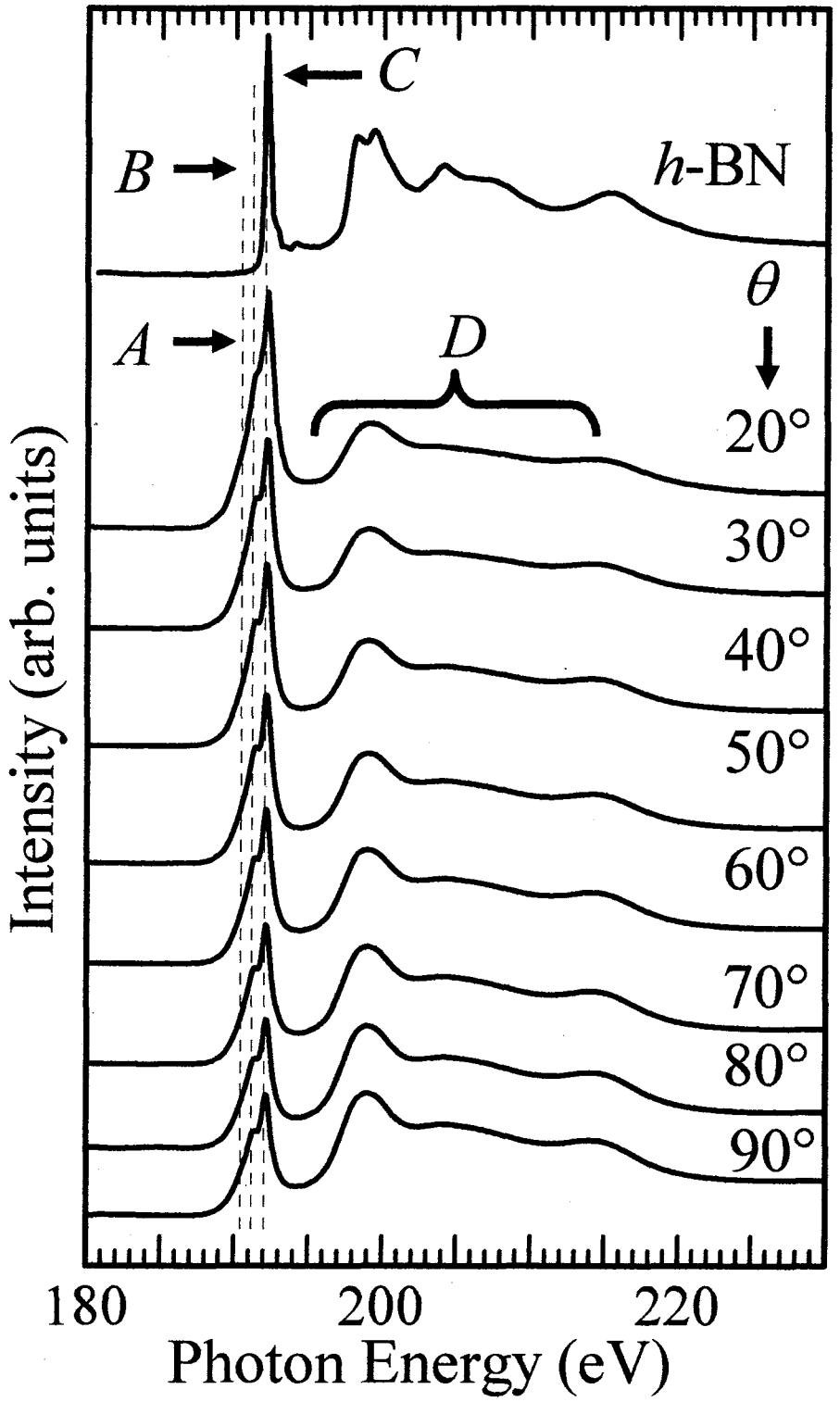

Fig. 43. B K-edge NEXAFS spectra for various incidence angles (θ) of x-ray of B-C-N hybrid films with the thickness of 2.1 nm synthesized at 800 °C. NEXAFS spectrum for bulk *h*-BN is shown in the top of the figure.

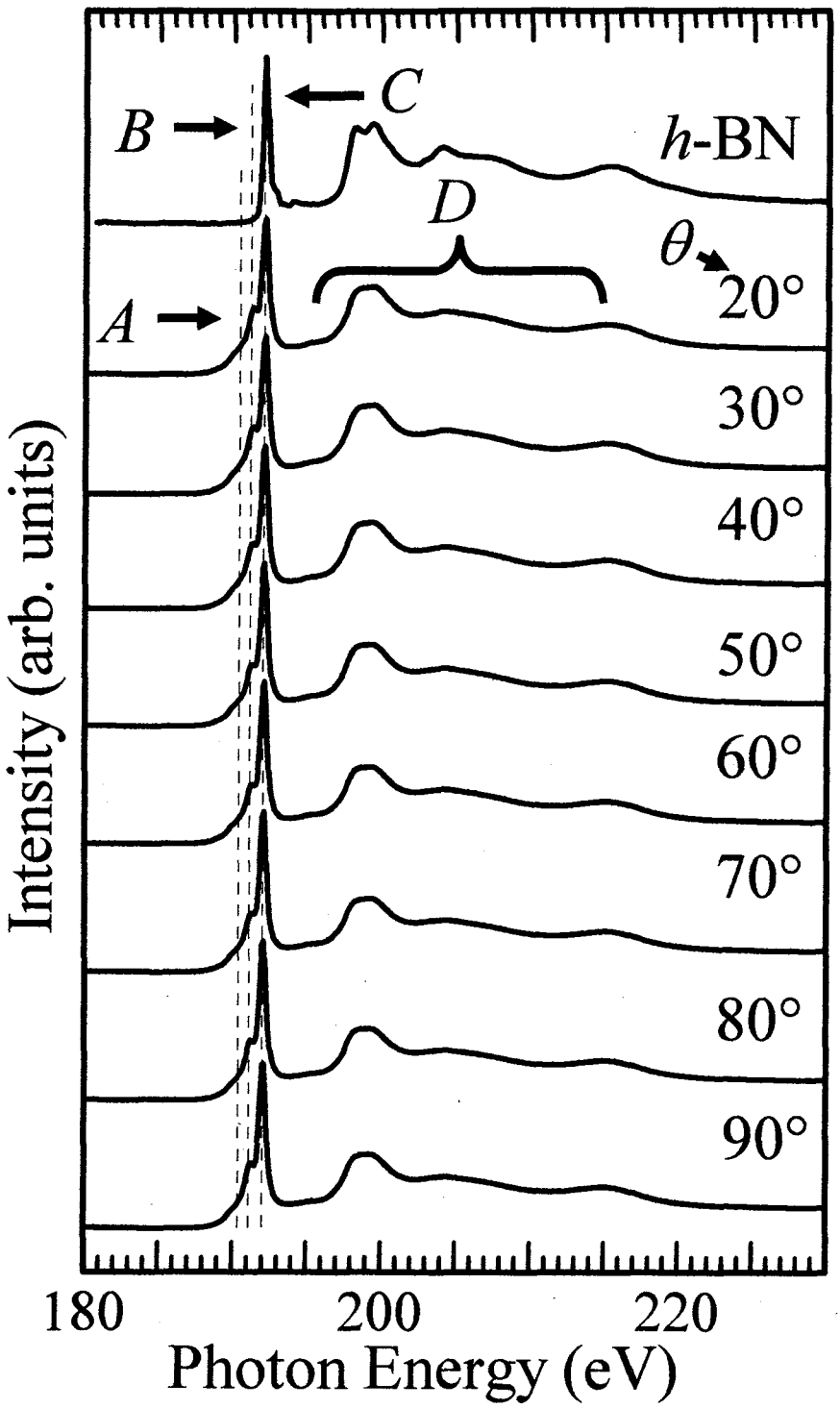

Fig. 44. B K-edge NEXAFS spectra for various incidence angles (θ) of x-ray of B-C-N hybrid films with the thickness of 4.1 nm synthesized at 800 °C. NEXAFS spectrum for bulk *h*-BN is shown in the top of the figure.

(i) Polarization dependence of the peaks at low fluence

The set of spectra in Fig. 42 show two broad features in the energy ranges of 187-193 eV (feature 1; marked *A*, *B*, *C*, and *E*) and 195-215 eV (feature 2; marked *D*). It is noteworthy that some new components (marked *E*) are present at the lower energies than that marked as *A*. There are two important observations in these spectra. One is the broad feature 1 which strongly indicates the formation of various local structures around boron atoms. The other is that the peak intensities in features 1 and 2 varied with the x-ray incidence angles. It is seen that the peaks at feature 1 almost vanish at normal incidence ($\theta = 90°$) and its intensities become high at the grazing incidence ($\theta = 20°$). In contrast, the intensities of the peaks at feature 2 become high at the normal incidence and they decrease drastically at the grazing incidence. This behavior of the peaks can be explained by the concept of polarization dependency of C K-edge NEXAFS spectra of HOPG [85]. The details of polarization dependence of the NEXAFS have been discussed in the experimental section 2.2.3.4.4.

In the present system, the peaks at features 1 and 2 (Fig. 42) show similar polarization dependencies for C(1s)→π^* and C(1s)→σ^* transitions of graphite, respectively (Fig. 17). Therefore, the peaks at features 1 and 2 must be originated from the B(1s)→π^* and B(1s)→σ^* transitions, respectively. Theoretical calculations suggest that the energy separation between B(1s)→π^* and B(1s)→σ^* resonances is 8.5 eV for graphite-like stoichiometric BC_2N [20]. It is in good agreement with the observed energy separation (>8 eV) between the peaks at features 1 and 2 shown in Fig. 42.

(ii) Structural orientation at high fluence and peak assignment

The peak *C* is attributed to π^* resonance at B sites which have BN_3 coordination, based on the fact that the energy position for the peak *C* coincides well with that of *h*-BN [23]. On the other hand, it is apparently supposed that peaks *B*, *A*, and *E* are responsible for the B sites in which the boron atoms bond with not only nitrogen atoms but also carbon atoms. Polarization dependencies of peaks *B*, *A*, and *E* have the same trend as that of π^* resonance in *h*-BN. This finding suggests that the transitions for the peaks *B*, *A*, and *E* have π^* character and that ordered structures of graphite-like planes consisting of B-C-N hybrids exist in the films. As to the atomic arrangement at the B sites, BCN_2 and BC_2N coordinations are immediately imagined between *h*-BN (BN_3 coordination) and graphite-like BC_3 [79]. XPS studies show that the B(1s) binding energy of BC_3 coordination is 2.6 eV lower than that of BN_3 coordination in the B-C-N hybrid film due to the electronegativity differences between B, C, and N [67,86]. In the case of carbon nitride (CN_x) films, Ripalda et al. [87] reported that the chemical shift of N K-edge π^* resonances in NEXAFS is attributed to the chemical shifts of N(1s) core levels which is obtained from XPS spectra. According to their report [67,87], it can be concluded that the peaks *B*, *A*,

and *E* belong to graphite-like structure of BC_nN_{3-n}, where n ranges from 1 to 3. It can also be said that components marked as E are attributed to B-C bonds formation because these components disappeared as the film thickness increased. These results suggest that various kinds of graphite-like B-C-N hybrids were formed in this film.

In Figs. 43 and 44, π*-like peaks (marked *A*, *B* and *C*) and σ*-like peaks (marked *D*) are also observed. As the borazine fluence increase, the intensities of the peaks *A* and *B* decrease whereas that of peak *C*, assigned for the π* resonance in *h*-BN increase. The spectrum shape at high fluence (Fig. 44) becomes very similar to that of *h*-BN, indicating the formation of the stoichiometric *h*-BN at high fluence. It also supports the XPS interpretation. The spectra in Fig. 44 do not show any polarization dependency. These results imply that the synthesized *h*-BN films are amorphous or randomly oriented.

(iii) Other structures

The π* peaks in the B K-edge NEXAFS spectra are associated with the formation of graphite-like structures which have B-C and B-N bonds as described above. However, one may point out other possibilities, the formation of dangling bonds and B-H bonds because we adopted ion beam for the synthesis and the ion beam included hydrogen as shown in Fig. 18. It is difficult to discuss these posibilities for the moment because the samples synthesized in this work contained variety of structures with B-C and B-N bonds. We think these should be discussed more with molecular orbital caluculation for future study. Neverthless, we roughly discuss these possibilities in turn below.

Jiménez et al. [88] reported formation of damaged structure of *h*-BN by irradiating Ar^+ and N_2^+ ions to *h*-BN. According to their report, B K-edge NEXAFS spectra of the damaged *h*-BN show three additional π^* peaks which are not observed in the spectra of *h*-BN. They assigned these π^* peaks to nitrogen void structure in which dangling bonds are formed at B site. These peaks are located above the original π^* peak which is assigned to B 1s $\rightarrow\pi^*$ transition of *h*-BN itself. On the other hand, no observable peak has been found above the peak *C* in the B K-edge NEXAFS spectra of our samples. If the assignment proposed by Jiménez is collect, the peaks E, B and A are not attributed to the formation of dangling bonds at B site. They also reported that phase transition from hexagonal to cubic is induced by the formation of the void structure. If cubic phase is formed, NEXAFS spectra would show only σ^* peak and show no polarization dependence. However, the σ^* resonance peak in Fig. 42 shows large polarization dependency. These all observations seem to nullify the formation of nitrogen void and cubic structures in the films.

The formation of B-H bonds is more difficult to verify than that of dangling bond formation. To our knowledge, no assignment has been reported for the B K-edge NEXAFS spectra of BN which includes hydrogen terminated B sites. Among the peaks A, B, and E, some of the π^* peaks may be

attributed to hydrogen terminated B site. However, it should be noted that intensity ratio of the peaks depends on the deposition amount. If all the additional π^* peaks originate from B-H bond, the peak intensity ratio would not significantly change depending on the deposition amount because borazine plasma always contain hydrogen. Therefore, the additional π^* peaks should be concerned with B-C bond formation. Another clue on this point is the graphite-like polarization dependence of the π^* peaks. This result means that the origin of the peaks have planer structure. If a B site is terminated with plural hydrogen atoms, planer structure can not be kept at the B site. We consider that the B sites which are attributed to the π^* peaks have B-C and/or B-N bonds to achieve planer structure.

3.4.4 Conclusions

XP spectra and the polarization dependencies of the B K-edge NEXAFS spectra have been observed for the films deposited on highly oriented pyrolytic graphite by borazine ion plasma implantation at 800 °C and RT. XP spectra indicated that the films are composed of BC_3, B-C-N hybrid, and BN_3 components. On the basis of the polarization dependence of the π^* resonance, it is concluded that amorphous or randomly oriented BN and B-C-N hybrids were deposited at 800 °C with high fluence of borazine and RT. In the films deposited at 800 °C with low fluence of borazine, NEXAFS spectra show a clear fingerprint for the existence of highly oriented graphite-like B-C-N hybrids.

4. Summary

Low-dimensional carbon materials such as graphite, fullerene, and nanotube have many potential applications to the electronic devices at nanometer scale. In order to search new low-dimensional material with semiconducting and insulating properties, one of the strategies is to synthesize heteroatom compounds of which configuration are analogous to graphite, fullerene and nanotube. The objective of this work is to synthesize new low-dimensional materials composed of carbon, nitrogen and boron where we can control electrical properties by changing the atomic composition. In this study, B-C-N hybrid thin films were grown from ion beam plasma of borazine on HOPG target at RT, 600 °C, 800 °C, and 850 °C. The films were characterized *in-situ* by XPS and NEXAFS. XPS study suggested that B, N and C atoms in the deposited films were in a wide variety of chemical bonds *e.g.*, B-C, B-N, N-C, and B-C-N. The substrate temperature and ion fluence had significant effects on the coordination and elemental binding on the B-C-N hybrids. It was found that B-C-N hybrids formation was enhanced at high temperature, and that the B-C-N component was dominantly synthesized at low

fluence of borazine. The results imply that it is possible to control the composition of B-C-N hybrids by changing the ion fluence and the temperature during ion implantation.

The resonance peaks from B(1s) to both π^*-like and σ^*-like orbitals were clearly observed in the B K-edge NEXAFS spectra. It suggested the existence of sp^2 configuration around the boron atoms. On the basis of the polarization dependencies observed in the B(1s)$\rightarrow\pi^*$ resonance peaks for B-C-N films deposited at 800 °C, it is confirmed that the highly oriented graphite-like B-C-N hybrids surely exist at low boron content. It is also found that amorphous or randomly oriented BN and B-C-N hybrids were deposited at 800 °C with high fluence of borazine and RT.

ACKNOWLEDGEMENTS

One of the authors (N.Md.U.) wishes to acknowledge JAERI for providing the opportunity to work at JAERI as a research student. We also thank Dr. Y. Kitajima of the Photon Factory, KEK for supporting XPS and NEXAFS measurements at the BL-11A. Thanks are also due to the stuff of the Photon Factory for supporting the experiments using synchrotron radiation.

REFERENCES

(1) M. Kawaguchi, Adv. Mater., 9, 615 (1997).

(2) W. J. Pan, J. Sun, H. Ling, N. Xu, Z. F. Ying, and J. D. Wu, Appl. Surf. Sci. 218, 297 (2003).

(3) R. Gago, I. Jiménez, J. M. Albella, and L. J. Terminello, Appl. Phys. Lett. 78, 3430 (2001).

(4) T. Nakahara, N. Fujimori, Mat. Res. Innovat. 1, 38 (1997).

(5) R. Riedel, Adv. Mater., 6, 549 (1994).

(6) T. Yoshida, Diam. Rel. Mater., 5, 501 (1996).

(7) P. B. Mirkarimi, K. F. McCarty, D. L. Medlin, Mater. Sci. Eng., R 21, 1 (1997).

(8) J. Robertson, Phil. Mag. B., 75, 335 (1997).

(9) J. C. Agnus, C. C. Hayman, Science, 241, 913 (1988).

(10) A. Grill., Diamond Relat. Mater., 8, 428 (1999).

(11) J. Robertson, Phil. Trans. R. Soc. Lind. A., 342, 277 (1993).

(12) A. Grill, Wear., 168, 143 (1993).

(13) J. Robertson, Prog. Solid State Chem., 21, 199 (1991).

(14) S. J. Bull, Diamond Relat. Mater., 4, 827 (1995).

(15) A. Grill, Surf. Coat. Technol., 94/95, 507 (1997).

(16) A. Y. Liu, R. M. Wentzcovitch, and M. L. Cohen, Phys. Rev. B, 39, 1760 (1989).

(17) M. Kawaguchi, T. Kawashima, and T. Nakajima, Chem. Mater., 8, 1197 (1996).

(18) M. Kawaguchi and Y. Wakukawa, Carbon, 37, 147 (1999).

(19) J. Kouvetakis, T. Sasaki, C. Shen, R. Hagiwara, M. Lerner, K. M. Krishnan, and N. Bartlett, Synth. Met., 34, 1 (1989).

(20) M. Wibbelt, H. Kohl, and Ph. Kohler-Redlich, Phys. Rev. B **59**, 11739 (1999).

(21) R. Gago, I. Jiménez, F. Agulló-Rueda, J. M. Albella, Zs. Czigány, and L. Hultman, J. Appl. Phys., 92, 5177 (2002).

(22) J. Stöhr, NEXAFS Spectroscopy, Springer Series in Surface Science, Vol. 25, Springer, New Yourk (1992).

(23) I. Shimoyama, Y. Baba, T. Sekiguchi, and K. G. Nath, submitted to Phys. Rev. B.

(24) I. Shimoyama, G. Wu, T. Sekiguchi, and Y. Baba, Phys. Rev. B, 62, R6053 (2000).

(25) A. Perrone, A.P. Caricato, A. Luches, M. Dinescu, , C. Ghica, V. Sandu, and A. Andrei, Appl. Surf. Sci, 133, 239 (1998).

(26) M. Dinescu, A. Perrone, A.P. Caricato, L. Mirenghi, C. Gerardi, C. Ghica, and L. Frunza, Appl. Surf. Sci, 127-129, 692 (1998).

(27) Y. K. Yap, Y. Wada, M. Yamaoka, M. Yoshimura, Y. Mri, and T. Sasaki, Diamond Rel. Mater., 10, 1137 (2001).

(28) R. Gago, I. Jiménez, I. García, and J. M. Albella, Vacuum, 64, 199 (2002).

(29) R. Gago, I. Jiménez, J. M. Albella, Thin Solid Films, 373, 277 (2000).

(30) M. V. Ugarov, V. P. Ageev, A. V. Karabutov, E. N. Loubnin, S. M. Pimenov, V. I. Konov, and A. Bensaoula, Appl. Surf. Sci., 138-139, 359 (1999).

(31) T. Sasaki, M. Akaishi, S. Yamaoka, Y. Fujiki, and T. Okawa, Chem. Mater., 5, 695 (1993).

(32) M.O. Watanabe, S. Itoh, K. Mizushima, and T. Sasaki, J. Appl. Phys., 78, 2880 (1995).

(33) R. A. W. Pryor, Appl. Phys. Lett., 68, 1802 (1996).

(34) F. L. Huang, C. B. Cao, X. Xiang, R. T. Lv, and H. S. Zhu, Diamond Relt. Mater., 13, 1757 (2004).

(35) E. R. Engbrecht, Y. –M. Sun, K. H. Junker, J. M. White and J. G. Ekerdt, J. Vac. Sci. Technol. A, 22, 2152 (2004).

(36) A. Tempez, N. Badi, A. Bensaoula, and J. Kulik, J. Vac. Sci. Technol. A, 16, 2896 (1998).

(37) R. Gago, I. Jiménez, T. Sajavaara, E. Rauhala, and J. M. Albella, Diam. Rel. Mater., 10, 1165 (2001).

(38) Z-M Ren, Y-C Du, Z-F Ying, F-M Li, J. Lin, Y-Z Ren, and X-F Zong, Mater. Chem. Phys., 50, 98 (1997).

(39) V. Linssa,b, N. Schwarzera, T. Chudobab, M. Karniychuka, F. Richtera, Surf. Coat. Techn., 195, 287 (2005).

(40) T. Thamm, K.-U. Ko¨rner, W. Bohne, E. Strub, J. Rohrich, S. Stockel, G. Marx, Appl. Surf. Sc., 252, 223 (2005).

(41) Yan-li Li, Nuo-fu Chen, Jian-ping Zhou, Shu-lin Song, Shao-yan Yang and Zhi-kai Liu, J. Cryst. Growth, 262, 186 (2004).

(42) O. Kutsay, I. Bello, Y. Lifshitz, C. W. Lam, W. Y. Luk, S. T. Lee, X. Meng and V. Kremnican, Diamond Relt. Mater., 12, 2051 (2003).

(43) M. M. Mitan, D. P. Pivin, T. L. Alford and J. W. Mayer, Thin Solid Films, 411, 219 (2002).

(44) Tetsuya Shibata, Yun-Sik Jin, Yoshinobu Matsuda and Hiroshi Fujiyama, Surf. Coat. Techn., 131, 428 (2000).

(45) S. -T. Lee, W. M. Lau, L. J. Huang, Z. Ren and F. Qin, Diam. Rel. Mater., 4, 1353 (1995).

(46) D. Ivanenko and J. Pomeranchuk, Phys. Rev., 65, 343 (1944).

(47) J. Schwinger, Phys. Rev., 70, 798 (1946).

(48) E.E. Koch, B. Kunz and B. Sonntag, Phys. Rep., 29, 153 (1977).

(49) H. Winick and S. Doniach, Synchrotron Radiation Research Eds. Plenum Press, New York, p. ll (1979).

(50) P. Carra and M. Altarelli, Phys. Rev. Lett., 64, 1286 (1990).

(51) F. M. F. de Groot, J. Electron Scectrosc. Rel. Phen., 67, 529 (1994).

(52) J. Somers, A.W. Robinson, Th. Linder, D. Ricken and A.M. Bradshaw, Phys. Rev. B, 40, 2053 (1989).

(53) A.M. Bradshaw and J. Somers, Phys. Scr., T31, 189 (1990).

(54) Ch. Ziegler, Th. Schedel-Niedrig, G. Beamson, D.T. Clark, W.R. Salaneck, H. Sotabayashi and A.M. Bradshaw, Langmuir, 10, 4439 (1994).

(55) U. Fano and J.W. Cooper, Rev. Mod. Phys., 40, 441 (1968).

(56) G. Ertl and J. Kiippers, Low Energy Electrons and Surface Chemistry, Monographs in Modern Chemistry, Verlag Chemie Weinheim, 4, 7 (1974).

(57) I. Lindau and W.E. Spicer, J. Electron Spectrosc. Rel. Phen., 3, 409 (1974).

(58) C.J. Powell, Surf. Sci., 44, 29 (1974).

(59) J.G. Timothy and R.P. Madden, in: Handbook on Synchrotron Radiation, edited by E.E. Koch, North-Holland, Amsterdam 315 (1983).

(60) F. W. Mclafferty and D. B. Stauffer, The Willy/NBS Registry of Mass Spectral Data, Willey Interscience, New York, 1, 15 (1989).

(61) J.J. Yeh, I. Lindau, Atomic Data Nucl. Tables 32, 1 (1985).

(62) H. Yamamoto, Y. Baba, J. Kor. Vac. Soc., 9, 84 (2000).

(63) S. Tanuma, C.J. Powell, D.R. Penn, Surf. Interface Anal., 21, 165 (1994).

(64) I. Shimoyama, Y. Baba, T. Sekiguchi, and K. G. Nath, J. Vac. Sci. Technol. A, 21, 1843 (2003).

(65) Z. F. Zhou, I. Bello, M. K. Lei, K. Y. Li, C. S. Lee, and S. T. Lee, Surf. Coat. Technol., 128-129, 334 (2000).

(66) Y. Etou, T. Tai, T. Sugiyama, and T. Sugino, Diam. Rel. Mater., 11, 985 (2002).

(67) M. Nizam Uddin, I. Shimoyama, Y. Baba, T. Sekiguchi, K. G. Nath, and M. Nagano, Appl. Surf. Sci., 241, 246 (2005).

(68) T. Hasegawa, K. Yamamoto, and Y. Kakudate, Diamond Relt. Mater., 11, 1290 (2002).

(69) H. Ling, J. D. Wu, J. Sun, W. Shi, Z. F. Ying, and F. M. Li, Diamond Relt. Mater., 11, 1623 (2002).

(70) M. O. Watanabe, S. Itoh, K. Mizushima, and T. Sasaki, Appl. Phys. Lett. 68 (21), 2962 (1996).

(71) F. Saugnac, F. Tessandier, and A. Marchand, J. Am. Ceram. Soc., 75 (1), 161 (1992).

(73) I. Shimoyama, G. Wu, T. Sekiguchi, and Y. Baba, J. Elec. Spec. Relat. Phenom., 114-116, 841 (2001).

(74) H. Kunzl, P. Gantenbein, R. Steiner, and P. Oelhafen, Fres. J. Anal. Chem., 346, 41 (1993).

(75) D. N. Hendrickson, J. M. Hollander, and W. L. Jolly, Inorg. Chem., 9, 612 (1970).

(76) D. H. Kim, E. Byon, S. Lee, J. –K Kim, and H. Ruh, Thin Solid Films, 447-448, 192 (2004).

(77) S. Ulrich, A. Kratzsch, H. Leiste, M. Stüber, P. Schloßmacher, H. Holleck, J. Binder, D. Schild, S. Westermeyer, P. Becker, and H. Oechsner, Surf. Coat. Technol., 116-119, 742 (1999).

(78) K. Siegbahn, C. Nordling, A. Fahlman, R. Nordberg, K. Hamrin, J. Hedman, G. Johansson, T. Bergmark, S. E. Karlsson, I. Lindgren , and B. Lindberg, Nova Acta Regiae Soc. Sci., Ups., 4, 20 (1967).

(79) J. Kouvetakis, R.B. Kaner, M.L. Sattler, and N. Bartlett, J. Chem. Soc. Chem. Commun., 1758 (1986).

(80) D. Tománek, S. G. Laue, and M. L. Cohen, Phys. Rev. B, 37, 3134 (1988).

(81) V. Linss, S. E. Rodil, P. Reinke, M. G. Garnier, P. Oelhafen, U. Kreissig, and F. Richter, Thin Solid Films, 467, 76 (2004).

(82) T. Klotzbucher, W. Pfleging, D. A. Wesner, M. Mergens, and E. W. Krentz, Diamond Rel. Mater., 5, 525 (1996).

(83) I. Shimoyama, Y. Baba, T. Sekiguchi, and K. G. Nath, J. Elec. Spec. Relat. Phenom., 137-140, 573 (2004).

(84) M. Nizam Uddin, I. Shimoyama, Y. Baba, T. Sekiguchi, and M. Nagano, J. Vac. Sci. Technol. A, 23 (3), 497 (2005).

(85) R.A. Rosenberg, P.J. Love and V. Rehn, Phys. Rev. B, 33, 4034 (1986).

(86) A. Perrone, A. P. Caricato, A. Luches, M. Dinescu, C. Ghica, V. Sandu, and A. Andrei, Appl. Surf. Sci., 133, 239 (1998).

(87) J. M. Ripalda, E. Román, N, Díaz, L. Galán, I. Montero, G. Comelli, A. Baraldi, S. Lizzit, A. Goldoni, and G. Paolucci, Phys. Rev. B, 60, R3705 (1999).

(88) I. Jiménez, A. Jankowski, L. J. Terminello, J. A. Carslisle, D. G. J. Sutherland, G. L. Doll, J. V. Mantese, W. M. Tong, D. K. Shuh, and F. J. Himpsel, Appl. Phys. Lett., 68, 2816 (1996).

国際単位系（SI）

表１．SI 基本単位

基本量	SI 基本単位	
	名称	記号
長さ	メートル	m
質量	キログラム	kg
時間	秒	s
電流	アンペア	A
熱力学温度	ケルビン	K
物質量	モル	mol
光度	カンデラ	cd

表２．基本単位を用いて表されるSI組立単位の例

組立量	SI 基本単位	
	名称	記号
面積	平方メートル	m^2
体積	立法メートル	m^3
速さ，速度	メートル毎秒	m/s
加速度	メートル毎秒毎秒	m/s^2
波数	毎メートル	m^{-1}
密度（質量密度）	キログラム毎立法メートル	kg/m^3
質量体積（比体積）	立法メートル毎キログラム	m^3/kg
電流密度	アンペア毎平方メートル	A/m^2
磁界の強さ	アンペア毎メートル	A/m
（物質量の）濃度	モル毎立方メートル	mol/m^3
輝度	カンデラ毎平方メートル	cd/m^2
屈折率	（数の）1	1

表５．SI 接頭語

乗数	接頭語	記号	乗数	接頭語	記号
10^{24}	ヨタ	Y	10^{-1}	デシ	d
10^{21}	ゼタ	Z	10^{-2}	センチ	c
10^{18}	エクサ	E	10^{-3}	ミリ	m
10^{15}	ペタ	P	10^{-6}	マイクロ	μ
10^{12}	テラ	T	10^{-9}	ナノ	n
10^{9}	ギガ	G	10^{-12}	ピコ	p
10^{6}	メガ	M	10^{-15}	フェムト	f
10^{3}	キロ	k	10^{-18}	アト	a
10^{2}	ヘクト	h	10^{-21}	ゼプト	z
10^{1}	デカ	da	10^{-24}	ヨクト	y

表３．固有の名称とその独自の記号で表されるSI組立単位

組立量	SI 組立単位			
	名称	記号	他のSI単位による表し方	SI基本単位による表し方
平面角	ラジアン(a)	rad		$m \cdot m^{-1}=1$(b)
立体角	ステラジアン(a)	sr(c)		$m^2 \cdot m^{-2}=1$(b)
周波数	ヘルツ	Hz		s^{-1}
力	ニュートン	N		$m \cdot kg \cdot s^{-2}$
圧力，応力	パスカル	Pa	N/m^2	$m^{-1} \cdot kg \cdot s^{-2}$
エネルギー，仕事，熱量	ジュール	J	N・m	$m^2 \cdot kg \cdot s^{-2}$
工率，放射束	ワット	W	J/s	$m^2 \cdot kg \cdot s^{-3}$
電荷，電気量	クーロン	C		s・A
電位差（電圧），起電力	ボルト	V	W/A	$m^2 \cdot kg \cdot s^{-3} \cdot A^{-1}$
静電容量	ファラド	F	C/V	$m^{-2} \cdot kg^{-1} \cdot s^4 \cdot A^2$
電気抵抗	オーム	Ω	V/A	$m^2 \cdot kg \cdot s^{-3} \cdot A^{-2}$
コンダクタンス	ジーメンス	S	A/V	$m^{-2} \cdot kg^{-1} \cdot s^3 \cdot A^2$
磁束	ウエーバ	Wb	V・s	$m^2 \cdot kg \cdot s^{-2} \cdot A^{-1}$
磁束密度	テスラ	T	Wb/m^2	$kg \cdot s^{-2} \cdot A^{-1}$
インダクタンス	ヘンリー	H	Wb/A	$m^2 \cdot kg \cdot s^{-2} \cdot A^{-2}$
セルシウス温度	セルシウス度(d)	℃		K
光束	ルーメン	lm	cd・sr(c)	$m^2 \cdot m^{-2} \cdot cd=cd$
照度	ルクス	lx	lm/m^2	$m^2 \cdot m^{-4} \cdot cd=m^{-2} \cdot cd$
（放射性核種の）放射能	ベクレル	Bq		s^{-1}
吸収線量，質量エネルギー分与，カーマ	グレイ	Gy	J/kg	$m^2 \cdot s^{-2}$
線量当量，周辺線量当量，方向性線量当量，個人線量当量，組織線量当	シーベルト	Sv	J/kg	$m^2 \cdot s^{-2}$

(a) ラジアン及びステラジアンの使用は、同じ次元であっても異なった性質をもった量を区別するときの組立単位の表し方として利点がある。組立単位を形作るときのいくつかの用例は表４に示されている。
(b) 実際には、使用する時には記号rad及びsrが用いられるが、習慣として組立単位としての記号“１”は明示されない。
(c) 測光学では、ステラジアンの名称と記号srを単位の表し方の中にそのまま維持している。
(d) この単位は、例としてミリセルシウス度m℃のようにSI接頭語を伴って用いても良い。

表４．単位の中に固有の名称とその独自の記号を含むSI組立単位の例

組立量	SI 組立単位		
	名称	記号	SI 基本単位による表し方
粘度	パスカル秒	Pa・s	$m^{-1} \cdot kg \cdot s^{-1}$
力のモーメント	ニュートンメートル	N・m	$m^2 \cdot kg \cdot s^{-2}$
表面張力	ニュートン毎メートル	N/m	$kg \cdot s^{-2}$
角速度	ラジアン毎秒	rad/s	$m \cdot m^{-1} \cdot s^{-1}=s^{-1}$
角加速度	ラジアン毎平方秒	rad/s^2	$m \cdot m^{-1} \cdot s^{-2}=s^{-2}$
熱流密度，放射照度	ワット毎平方メートル	W/m^2	$kg \cdot s^{-3}$
熱容量，エントロピー	ジュール毎ケルビン	J/K	$m^2 \cdot kg \cdot s^{-2} \cdot K^{-1}$
質量熱容量（比熱容量），質量エントロピー	ジュール毎キログラム毎ケルビン	J/(kg・K)	$m^2 \cdot s^{-2} \cdot K^{-1}$
質量エネルギー（比エネルギー）	ジュール毎キログラム	J/kg	$m^2 \cdot s^{-2} \cdot K^{-1}$
熱伝導率	ワット毎メートル毎ケルビン	W/(m・K)	$m \cdot kg \cdot s^{-3} \cdot K^{-1}$
体積エネルギー	ジュール毎立方メートル	J/m^3	$m^{-1} \cdot kg \cdot s^{-2}$
電界の強さ	ボルト毎メートル	V/m	$m \cdot kg \cdot s^{-3} \cdot A^{-1}$
体積電荷	クーロン毎立方メートル	C/m^3	$m^{-3} \cdot s \cdot A$
電気変位	クーロン毎平方メートル	C/m^2	$m^{-2} \cdot s \cdot A$
誘電率	ファラド毎メートル	F/m	$m^{-3} \cdot kg^{-1} \cdot s^4 \cdot A^2$
透磁率	ヘンリー毎メートル	H/m	$m \cdot kg \cdot s^{-2} \cdot A^{-2}$
モルエネルギー	ジュール毎モル	J/mol	$m^2 \cdot kg \cdot s^{-2} \cdot mol^{-1}$
モルエントロピー，モル熱容量	ジュール毎モル毎ケルビン	J/(mol・K)	$m^2 \cdot kg \cdot s^{-2} \cdot K^{-1} \cdot mol^{-1}$
照射線量（Ｘ線及びγ線）	クーロン毎キログラム	C/kg	$kg^{-1} \cdot s \cdot A$
吸収線量率	グレイ毎秒	Gy/s	$m^2 \cdot s^{-3}$
放射強度	ワット毎ステラジアン	W/sr	$m^4 \cdot m^{-2} \cdot kg \cdot s^{-3}=m^2 \cdot kg \cdot s^{-3}$
放射輝度	ワット毎平方メートル毎ステラジアン	$W/(m^2 \cdot sr)$	$m^2 \cdot m^{-2} \cdot kg \cdot s^{-3}=kg \cdot s^{-3}$

表６．国際単位系と併用されるが国際単位系に属さない単位

名称	記号	SI 単位による値
分	min	1 min=60s
時	h	1h =60 min=3600 s
日	d	1 d=24 h=86400 s
度	°	1° =(π/180) rad
分	’	1’ =(1/60)° =(π/10800) rad
秒	”	1” =(1/60)’ =(π/648000) rad
リットル	l、L	1l=1 $dm^3=10^{-3}m^3$
トン	t	$1t=10^3$ kg
ネーパ	Np	1Np=1
ベル	B	1B=(1/2)ln10(Np)

表７．国際単位系と併用されこれに属さない単位でSI単位で表される数値が実験的に得られるもの

名称	記号	SI 単位であらわされる数値
電子ボルト	eV	$1eV=1.60217733(49) \times 10^{-19}J$
統一原子質量単位	u	$1u=1.6605402(10) \times 10^{-27}kg$
天文単位	ua	$1ua=1.49597870691(30) \times 10^{11}m$

表８．国際単位系に属さないが国際単位系と併用されるその他の単位

名称	記号	SI 単位であらわされる数値
海里		1海里=1852m
ノット		1ノット=1海里毎時=(1852/3600)m/s
アール	a	$1 á=1 dam^2=10^2m^2$
ヘクタール	ha	$1 ha=1 hm^2=10^4m^2$
バール	bar	$1 bar=0.1MPa=100kPa=1000hPa=10^5Pa$
オングストローム	Å	$1 Å=0.1nm=10^{-10}m$
バーン	b	$1 b=100fm^2=10^{-28}m^2$

表９．固有の名称を含むCGS組立単位

名称	記号	SI 単位であらわされる数値
エルグ	erg	$1 erg=10^{-7}$ J
ダイン	dyn	$1 dyn=10^{-5}$N
ポアズ	P	$1 P=1 dyn \cdot s/cm^2=0.1Pa \cdot s$
ストークス	St	$1 St=1cm^2/s=10^{-4}m^2/s$
ガウス	G	$1 G \hat{} 10^{-4}T$
エルステッド	Oe	$1 Oe \hat{} (1000/4\pi)A/m$
マクスウェル	Mx	$1 Mx \hat{} 10^{-8}Wb$
スチルブ	sb	$1 sb=1cd/cm^2=10^4cd/m^2$
ホト	ph	$1 ph=10^4lx$
ガル	Gal	$1 Gal=1cm/s^2=10^{-2}m/s^2$

表10．国際単位に属さないその他の単位の例

名称	記号	SI 単位であらわされる数値
キュリー	Ci	$1 Ci=3.7 \times 10^{10}Bq$
レントゲン	R	$1 R = 2.58 \times 10^{-4}C/kg$
ラド	rad	$1 rad=1cGy=10^{-2}Gy$
レム	rem	$1 rem=1 cSv=10^{-2}Sv$
X線単位		$1X unit=1.002 \times 10^{-4}nm$
ガンマ	γ	$1\gamma=1 nT=10^{-9}T$
ジャンスキー	Jy	$1 Jy=10^{-26}W \cdot m^{-2} \cdot Hz^{-1}$
フェルミ		$1 fermi=1 fm=10^{-15}m$
メートル系カラット		1 metric carat = 200 mg = 2×10^{-4}kg
トル	Torr	1 Torr = (101 325/760) Pa
標準大気圧	atm	1 atm = 101 325 Pa
カロリー	cal	
ミクロン	μ	$1 \mu=1\mu m=10^{-6}m$

（第７版，1998年改訂）